

A PULSED ULTRASONIC FLOWMETER
EMPLOYING TIME DOMAIN METHODS

BY

STEVEN GERALD FOSTER

B.S., Illinois Institute of Technology, 1978
M.S., University of Illinois, 1981

THESIS

Submitted in partial fulfillment of the requirements
for the degree of Doctor of Philosophy in Electrical
Engineering in the Graduate College of the
University of Illinois at Urbana-Champaign, 1985.

Urbana, Illinois

A PULSED ULTRASONIC FLOWMETER
EMPLOYING TIME DOMAIN METHODS

Steven Gerald Foster, Ph.D.
Department of Electrical Engineering
University of Illinois at Urbana-Champaign, 1985

In this thesis the flow velocity profile across a vessel is determined. Knowledge of the velocity profile is valuable in determining the condition of the vessel and the heart. The time domain method (TDM) being described is an ultrasonic approach for determining flow velocity profiles. Currently available ultrasonic methods transmit more energy into the body than the TDM for the same degree of accuracy and they cannot correct for vessel motion.

The TDM measures the velocity profile by transmitting two short ultrasonic pulses separated by a known amount of time. Two echoes from the two pulses scattered from the medium are amplified, digitalized, and then stored in a high speed memory in which the digitalized data can be read by the computer used for digital signal processing. The TDM then cuts out a portion of the first echo at a desired range and overlays and moves it across the second echo. The point at which the cut-out portion of the first echo is maximally correlated with the second echo is the change in range which the scatterers of the second echo have moved with respect to the first echo in the intervening time between the transmission of the two pulses. From the change in range information and the time interval between the two pulses, the radial velocity of the scatterers can be determined.

In this work, the TDM is first studied by computer simulation. In the simulation a variety of parameters are used: vessel diameter, beam width of the transducer, the amount of damping of the transducer, and the type of velocity profile. Next, the TDM is applied to determine the velocity profile of buttermilk (substitute for blood) pumped through tubing. The application of the TDM on the buttermilk is in agreement with the simulation. Included is a discussion of the sources of errors resulting from each system parameter.

The motion of the tubing can be eliminated by first lining up the second echo with the first at the tube wall where there is a large echo, then applying the TDM. With two ultrasonic pulses, the TDM achieves a precision of 3% in estimating midstream flow. Other available ultrasonic means must use many more pulses (hundreds) to achieve the same precision.

TABLE OF CONTENTS

	Page
I. INTRODUCTION.....	1
II. THEORY OF THE TIME DOMAIN METHOD.....	9
A. Signal Model of the Echo from a Scattering Medium.....	9
B. Determination of the Change in Range of a Scatterer.....	13
C. Errors Associated with the Field Pattern of the Transducer.....	21
D. Limitations of the Correlation Method.....	26
1. Error Associated with Windowing.....	27
2. Jitter Associated with a Velocity Gradient within the Range Cell.....	32
3. Jitter Associated with Nonzero Time Duration of the System Impulse Response and Velocity Gradients.....	38
4. Jitter Associated with Nonzero Beam Width and Velocity Gradients.....	40
5. Jitter Associated with Intensity Modulation Across the Beam.....	41
E. Determination of the Viewing Angle.....	44

III.	COMPUTER SIMULATION OF THE TIME DOMAIN METHOD FOR DETERMINING FLOW PROFILES.....	52
IV.	EXPERIMENTAL VERIFICATION.....	70
A.	Experimental Setup.....	70
B.	Description of A/D Unit.....	80
C.	Measured Statistics of the Echo Waveform.....	84
D.	Velocity Profile Results.....	89
E.	Estimated Speed Linear Dependence on Actual Speed.....	93
F.	Estimated Speed Dependence on Viewing Angle.....	96
G.	Absolute Agreement Between Estimated Speed and Actual Speed.....	101
H.	Estimated Speed Dependence on the Amount of Shift Between Successive Echoes.....	105
I.	Variance of the Estimate of the Midstream Flow.....	107
J.	Correlation Coefficient Measurements.....	109
V.	ERRORS INTRODUCED BY QUANTIZATION OF THE ECHOES.....	116
VI.	DISCUSSION.....	128
A.	Comparison Between Computer Simulation of the Theory and Experimental Results.....	128
B.	Comparison of Pulsed Techniques with the Time Domain Method.....	134

C.	Further Predictions of the Simulation in Chapter III.....	137
D.	Scaling.....	141
VII.	IMPROVEMENTS FOR THE TIME DOMAIN METHOD.....	143
	APPENDIX.....	145
	LIST OF REFERENCES.....	159
	VITA.....	163

I. INTRODUCTION

Of the two ultrasonic methods currently employed for obtaining blood flow information, continuous wave (CW) Doppler and pulsed Doppler, only the latter is capable of providing range information. This study explores a new signal processing technique for obtaining blood flow velocity and range information with ultrasound. The technique is called the time domain method (TDM).

The first pulsed Doppler devices were developed in the mid-sixties [1]. A system developed by Baker transmitted periodic (coherent) ultrasonic pulses consisting of five cycles at the resonant frequency of the transducer (5 megahertz (MHz)) at a pulse repetition rate between 12.5 kilohertz (kHz) and 25 kHz [2]. To understand the signal processing employed, it is helpful to examine the general expressions describing the waveform $f(t)$ and the Fourier series $F(t)$ of such pulsed Doppler systems,

$$f(t) = \begin{cases} \sin \frac{2\pi}{T_0} t & -\frac{N}{2}T_0 + nT \leq t \leq \frac{N}{2}T_0 + nT \\ 0 & \text{elsewhere} \end{cases} \quad \text{Eq. (I.1)}$$

$$F(t) = \sum_{k=1}^{\infty} b_k \sin \frac{2\pi k}{T} t \quad \text{Eq. (I.2)}$$

$$b_k = \frac{NT_0}{T} \left[\text{sinc} [NT_0(f_0 - k f_r)] - \text{sinc} [NT_0(f_0 + k f_r)] \right] \quad \text{Eq. (I.3)}$$

where T (f_T) is the pulse repetition period (frequency), f_o (T_o) is the resonant frequency (period) of the transducer, N is the number of cycles in the pulse burst, and n is an integer. For large N and $f_o > 0$ then;

$$b_k \doteq \frac{NT_o}{T} \text{sinc}[NT_o(f_o - kf_T)] \quad \text{Eq. (I.4)}$$

The receiver used a gate to select the echo from a desired range, mixed the gated portion of the echo with the 5 MHz sinusoid, and low pass filtered the output. The Doppler shift was determined from the average frequency of this low passed output. It should be noted that only the energy of a single spectral line was used in the mixer; the energy of the other spectral lines was lost. From Eq. (I.4) it can be seen that the energy in the spectral line is equal to the product of duty cycle ($N \cdot T_o / T$) and the total power in the waveform. For Baker's system [2] the duty cycle was 1/80 to 1/40 resulting in the use of 19 to 16 decibels (dB) less energy than the total available energy. A system (such as the TDM) that uses all the energy in the gated portion of the echo will have a corresponding increase in signal-to-noise ratio. Other researchers have stayed with Baker's pulse-coherent system which Baker introduced with little modification of the underlying system principle [3,4].

The duty cycle of pulsed Doppler systems can be increased by transmitting a long pulse of a random (or pseudorandom) waveform without the accompanying reduction of range resolution that transmitting a longer pulse of a pure

sinusoid would provide. Bendick [5] was the first to use a random waveform for determining the Doppler shift from blood flow by ultrasonic means. Bendick transmitted a random Gaussian waveform, received the resulting echo, mixed the echo with a delayed version of the transmitted waveform, and low pass filtered the output of the mixer. The output of the low pass filter contained the Doppler shift. Jethwa [6] also used a random Gaussian waveform, but he was able to operate at a lower average pulse repetition rate without introducing velocity ambiguities by using random pulse staggering. By operating at lower average pulse repetition rates, the amount of clutter (uncorrelated echoes from ranges other than the range of interest) was reduced and the signal-to-noise ratio was improved.

Cathigol [7] transmitted a non-Gaussian pseudorandom waveform instead of a random Gaussian waveform. The waveform was generated by a logic circuit and the delayed waveform needed for the mixer was simply the waveform being passed through a shift register. The use of random Gaussian waveforms requires an analog delay line.

Still another potential problem of presently available Doppler blood flow measurement systems is that the Doppler angle (the angle between the vessel and the transducer axis) is needed to quantify blood flow measurements. Three methods of determining the Doppler angle have been developed. In the null method, the transducer is moved in an arc with respect to the vessel to determine the angle for a minimum Doppler shift (or null), the 90 degree Doppler angle [1]. Other

Doppler angles can be found by reference to this angle. The major difficulty with this method is determining the plane in which to rotate the transducer since the plane containing the vessel is not known. Another point is that the null is broad, making the exact null angle difficult to ascertain. These difficulties make the null method the most inaccurate of the three methods discussed herein.

In a second method (the image method) the Doppler angle may be determined by imaging the vessel to find the orientation with respect to the transducer [1]. The image method has a very costly image processor.

The third method is the triangulation method. It uses three transducers whose axes are orthogonal and whose focal points are situated at the same point in space [8]. The method eliminates the subjectivity inherent in the null method. However, the cost of increased circuitry, the addition of two precisely aligned transducers, and problems of clinical implementation are disadvantages.

Varner et al. [9] showed that in the case of a single scatterer, the Doppler angle is related to the inverse tangent of the ratio of the bandwidth of the reflected signal to its center frequency. The experimental usefulness of this method has yet to be demonstrated.

Even with the limitations described above, the Doppler shift has been employed clinically as a measure of the blood flow speed. This may largely be due to the instrumentation development, in that all Doppler devices are FM receivers which can be constructed with relative ease. However, even

in the most ideal case of randomly distributed scatterers with uniform velocity, the Doppler shift will be a random process with a mean which is directly related to the speed of the scatterers. The Doppler receiver must estimate this mean. If a nonrandom parameter related to the speed of the scatterers could be used, then the measurements might be subject to less variation. One such parameter is the change in range of a target between ultrasonic pulses. That is, if the second echo must be moved 0.1 millimeter (mm) in range to match the first echo, and the time between transmission of the two pulses is 1 millisecond (ms), then the scatterers are moving at a speed $0.1 \text{ mm} / (2 * 0.001 \text{ s}) = 50 \text{ mm/second (s)}$ axially with respect to the transducer. Until the advent of high speed analog to digital converters (A/D) there was no simple way to implement this approach.

The time domain method presented in this thesis for determining blood speed exploits the idea of measuring the change in range between the same scatterers in two successive echoes and using the interpulse time interval. The TDM and pulsed Doppler methods are each capable of providing: (1) the velocity profile across the vessel, (2) the Doppler angle (hereafter called the viewing angle when discussing the TDM), (3) the direction of flow, and (4) the subtraction of stationary targets. Blood flow measurements at several ranges across the vessel are needed to determine the velocity profile. If the flow rates are to be obtained simultaneously, this requires duplication of the hardware for each range in pulsed Doppler systems. The TDM has the

advantage of requiring no additional hardware. The velocity estimates using the TDM are dependent on the angle between the axis of the transducer and the axis of the vessel. The pulsed Doppler technique must use one of the aforementioned methods for finding the Doppler angle, whereas the TDM can potentially measure the angle through the statistics of the echoes (using only one transducer). The TDM determines the direction of flow of the scattering medium without any increase in hardware; however, pulse Doppler techniques require a more sophisticated demodulation method, such as quadrature detection, to determine direction. To eliminate stationary echoes (such as multiple reflections from the vessel wall) from the desired echo information, the pulsed Doppler techniques use analog delay lines [10]. The TDM finds the stationary echoes by averaging the echoes long enough to remove the fast moving random returns, then digitally subtracts the stationary echoes from each echo to be processed.

The TDM provides the desired clinical flow information more efficiently since it needs only two echoes to determine the speed of the scatterers, whereas pulsed Doppler techniques need many (hundreds). Also, the TDM utilizes all the energy in the echo, whereas pulsed Doppler techniques use typically less than a fiftieth of the available energy.

The major topic of this thesis is the theoretical development of the TDM for the measurement of blood flow. A model for the scattered signal from an ultrasonic pulse scattered from blood is necessary for understanding the

theoretical aspects of this work. Brody [11,12] used a model that assumed that erythrocytes were independent point scatterers, that their positions followed a Poisson distribution, and that their scattering coefficients were random with a mean of zero. Newhouse [13] used the same model for the study of the effect of the transit time of the erythrocyte passing through the sound beam on Doppler flow measurements.

Shung [14] found experimentally that as the hematocrit increased to 26% the scattering coefficient increased. However, as the hematocrit was increased further, the scattering coefficient decreased, violating the ideal of the erythrocyte as an independent scatterer in normal blood (hematocrit of 45%). In order to circumvent the mathematical difficulties of treating the erythrocyte as a nonindependent point scatterer, Angelsen [15] divided the transducer field pattern into one-tenth wavelength cubicals. The scattering coefficient of each cubical was shown to be approximately independent of the neighboring cubicals, to have a Gaussian distribution, and to have the spectrum of the transmitted ultrasonic pulse. The Angelsen [15] model is used in this thesis and the term scatterer will refer to Angelsen's cubicals hereafter and not to the constituent red blood cells that make up each cubical.

The organization of the remainder of the material is as follows: In Chapter II, the theoretical foundation of the time domain method is discussed; in Chapter III, the theory is verified by computer simulation. Chapter IV gives the

experimental results which are shown to agree with the theoretically predicted results of Chapter II. In Chapter V, the experimental sources of error due to the quantization of the echo by the high speed A/D converter are discussed. In Chapter VI, the experimental results and those predicted by theory are compared to the results of the frequency domain methods under similar conditions. Improvements in the experimental arrangement and considerations for future development are discussed in Chapter VII.

One goal of the study is to establish trends in the selection of experimental parameters (such as the degree of focus of a transducer) and not their optimization for a particular clinical environment. Often it is difficult to isolate one parameter from another; hence, making the optimization (or the criteria for a measure of optimization) is difficult.

II. THEORY OF THE TIME DOMAIN METHOD

A. Signal Model of the Echo from a Scattering Medium

Throughout this thesis the signal model that will be used for the echoes from the scattering medium is bandpass white Gaussian noise (BPWGN). Angelsen has derived this model rigorously [15], but it will be summarized here. In normal blood, the red blood cell (erythrocyte) is the major scatterer and constitutes approximately 45% of the blood volume [16]. The volume of a single erythrocyte is about 87 cubic micrometers [16]. At 5 MHz the wavelength of sound in blood is about 300 micrometers. Assuming that the size and shape of an acoustic particle may be a cube with the length of each side to be a tenth of a wavelength, then each particle contains 135 erythrocytes. A cube with sides of a tenth of a wavelength contains a sufficient number of erythrocytes such that a statistical approximation of a large number of samples is applicable, and the cube is small enough to allow the cube to behave as an acoustic particle.

In moving blood where the formation of rouleux is minimal, there is no preferred spatial position for the erythrocyte since all locations in the fluid have the same probability of being occupied by an erythrocyte [15]. Hence, a particle in the fluid will contain on the average 135 erythrocytes, but generally the number of the randomly distributed erythrocytes in the particle will be greater than (or less than) 135 with a corresponding greater density and a lesser compressibility (or lesser density and greater compressibility) than the average. From the Central Limit

Theorem, the density of the scattering particle can be approximated as a Gaussian random variable. Angelsen continues the derivation stating that since the number of erythrocytes in neighboring particles is independent and interaction between erythrocytes is not likely to extend more than a couple of blood cell diameters, the density and compressibility of the particle can be approximated as Gaussian independent variables [15]. Hence, the reflection coefficient of each particle can be modeled approximately as a Gaussian independent variable.

Each particle scatters back to the transducer an amplitude modulated replica (dependent on the relative compressibility and density difference of the particle) of the transmitted pulse. The intervening tissue will interact with the scattered ultrasound by attenuating the ultrasound and by presenting multiple return paths which will distort the ultrasound waveform. In this study the scattering fluid is contained in a tube submerged in a water bath where multipath phenomenon and attenuation played a minor role; hence, these effects are not considered in the signal model of the echo. The signal at the receiving transducer consists of the sum of all the individual echoes from each of the acoustic particles, delayed by the time that the ultrasound takes to travel from the source transducer to the particle and back to the receiving transducer. In this study the same transducer was used for transmission and reception. The mathematical representation of the amplified electrical signal received by the transducer is given by

$$w(t) = \int_V A(\bar{R}) h(\bar{R}, t - \frac{2|\bar{R}|}{c}) dR^3 \quad \text{Eq. (II.1)}$$

where $A(\bar{R})$ is the random reflection coefficient (zero mean and a variance of σ^2), $h(\bar{R}, t - \frac{2|\bar{R}|}{c})$ represents the echo from the particle dR^3 with a reflection coefficient of unity positioned at \bar{R} (see Figure 1), and c is the speed of the ultrasonic wave in the medium.

The function $h(\bar{R}, t - \frac{2|\bar{R}|}{c})$ is the system impulse response. The system impulse response is defined as the waveform that is available to the processor from an ultrasonic pulse (generated and detected by the system) reflecting from a single scatterer at position \bar{R} . Since the system is assumed to be linear, the band limiting of the system will be characterized by an ultrasonic pulse identical to the system impulse response, and the rest of the system (transducer, water path to scattering medium, and amplifier) can be assumed to be frequency independent.

The transmitted pulse rings for several cycles (the transducers used in this study had a Q of approximately 4, see Section IV.C.) and thus has a spectrum consisting of a band of frequencies centered about the resonant frequency of the transducer, i.e., a bandpass spectrum. Since the echo from the fluid consists of the sum of all the echoes from the scattering particles within the fluid, the echo from the fluid will also be characterized by a spectral band. The sum of these independent, bandpass Gaussian amplitude modulated echoes appears as a bandpass white Gaussian signal. The signal in this case resembles the noise on the output of a tuned amplifier resulting from thermal noise on its input.

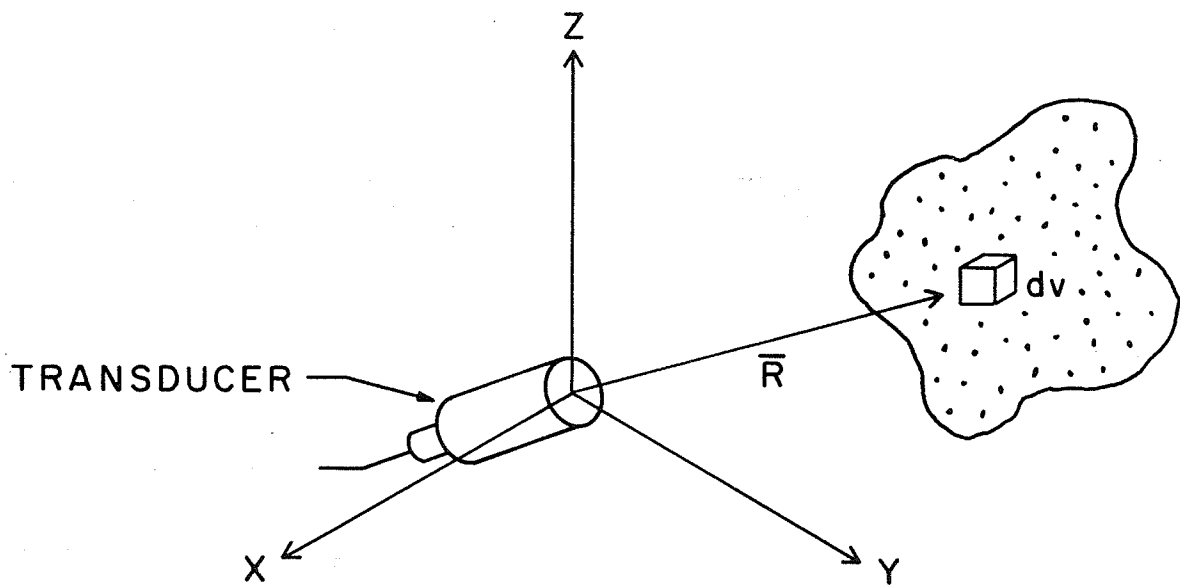


Figure 1. Transducer orientation with respect to the scatterers.

The BPWGN model is consistent with the experimental findings on the statistical parameters of the received signal (see Chapter IV).

One of the important characteristics of BPWGN is the sharpness, or Q , of the bandpass region where the Q is the center frequency divided by the 3 dB bandwidth. For example, if the Q is 0.5, BPWGN will appear as structureless. For high Q , the BPWGN signal will look like a sinusoid with a slowly varying amplitude. Figure 2 gives some examples of BPWGN for various Q 's. The spectrum of the waveforms in the figure is of a 6 pole Chebyshev bandpass filter with 1 dB of ripple in the pass band [17]. The filter was selected because it is causal, closely matches the response of the system used in this study, and is a well-known response. The Chebyshev response will be assumed throughout the thesis in the theoretical derivations and in the computer simulations.

B. Determination of the Change in Range of a Scatterer

This section will concern general principles of the correlation procedure which ensures determination of the amount that the scatterers move between the two transmitted pulses employed.

The model assumes that the scattering fluid is represented as a large number of independent scatterers. To assist in the understanding of the correlation procedure used in this study, consider the results of the procedure when applied to a single scatterer.

The change in range of an echo from a single scatterer is found by a correlation procedure which is pictorially

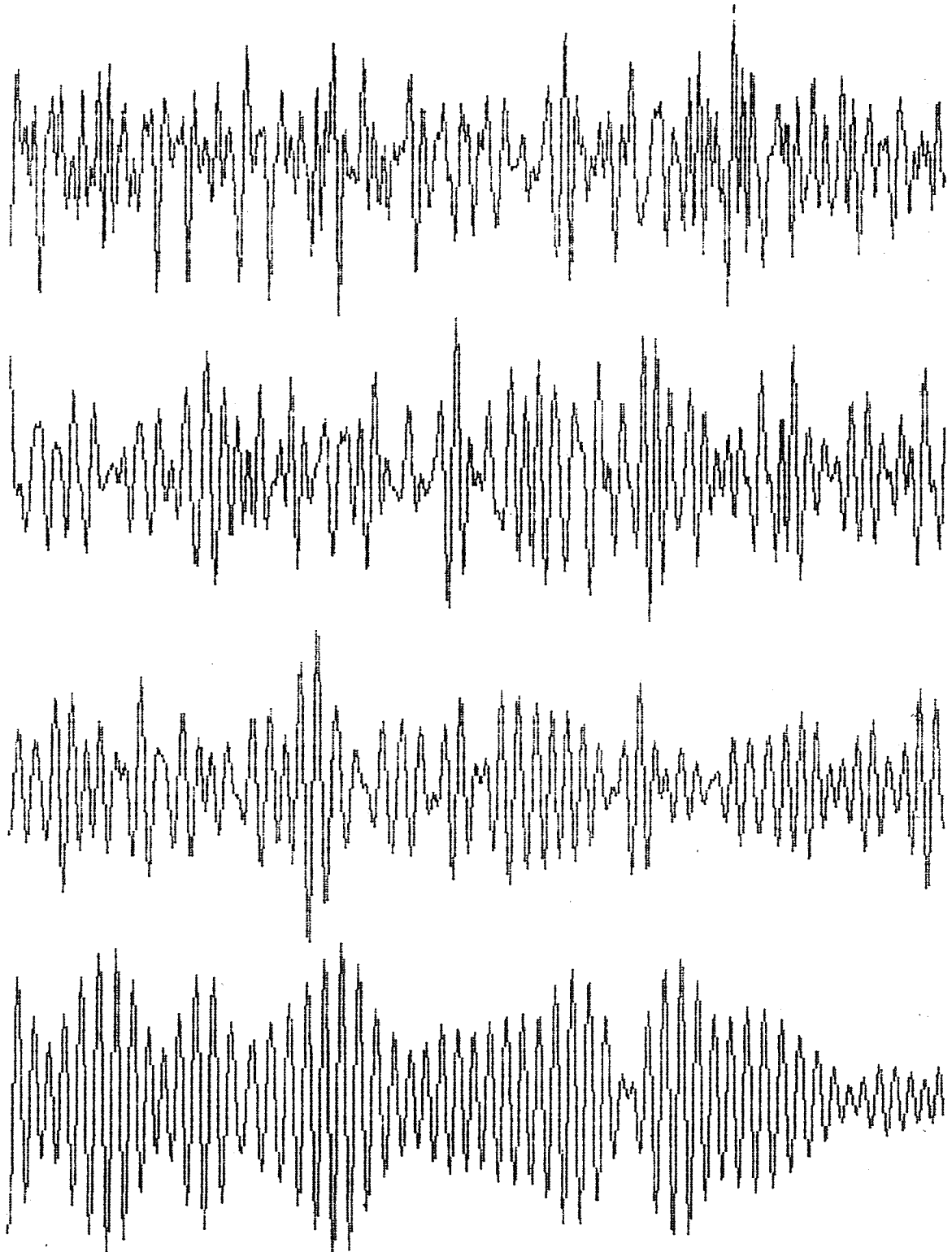


Figure 2. Examples of BPWGN. From top to bottom the Qs of the spectra of the waveforms are 0.5, 1.0, 2.0, and 4.0.

represented in Figure 3. It shows the range of the first echo, $w_1(t)$, as the reference point for range measurement. T seconds later, a second ultrasonic burst is transmitted and the second echo, $w_2(t)$, is received, but shifted down range by T_s from the first echo. The bottom waveform in Figure 3 is the correlation function of the two echoes defined by

$$R(\tau) = \int_{-\infty}^{\infty} w_1(t)w_2(t+\tau)dt \quad \text{Eq. (II.2)}$$

The two echoes are identical except for the second echo being delayed from the first:

$$w_2(t) = w_1(t-T_s) \quad \text{Eq. (II.3)}$$

$$\text{Hence, } R(\tau) = \int_{-\infty}^{\infty} w_1(t)w_1(t-T_s+\tau)dt = R_{11}(\tau-T_s) \quad \text{Eq. (II.4)}$$

where $R_{11}(\tau-T_s)$ is the autocorrelation function of $w_1(t)$ and thus maximal when the argument of the autocorrelation function is zero, i.e., when $\tau=T_s$. Hence, the amount of change in range of the second echo with respect to the first echo is found at the position where the correlation function of the two echoes is maximal (see Figure 3).

This procedure is equivalent to the well-known radar problem of determining the range of a target with known reflection characteristics [18,19]. The methods are approximately equivalent because the first echo yields the reflection characteristics of the scatterer whereas the

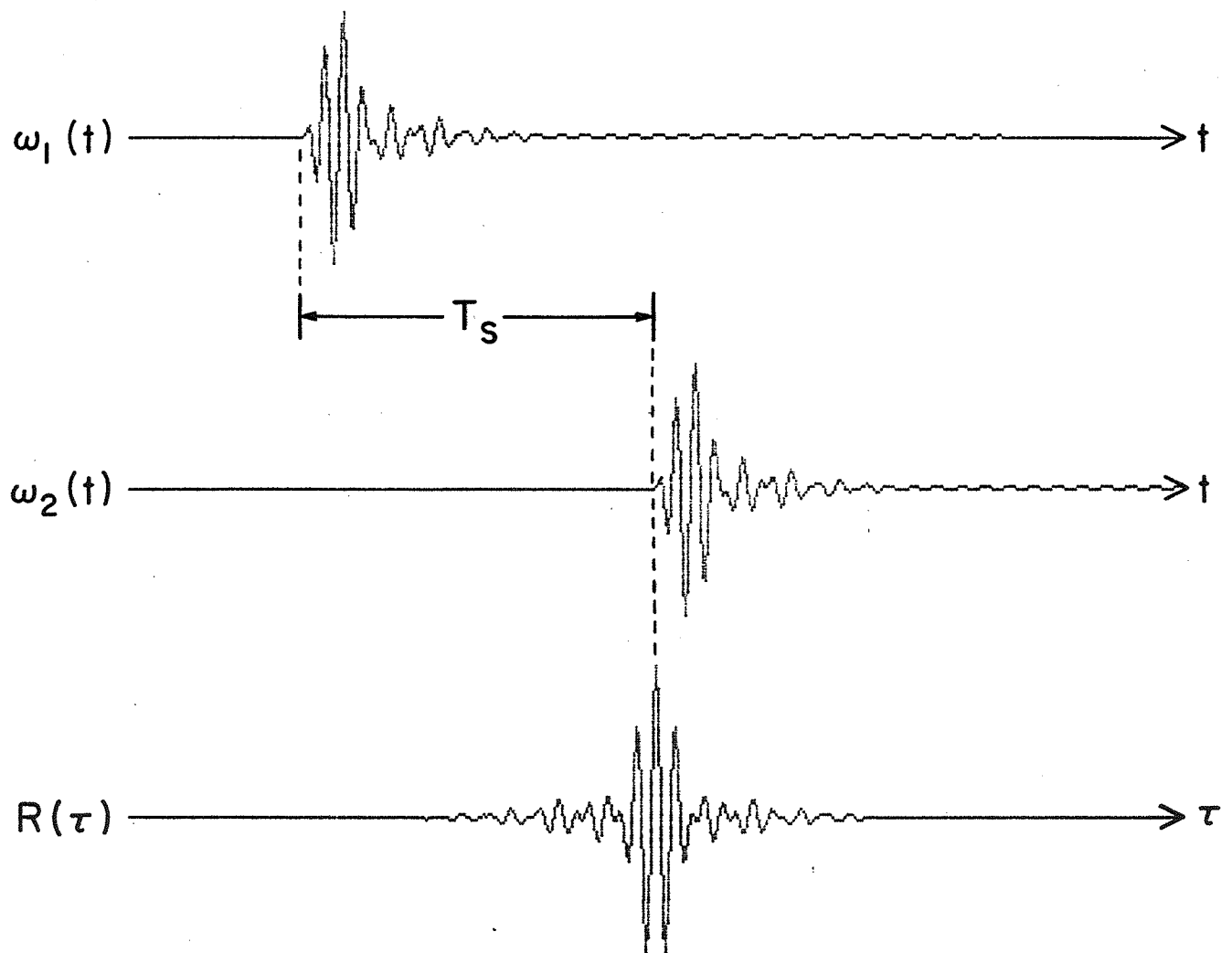


Figure 3. Correlation function (bottom curve) of the segment of the first echo (top curve) with the second echo (middle curve).

second echo is compared to determine the range at which it looks most like the first. The maximum likelihood estimate of the range of the second echo (assuming white additive noise) is the point where the two echoes are maximally correlated [18,19]. Thus the correlation procedure gives the maximum likelihood estimate of the change in range of the scatterer with white additive noise, assuming that the two echoes are identical except for a time delay.

Now the equation relating the speed of a single scatterer to the physical parameters of the transducer location will be derived. Figure 4 shows the geometry of the transducer and scatterer.

If the scatterer is moving with a velocity V , it moves from position 1 to position 2 in time T , as shown in Figure 4. Note that the component of the scatterer's velocity along the axis of the transducer is V_A . The axial distance that the scatterer has moved in time T is designated as ΔL where $\Delta L = VT \cos(\theta)$. At time $t=0$ an ultrasonic pulse is transmitted, and at time $t=T_1$ the echo from the scatterer at position 1 is received. At time $t=T$ a second pulse is transmitted. The scatterer has now moved to position 2 and the echo from the scatterer arrives at $t=T+T_2$. The propagation time for the echo from position 2 was T_2-T , longer than that for the echo returned from position 1, which is identical to the length of time the two echoes from this one scatterer are shifted. Therefore, $T_s = T_2 - T_1$, where T_s is positive when the scatterer is moving away from the transducer. (A negative value for T_s would mean the

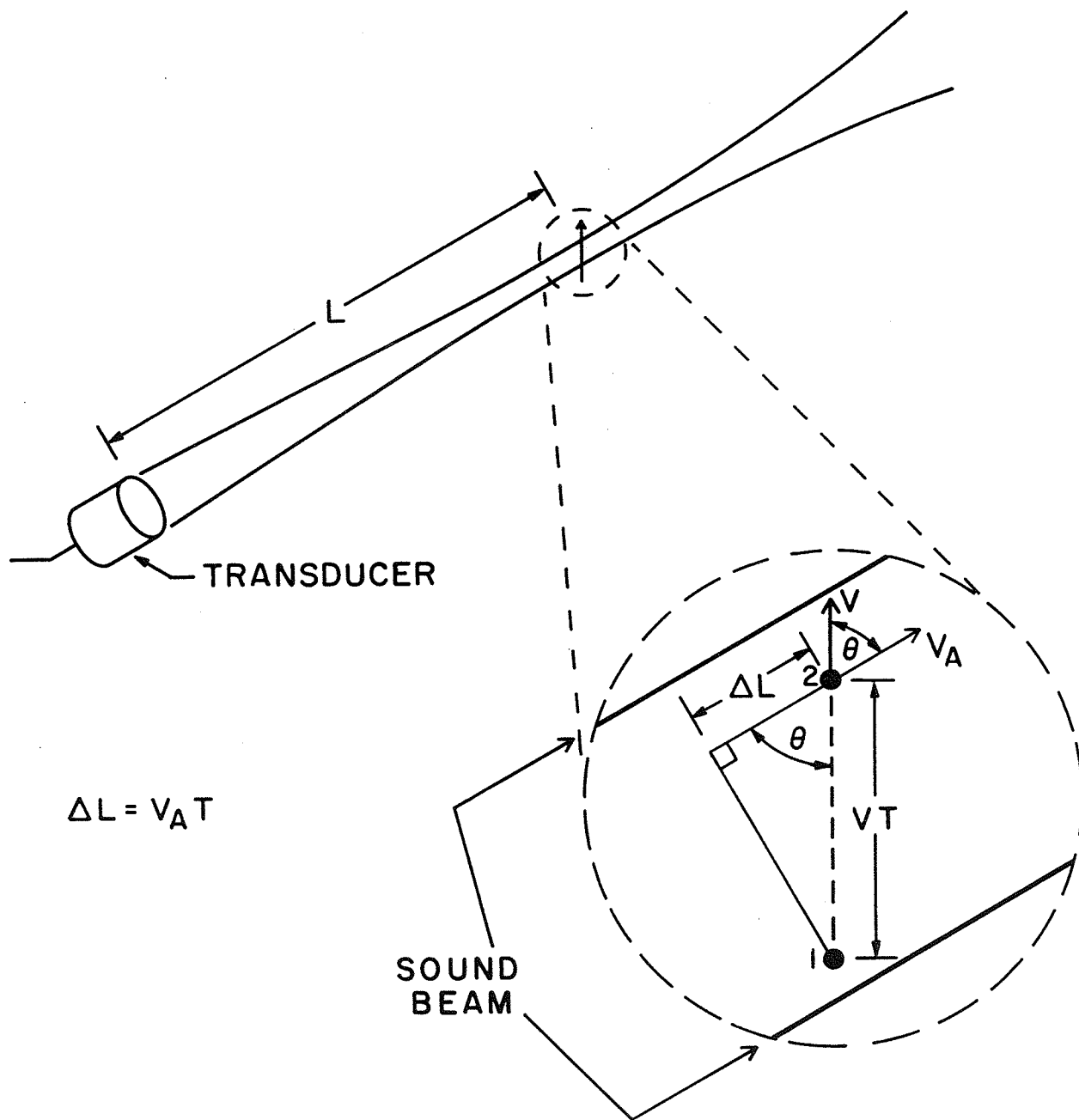


Figure 4. A schematic representation of the sound beam relative to the direction of flow of the scatterers. L is the range of point (1), θ is the viewing angle, and ΔL is the distance projected along the beam axis. The scatterers take T seconds to move from position 1 to position 2.

scatterer is moving towards the transducer.) The velocity component along the transducer axis is

$$V_A = \frac{cT_2/2 - cT_1/2}{T} \quad \text{Eq. (II.5)}$$

where c is the speed of sound in the scattering medium. Since the vessel is orientated at an angle ϕ (the viewing angle) the result must be scaled by $1/\cos(\phi)$, to yield the speed of the scatterer V :

$$V = \frac{c(T_2 - T_1)}{2T\cos(\phi)} = \frac{cT_s}{2T\cos(\phi)} \quad \text{Eq. (II.6)}$$

Figure 5 shows a representation of the correlation procedure for multiple scatterers. The bottom curve is the value of the correlation of the window of the first waveform with the second waveform. The value of the correlation function is read by extending the leading edge of a window down to the correlation function (the finely dotted line). Note that the second echo is delayed to the first echo by one cycle. This indicates that the scatterers are moving towards the transducer.

The correlation method for multiple scatterers is applied in the following manner (see Figure 5). Two sequential pulses are transmitted which are separated in time by a known amount. The two returned echoes are amplified, digitalized and stored (in the case of this study) for subsequent computer processing. To determine the shift between echoes at a particular range, a rectangular window is used to remove a segment from the first echo, $w(t)$, at the

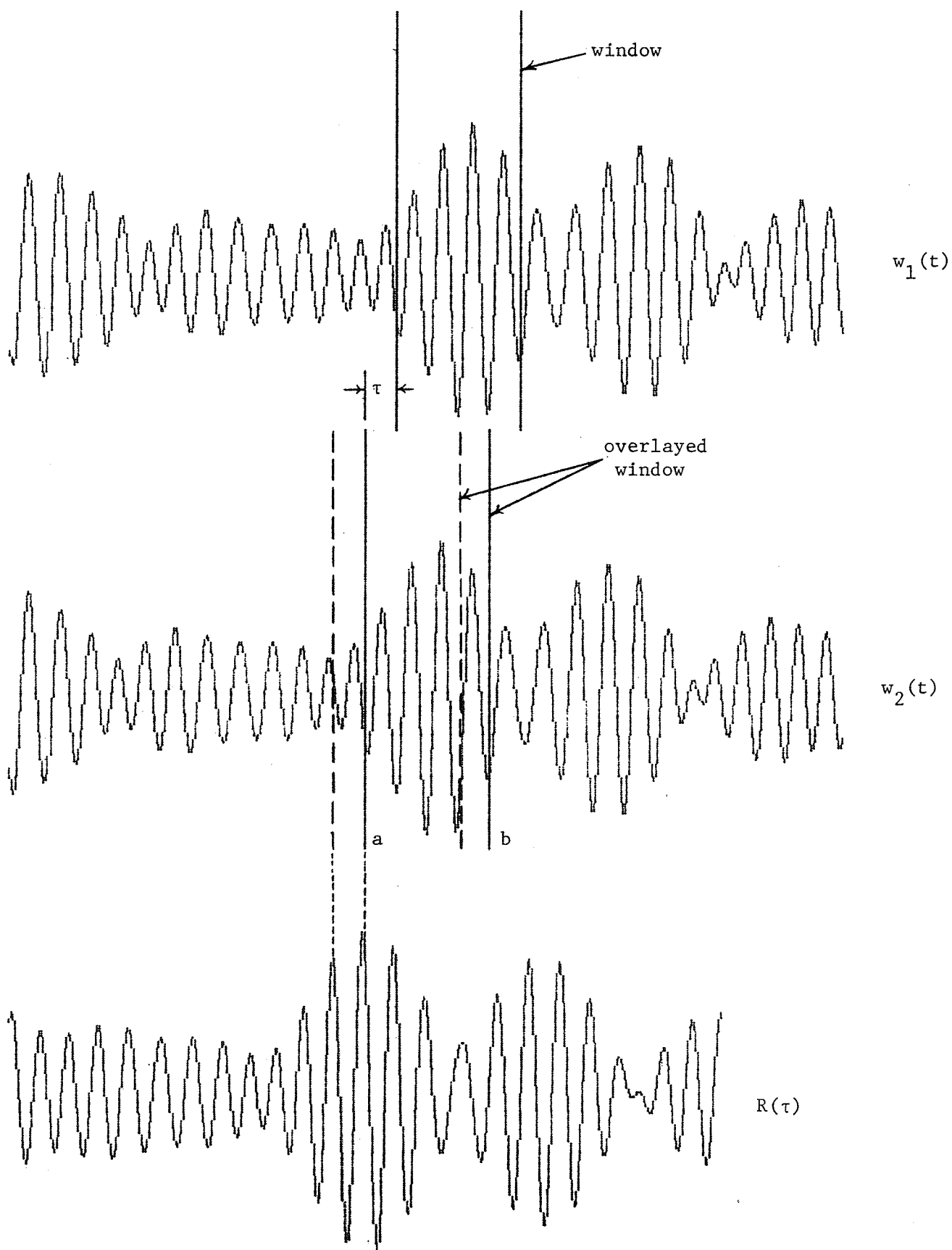


Figure 5. Segments of two successive bandpassed white Gaussian noise echoes.

particular range. This segment is overlaid and shifted along the second echo, $w_2(t)$, to determine the shift that results in maximum correlation. The amount that the windowed data are shifted in time to obtain this maximum correlation is directly related (except for the errors discussed in Sections C and D) to the axial velocity of the scatterers from the transducer. The shift $\hat{\tau}$ where maximum correlation occurs is determined by the following expression:

$$\hat{\tau} = \tau \int_a^b w_1(t) w_2(t+\tau) dt \quad \text{Eq. (II.7)}$$

C. Errors Associated with the Field Pattern of the Transducer

To a first-order approximation, the field pattern of a pulsed transducer will be taken as that for a CW transducer. The simulation of Chapter III also uses this approximation. The experimental results of Chapter IV will show the approximation to be valid. The justification for it is that the pulses from the transducers used in this study have Q 's of approximately 4 and, therefore, have a narrow spectrum (1.25 MHz bandwidth) centered at the natural resonant frequency (5 MHz) of the transducer. Hence, the pulsed field pattern will be similar to the field pattern of the transducer under sinusoidal excitation at its natural resonant frequency.

The assumption that the echoes are identical is not necessarily true since the intensity field pattern of the spherically focused transducer is not uniform. Instead, it has an Airy distribution perpendicular to the axis of the

transducer and a sinc function distribution along the axis for sinusoidal excitation [20]. For pulsed excitation the distributions are even less uniform. Born [20] has shown that the equal phase front (co-phasal) surfaces in the focus are substantially planar. However, the phase jumps 180 degrees at the node in the Airy distribution (surface of zero intensity). Figure 6 is the field pattern for a spherically focused transducer with focal length to aperture diameter ratio of 2; the aperture diameter is 84.7 wavelengths (model taken from Born [20]). The transducer is located at the left of the figure. This size of transducer is similar to the most strongly focused transducer used in our study. The vertical curves are co-phasal curves (resulting from a plane containing the transducer axis slicing through the co-phasal surfaces) which are rotationally symmetric about the axis of the transducer. The co-phasal curves are separated in the figure by 360 degrees and the horizontal and vertical directions have the same scale.

Born has also shown that the distance between co-phasal fronts in the focal region is longer than a wavelength (the wavelength of an infinite plane wave) by the factor

$$1 + \left(\frac{a}{2f}\right)^2 \quad \text{Eq. (II.8)}$$

where a is the radius of the transducer and f is the focal length. Hence, all ultrasonic measurements of the velocity of the scatterers in the focal region will be low by the factor in Eq. (II.8). For the transducer field which is shown in Figure 6, this factor is 1.016; therefore, the measurement of the speed of the scatterers will be low by

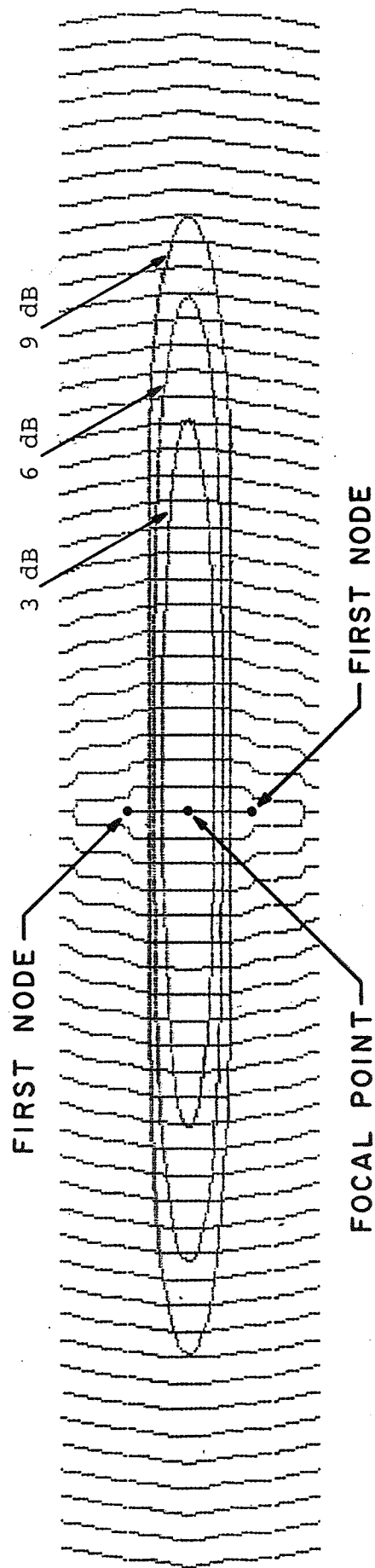


Figure 6. The field pattern for a spherically focused transducer with a focal length to aperture diameter of 2. The length of the aperture diameter is 84.7 wavelengths.

1.6%. The three elliptical closed curves are the 3 dB, 6 dB, and the 9 dB iso-intensity curves which are discussed below.

The scatterer at the focal point moving perpendicular to the sound beam axis will experience a 180 degree phase shift as the scatterer passes through the first node in the field pattern. Hence an echo from the scatterer at the focal point will be 180 degrees out of phase with the echo from the scatterer at a position above the first node (but below the second node). The correlation algorithm will determine the shift between the echoes to be one-half of a wavelength in error, resulting in an incorrect velocity measurement. To keep the axial scatterer at the focal point from undergoing a phase reversal, the lateral motion must be less than the distance to the first node ($1.185 BW$, where BW is the 3 dB beam width of the sound beam) which can be achieved by controlling the time between pulses. Using the worst case experimental parameters of this study, that is, the narrowest beam width of 2 wavelengths, the greatest viewing angle of 75 degrees, and a nominal shift in the two successive echoes of 0.7 wavelength, the perpendicular change in position of the scatterer at the focal point is $0.65 BW$. For the viewing angle of 45 degrees, the perpendicular change in distance reduces to $0.175 BW$.

The lateral intensity field pattern of an ideal spherically focused transducer in a nondispersive and nonattenuating medium at the focal point is an Airy distribution, $[2J_1(r)/r]^2$ [20]. When the same transducer is used for transmission and for reception (as in this study),

the returning intensity will again be modulated by the field pattern. Hence the returning intensity is governed by $[2J_1(r)/r]^4$. The fraction of energy received from a circle centered on and perpendicular to the beam axis at the focal length can be determined by the following expression:

$$\frac{\int_0^{r_0} 2\pi r \left(\frac{2J_1(r)}{r} \right)^4 dr}{\int_0^{\infty} 2\pi r \left(\frac{2J_1(r)}{r} \right)^4 dr} \quad \text{Eq. (II.9)}$$

The $2\pi r$ term in the integral is the contribution due to the axially symmetric infinitesimal ring of constant intensity. The results of the integration are listed in Table II.1.

Table II.1

Percentage of received energy from various diameters of cross section in the focal region of a spherically focused transducer. The diameter is measured in terms of the 3 dB beam width (BW) of the sound beam. The number in parenthesis is the amount in dB that the intensity of the sound field is reduced from the value at the focal point.

Diameter	Energy (percentage of total)
1.00 BW (3 dB)	78.0
1.37 BW (6 dB)	95.1
1.63 BW (9 dB)	98.8
2.39 BW (first node)	99.7

The diameters of the circles are listed as the distance from the axis to the point that the intensity drops to the listed level. Note that about 1% of received energy is from outside the 9 dB boundary. For the scatterer in the neighborhood of the node, a phase reversal will occur but the amplitude of the echo will be very small and hence undetectable.

The amplitude modulation plays no role in the correlation procedure since the correlation of a function with the scaled version of itself is equal to the scaled autocorrelation function. The location of the maximum of a function is not affected by scaling in the absence of noise.

A transducer with a focal length to diameter ratio of 2 has a 3 dB lateral width that is 16 times smaller than the axial length, this corresponding to the most strongly focused field used in this study. Thus, the modulation along the transducer axis is minor compared to the modulation in the lateral direction.

D. Limitations of the Correlation Method

At this point in the discussion it is necessary to define the term "range cell." The range cell is the volume of scatterers that contributed detectable amounts of energy to the energy contained in the windowed segment of the echo.

In this section the limitations of the correlation method are discussed. These limitations arise from the windowing process, from the variation in speed of scatterers within the range cell, from the beam width modulation of the echo amplitude as the scatterer moves through the sound beam, and from the received energy from scatterers located outside of the range cell.

In order to find range information concerning the speed of the scatterers, the received echoes must be windowed at the desired range. This causes several types of errors:

- 1) A windowed waveform does not necessarily have its maximum correlation at the actual shift.

- 2) The range cell has scatterers which move at different velocities. Thus, successive waveforms will not only be shifted (by the average velocity of the scatterers) but also will be distorted.
- 3) A range cell will contain ultrasonic energy from a band of scatterers at the given range. Since the ultrasonic pulse burst is of nonzero duration, the trailing edge of the pulse brings energy from scatterers in front of the range cell into the range cell. The energy from the scatterers at the end of the range cell will be truncated by the window.
- 4) The nonzero width of the sound beam will pick up energy from outside the 3 dB beam width of the ultrasonic beam and hence the signal is potentially modified by scatterers moving at different speeds than those contained within the 3 dB beam width.
- 5) As the scatterer moves through the beam, the scattered sound is modulated by the field pattern of the ultrasonic transducer. Those scatterers which are entering the beam will produce echoes increasing in strength as they near the beam axis and vice versa. Hence two successive echoes will appear as modified versions of each other and not as simply shifted.

1. Error Associated with Windowing

The correlation procedure discussed in Section B will not in general give the exact amount of shift between the windowed portion of the first echo with the second echo. The procedure is exact when the window contains all of the first echo; the two echoes are identical except for the time shift. However, since a portion of the first echo must be windowed out in order to gain range information, the procedure will not give, in general, the exact shift (even if the two echoes are identical). For this discussion the second echo will be assumed to be identical to the first so that this source of error can be studied independently of errors resulting when the echoes are not identical. These errors are discussed later in this section.

Computer analysis of the shift between the windowed range cell of the first echo with itself (first and second echoes are identical) using Eq. (II.2) shows that the estimate is unbiased (the error in the estimate of $\hat{\tau}$ is zero) and that it has a nonzero variance. In the above referenced program, echoes are simulated by passing numerically generated Gaussian random numbers (see Chapter III) through a 6 pole Chebyshev digital filter (with 1 dB of ripple in the pass band). There are 32 sample points per period of the center frequency of the filter. The correlation is done by numeric integration. Since the shifts are random (because the echoes are random), a large number of echoes are used to achieve a better statistical estimate of the variance of the shifts. The number of echoes used was selected by using a number so large that doubling the number of echoes resulted in no statistical difference at a 99% confidence level. The number of echoes used was approximately 16384. The term jitter will refer to the standard deviation of the estimate of the shift expressed in wavelengths. This is the average amount that the estimate of shift varies with respect to the mean of the estimate from sample to sample. The mathematical expression for jitter is

$$\text{jitter} = \sqrt{E[(\hat{\tau} - E[\hat{\tau}])^2]} \quad \text{Eq. (II.10)}$$

where $E[.]$ is the expectation operator.

Figure 7 shows the results of a computer simulation of the jitter vs. correlation length for various system Q's (the experimental system has a Q of 4). The correlation length is

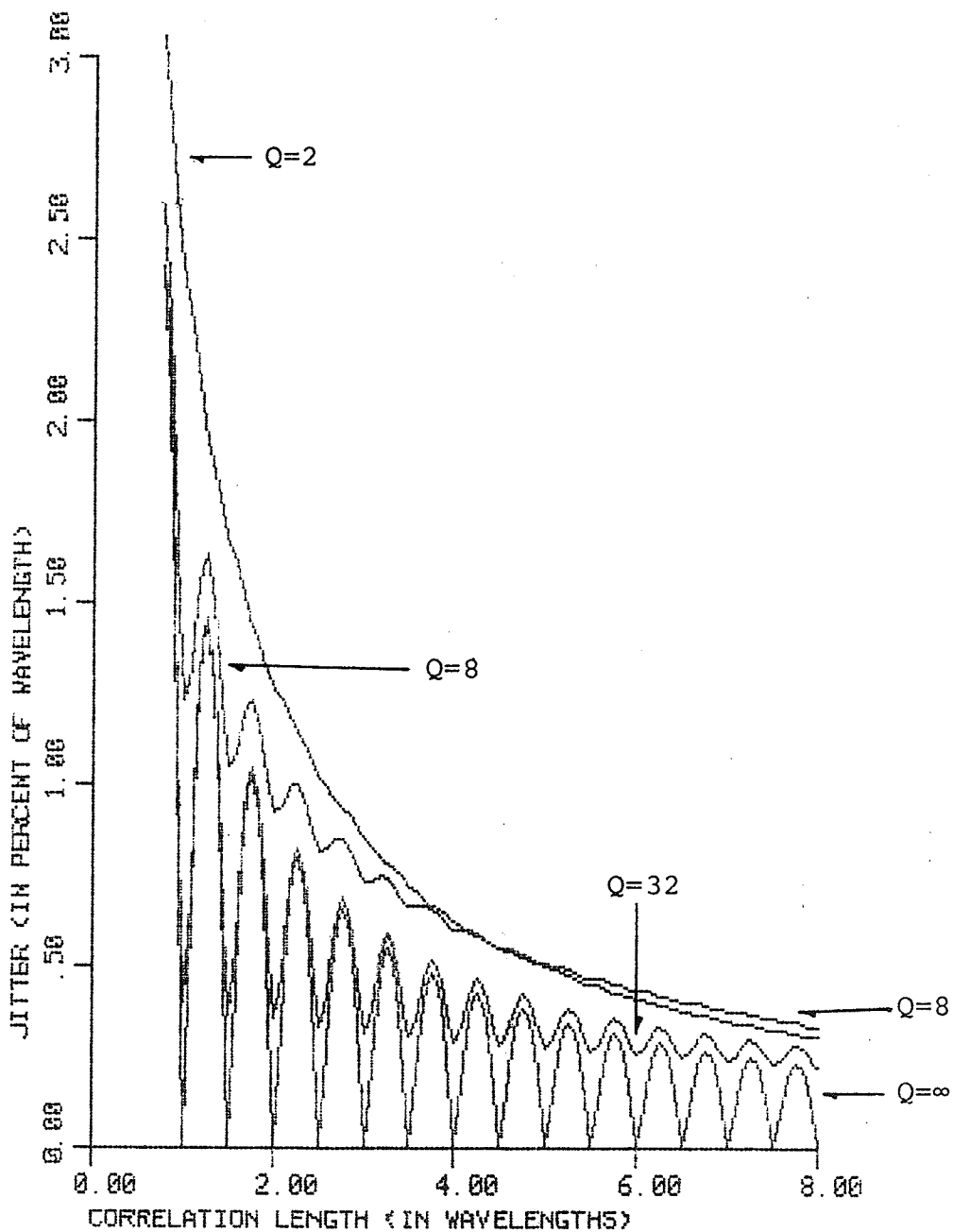


Figure 7. A graphical representation of the jitter as a function of correlation length for four system Q's.

expressed in wavelengths of the center frequency of the ultrasonic pulse along the horizontal axis. The different system Q 's were simulated by adjusting various coefficients in the digital filter. It can be seen in Figure 7 that, as the correlation length increases, there is a general tendency for the jitter to decrease. This happens because the correlation more closely approximates the autocorrelation function (which has zero jitter in the estimate of actual shift) as the correlation length becomes greater. The bottom curve of Figure 7 represents a BPWGN signal with an infinite Q (that is purely sinusoidal). In this curve the series of minima and maxima that the jitter goes through as the correlation length increases is due to the jitter being minimum when a correlation length of an integer half wavelength is chosen and maximum when the correlation length is an odd integer multiple of a quarter wavelength. The next curve from the bottom is for a BPWGN signal with a Q of 32. The minima and maxima occur in approximately the same positions as those of the infinite Q BPWGN case since with a Q of 32 the waveform will closely resemble a slowly modulated sinusoid. As the Q decreases further, the minima and maxima lose their identity but the jitter does not continue to increase (as Figure 7 appears to suggest). To demonstrate this, the jitter vs. Q for various correlation lengths is shown in Figure 8. The correlation lengths are chosen as the worst case lengths for the pure sinusoid case (the lengths that give the largest local jitter).

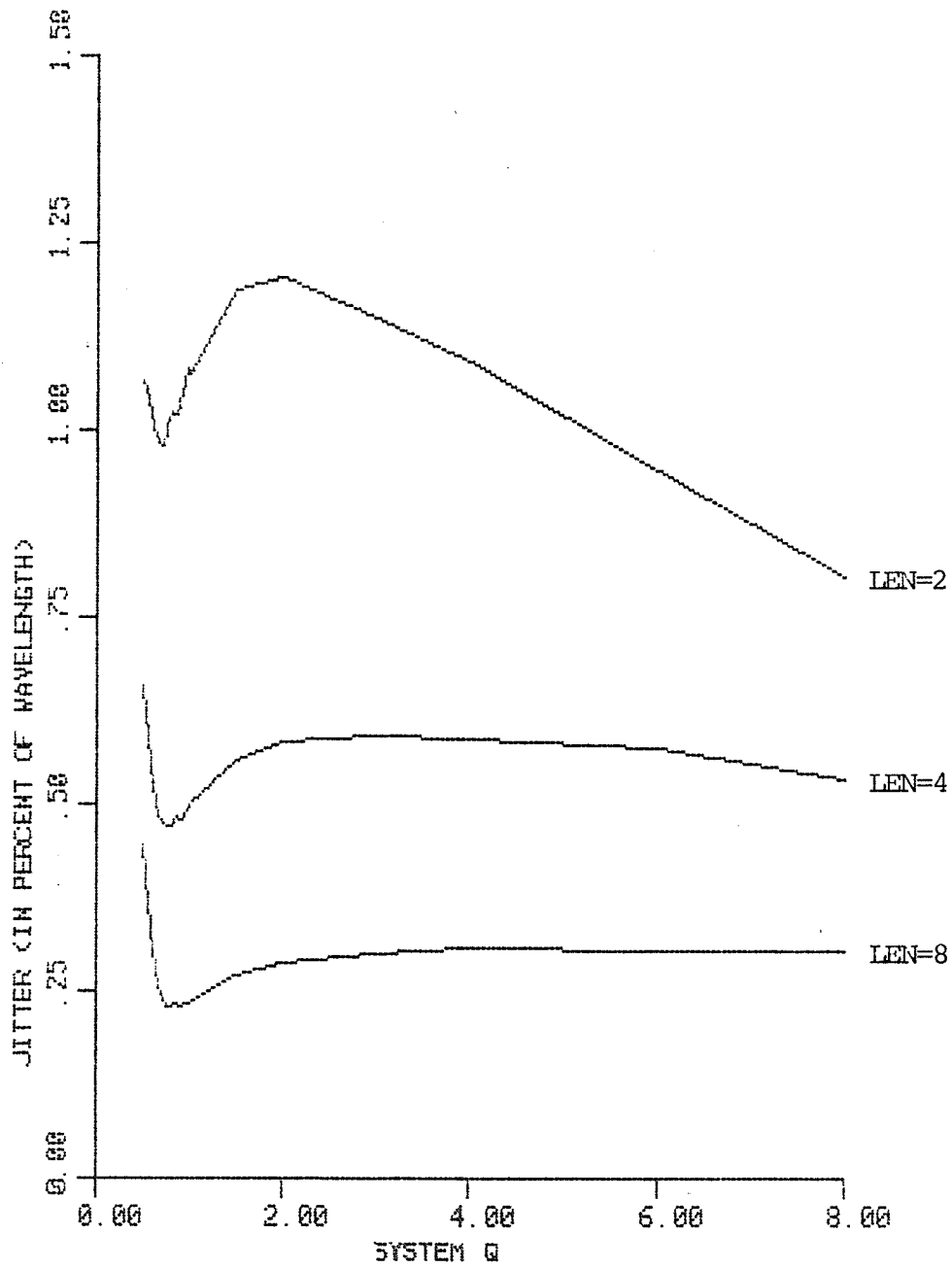


Figure 8. A graphical representation of the jitter as a function of system Q for three different correlation lengths (LEN).

2. Jitter Associated with a Velocity Gradient within the Range Cell

The scatterers within a range cell will be moving at different velocities since the velocity flow profile across the vessel is not necessarily uniform (it should be parabolic in the case of fully developed laminar flow). A velocity gradient occurs in the situation in which the scatterers are moving at a different velocity in one part of the range cell to that in another. When the flow profile is not uniform, only part of the range cell in the first echo will line up with the corresponding part in the second echo. The other parts of the signal of the first echo will not be perfectly aligned with their corresponding parts in the second echo since these parts come from scatterers that are moving with different velocities.

One measurement of the velocity gradient across a range cell is the distance that the fastest scatterer in the range cell gains over the slowest scatterer in the time interval between successive echoes. The distance gained will be defined as the amount of separation or symbolically $S(r)$. Separation will be determined analytically for fully developed laminar flow [21] which is described by the following expression and graphically displayed in Figure 9:

$$V(r) = V_{\max}[1-(2r/D)^2] \quad \text{Eq. (II.11)}$$

where

$V(r)$ = Radial velocity profile,
 V_{\max} = Axial velocity in wavelengths per unit time,
 D = Diameter of vessel in wavelengths, and
 r = Radial variable.

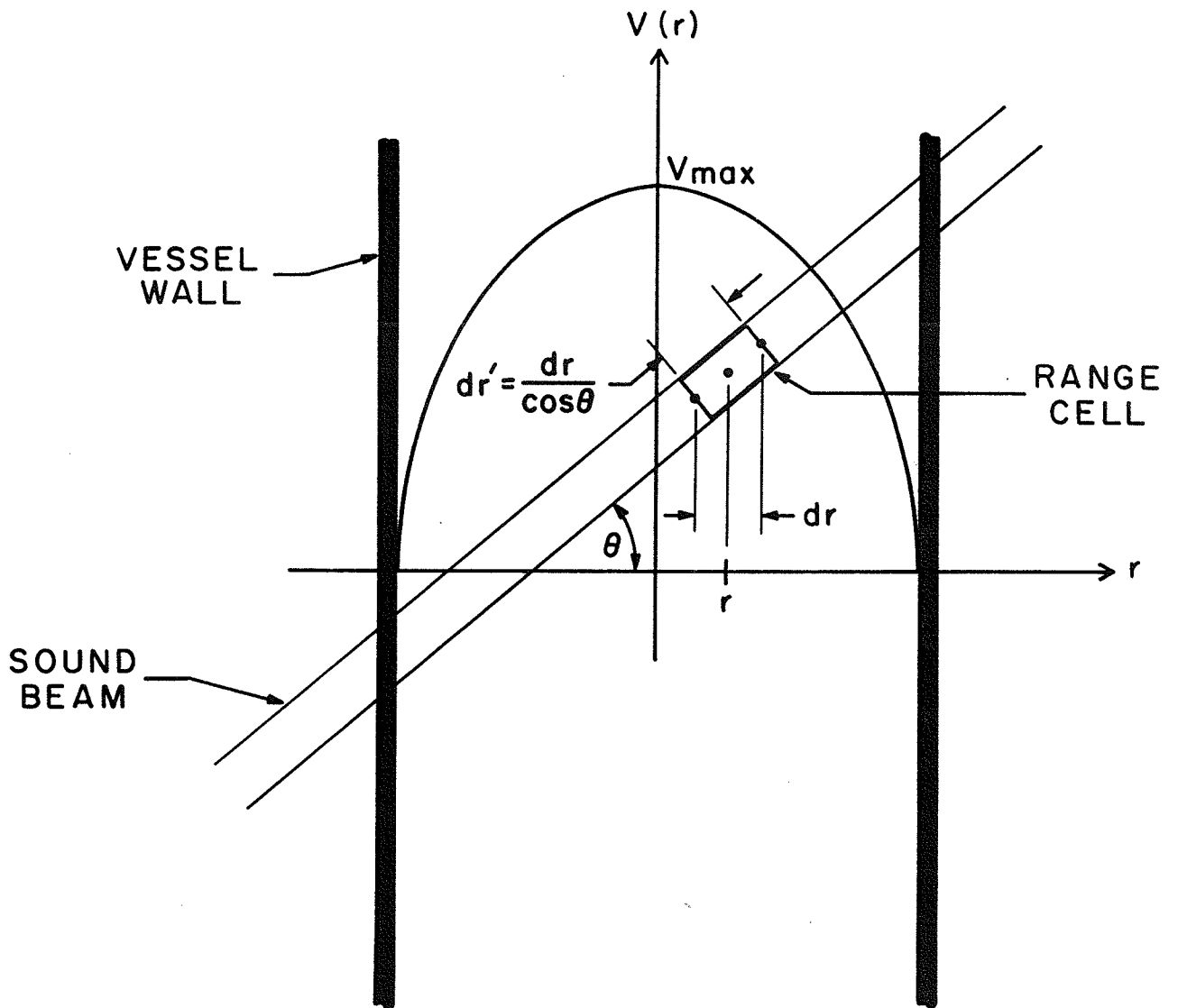


Figure 9. Geometry used in the derivation of the jitter resulting from separation.

The center of the range cell is at r and has width dr . The change in distance experienced by the scatterers at the end of the range cell compared to those at the beginning of the range cell in time T is

$$S(r) = T \left[V \left(r + \frac{dr}{2} \right) - V \left(r - \frac{dr}{2} \right) \right] \quad \text{Eq. (II.12)}$$

For smaller dr the above expression can be simplified by approximating the difference as a derivative times dr .

$$S(r) = T \frac{d}{dr} V(r) dr = -4(TV_{\max}/D) (2r/D) dr \quad \text{Eq. (II.13)}$$

Note that the worst separation occurs at the walls of the vessel (where $r=D/2$). The equation for $S(r)$ can be put in terms of experimentally measurable parameters. TV_{\max} is the amount that a midstream scatterer moves in time T ; however, the TDM measures directly the amount (in wavelengths) the scatterer has moved along the transducer axis or $2TV_{\max}\cos(\theta)$ Eq. (II.6). Calling this quantity s , and rearranging yields $TV_{\max}=s/(2\cos(\theta))$. The value dr can be replaced by the range cell axial length scaled by $\cos(\theta)$ or $dr=dr'\cos(\theta)$ where dr' is the length of the range cell. The separation equations can now be written in terms of directly measurable quantities:

$$S(s) = 2(s/D) (2r/D) dr' \quad \text{Eq. (II.14)}$$

A computer simulation has been used to estimate the degree of jitter due to different velocity gradients across the range cell. For this simulation, the scatterers at the edge of the range cell nearest to the transducer are taken to

have the lowest velocity; the scatterers at the farthest edge are assumed to have the highest velocity. The scatterers between these two edges are assumed to have velocities that increase linearly with depth into the range cell. The simulation consists of a range cell with spatially but randomly distributed scatterers with Gaussian random amplitudes after the model in Section A. The simulation then produces a second range cell by moving the scatterers in the first range cell by a distance proportional to their speed. Then both range cells are passed through the digital filter described in Part 1 of this section and correlated to determine the shift. To decrease the error of the estimation of the jitter due to this effect, a large number of samples were used as in Part 1 of this section. The number of echoes needed are 16384. The results are represented in Figure 10 where the jitter is plotted as a function of correlation length for various scatterer separation distances ($Q=4$). Note the effect of the finite correlation window length in the bottom curve (zero separation) of Figure 10. If the error associated with windowing were not present, then the $s=0$ curve would lie on the horizontal axis.

The jitter of systems as a function of Q is shown in Figure 11. Here the separation was arbitrarily chosen as 0.125 wavelength and the correlation lengths used were 2, 4, and 8 wavelengths. From the figure it can be seen that increasing the value of the system Q or decreasing the correlation length results in increasing the jitter.

Consider a typical experimental arrangement using a 24

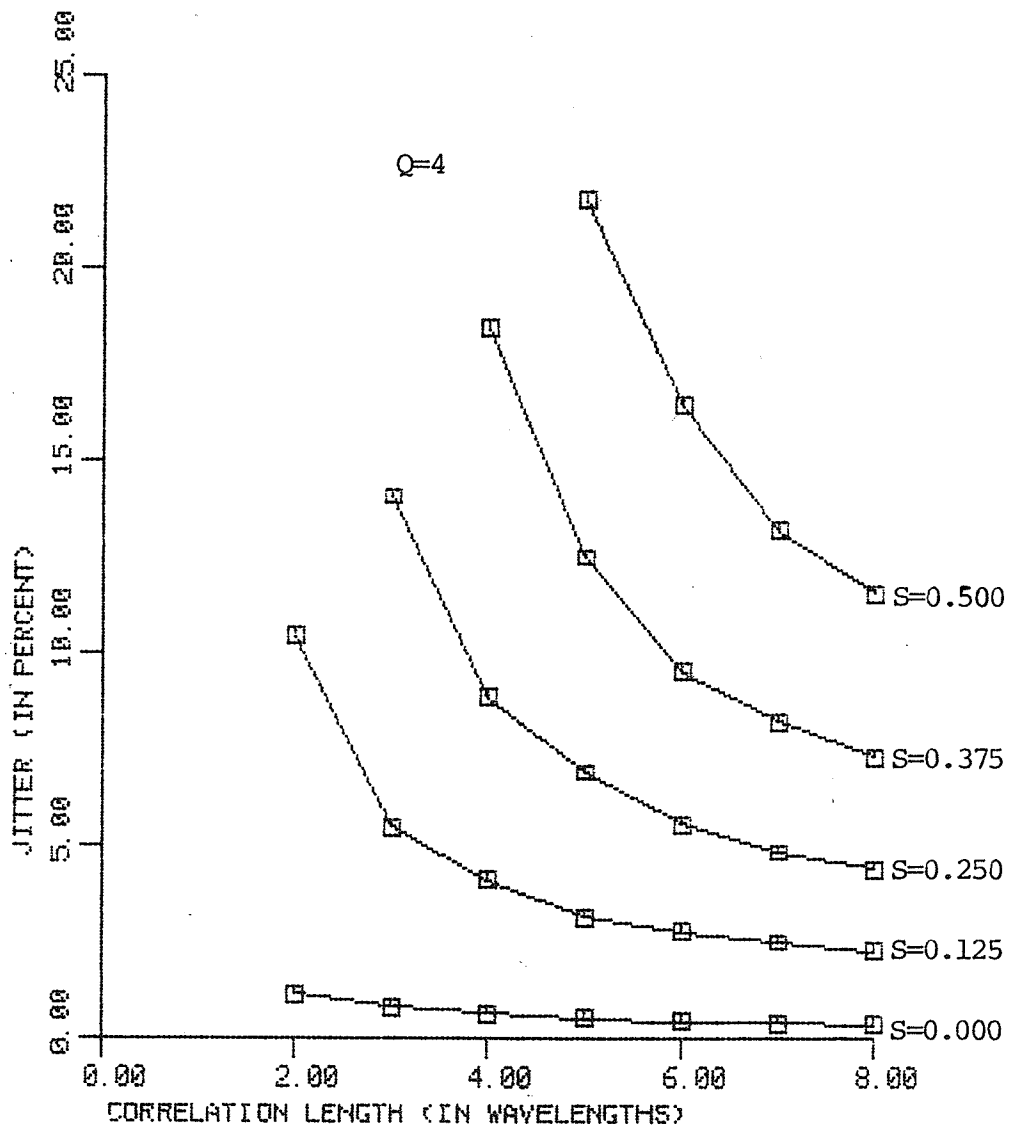


Figure 10. A graphical representation of jitter as a function of correlation length of five scatterer separation distances (S) where distances are measured in wavelengths.

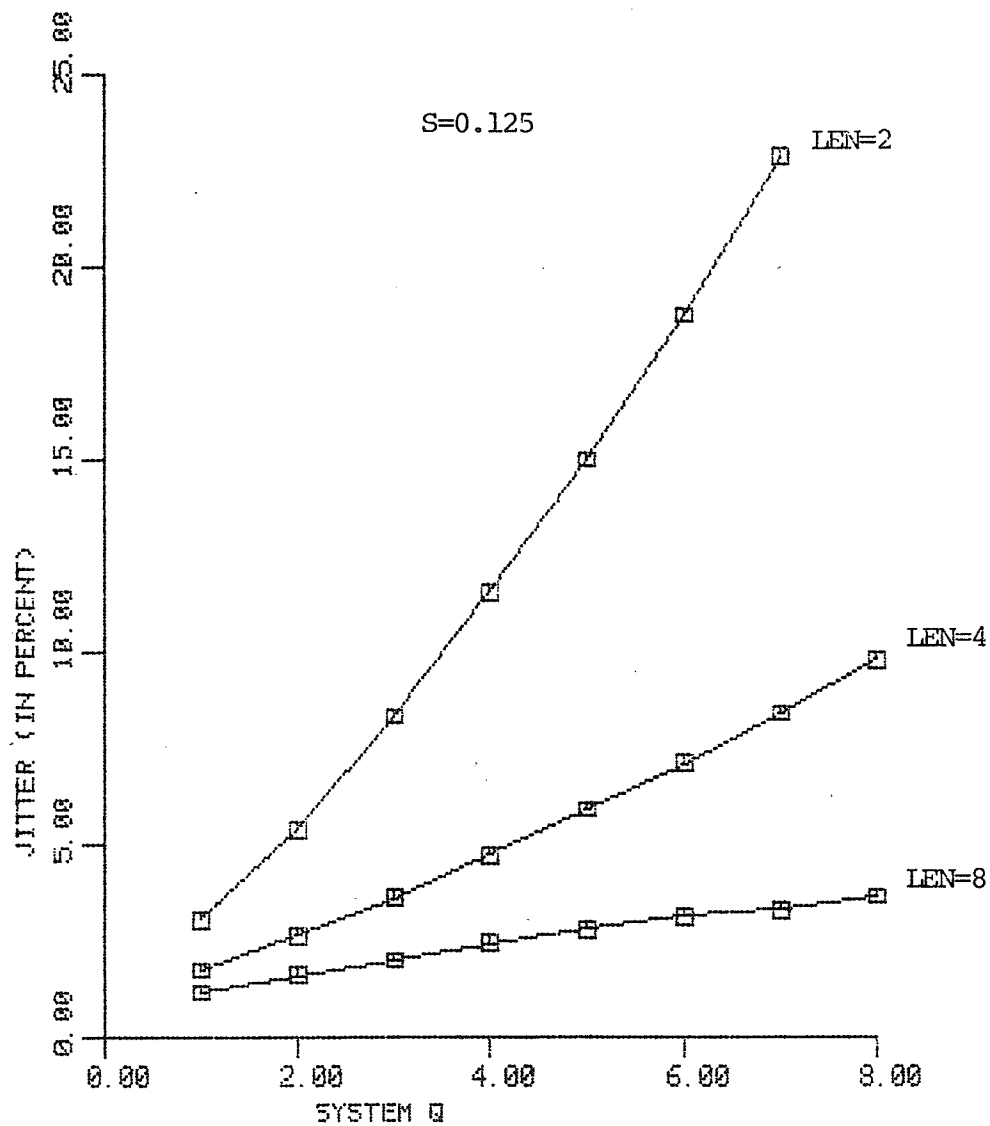


Figure 11. A graphical representation of jitter as a function of a system Q for a separation distance (S) of 0.125 wavelength for various correlation lengths (LEN).

wavelength diameter vessel (6.96 mm) inclined at 45 degrees with respect to the transducer, an ultrasonic pulse burst with a center frequency of 5 MHz, a Q of 4, a measured s of 0.7 wavelength, a range cell length of 8 wavelengths, and a speed of sound of 1500 m/s in the medium. The separation would be 0.47 wavelength at the vessel wall. The jitter associated with the velocity estimate from Figure 10 is 6% of a wavelength. As will be shown in Chapters III and IV, this source of error accounts for most of the jitter predicted from the simulation and measured experimentally near the edges of the vessel wall. The error becomes smaller as the range cell nears the axis (zero error at the axis).

3. Jitter Associated with Nonzero Time Duration of the System Impulse Response Velocity Gradients

The acoustical length of the range cell (the axial length of the volume of scatterers contributing to the energy in the range cell) is in part determined by the impulse response of the system. For example, if a very narrow window is used to create a range cell out of the echo, the energy in the range cell will be from a group of scatterers spread over a length comparable to the system impulse response at the range of the window in the medium. Hence, the impulse response has the effect of increasing the acoustic length of the range cell which allows for greater corruption from velocity gradients. This is evident from Figure 11 in that as the system Q increases the jitter increases. (A higher system Q results in a greater temporal duration.) In addition, the estimate will also lose range resolution

(smooth out detail) since the estimate of the shift will be averaged over all the scatterers delivering energy at a particular range. The exact amount of smoothing due to the impulse response of the system is difficult to derive analytically. However, in Chapter VI the effect of smoothing is demonstrated in Figure 40 (page 142) by computer simulation (Chapter VI contains results of the computer simulation that are not verified in Chapter V). For good range resolution the impulse response must have the lowest possible temporal duration. The half power width and 95% power width of the impulse response for various system Q's are expressed in wavelengths of the center frequency in Eq. (II.15) (the passband is assumed to be a 6 pole bandpass Chebyshev response with 1 dB of ripple):

$$50\% \text{ power width} = 0.4046 Q \quad \text{Eq. (II.15)}$$

$$95\% \text{ power width} = 1.646 Q$$

These values were determined by numerically integrating the square of the impulse response for the digital filter used to synthesize the BPWGN with various Q's. The jitter from the nonzero duration impulse response is significant near the sides of the vessel where the velocity gradient is greatest (see Figure 40). The finite impulse response plays a lesser role midstream in the vessel than at the sides unless the response is so great as to bring velocity information in from other parts of the vessel (see Chapter VI, Figure 40). This is because the midstream velocity profile is rather uniform.

4. Jitter Associated with Nonzero Beam Width and Velocity Gradients

The nonzero time duration of the impulse response makes the system sensitive to the scatterers along the beam axis. The nonzero beam width makes the system sensitive to scatterers perpendicular to the beam axis. All ultrasonic transducers have a nonzero beam width. Hence, the scattered ultrasound in a certain range cell will be the result of scattered ultrasound from all scatterers in the plane perpendicular to the axis of the beam and intersecting the axis at the particular range being windowed. Here the beam is assumed to be planar in the focal region. Hence the effect of a nonzero beam width is similar to the jitter of the nonzero duration impulse response. That is, near the sides of the vessel where the velocity gradients are greatest, the nonzero beam width effects will bring in more contradictory information on the velocity of the scatterers, thus corrupting the shift estimation. Near the center where the flow is more uniform the nonzero beam width plays a lesser role. The error is difficult to determine analytically. However, in Chapter VI (Figure 38, page 139) this error will be studied by computer simulation on the velocity determination across a vessel with parabolic flow profile for various sized beam widths. The estimate will be biased towards the average velocity of the scatterers contained in the plane and intersecting the beam.

5. Jitter Associated with Intensity Modulation Across the Beam

A scatterer that passes through a spherically focused sound beam will scatter ultrasonic energy proportional to the ultrasonic intensity at the position of the scatterer. The intensity of the scattered energy will increase as the scatterer nears the axis of the beam and will decrease as the scatterer moves away from the axis. With many scatterers in the beam, some will be approaching the axis and some will be moving away from the axis. This will be referred to as beam width modulation.

Two successive echoes will not appear identical since some of their constituent scatterers will have increasing amplitudes (those nearing the axis) and other scatterers will have diminishing amplitudes. The error in the estimation of the shift between two successive echoes due to beam width modulation is difficult to determine analytically. However, the error can be estimated through a simulation where the scatterers are moved in fixed amounts perpendicular to the beam axis between successive echoes. In the simulation, the beam width modulation error as a function of correlation length was studied. The scatterers were assumed to be moving perpendicularly to the ultrasonic beam axis with constant speed. This ruled out errors due to velocity gradients and simplified the alignment procedure in the program; two successive range cells should have no shift between them because there was no scatterer motion along the axis. A range cell was constructed with a length long enough to

accommodate the largest correlation length and impulse response of the system. In the range cell, the location of a large number (1024) of scatterers was randomly distributed (all locations in the cell had an equal probability of being occupied by a scatterer). The lateral extent of the range cell was limited to the first node in the Airy pattern formed by an ideal spherically focused transducer. Each scatterer in the range cell was assigned a random Gaussian amplitude generated by a random number generator. A second range cell was constructed from the first by translating the positions of all the scatterers of the first by the same perpendicular distance. Various distances were tried (see Figure 12). The amplitudes of each of the scatterers in each echo were scaled by the square of the Airy function (same transducer for transmission and reception) according to their perpendicular distance from the beam axis. Next, both range cells were passed through the digital filter mentioned in Section II.C.1. The Q of the filter was 4 (the same as the experimental system). The range cells were aligned by the correlation procedure and their shift deviation from zero shift was determined by averaging the results of a large number of independent trials. The number was chosen by the method described in Part 1 of this section. The number of trials was 16384. The jitter in the estimate of the shift from beam width modulation is graphed in Figure 12. The jitter (in percentage) is presented as a function of the fractional amount of beam width that the scatterer moves for various correlation lengths. Note that for the case of no

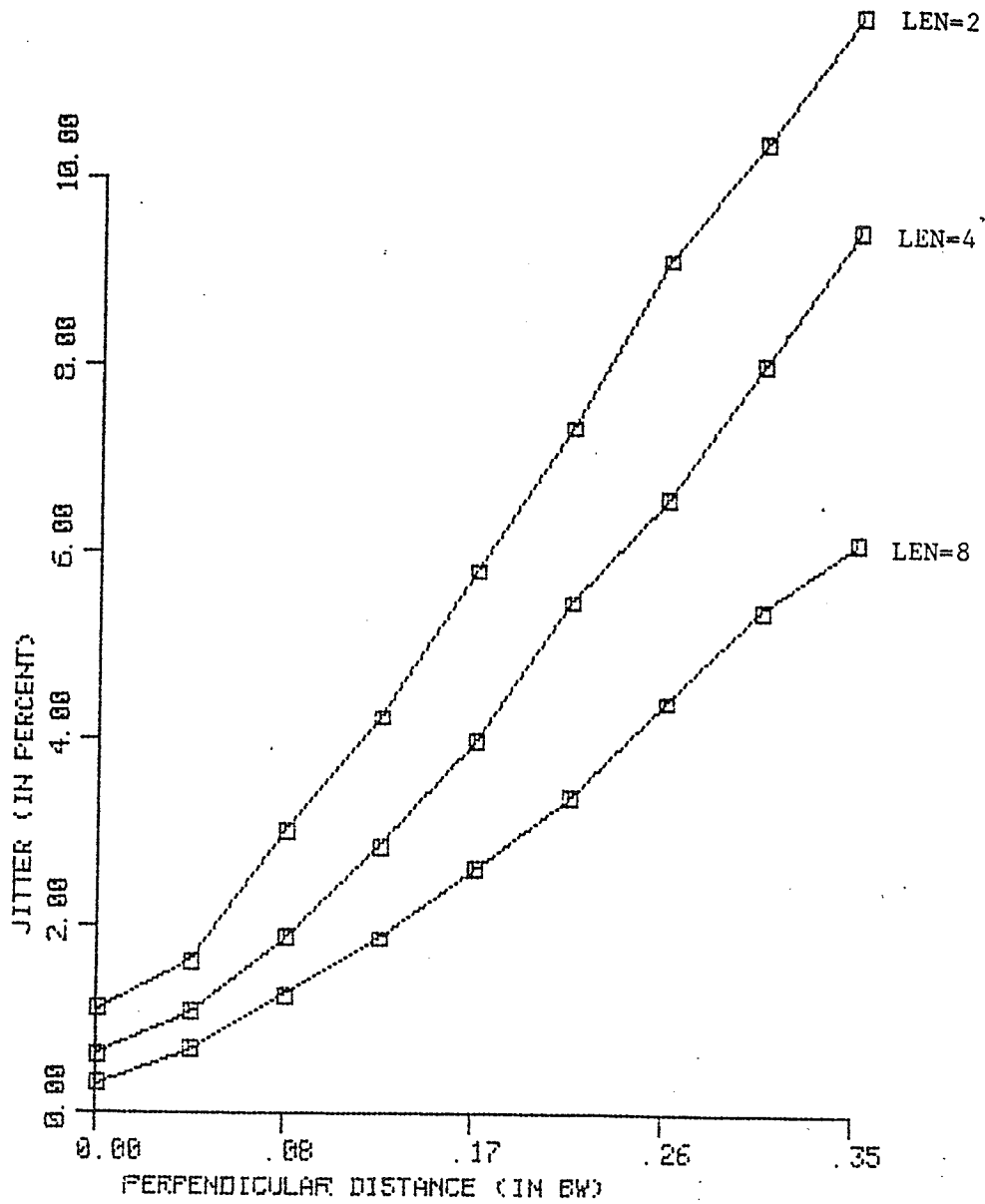


Figure 12. A graphical representation of jitter as a function of the distance the scatterer moves across the beam width for three correlation lengths (LEN).

scatterer movement, the jitter (the data on the vertical axis) reduces to the jitter associated with the correlation length effect.

E. Determination of the Viewing Angle

In this section the dependency of the viewing angle (θ in Figures 4 and 13) on the correlation coefficient of the two aligned windowed data sets of the two echoes will be demonstrated. Ideal sound and velocity fields will be assumed to show that the viewing angle can be obtained from the statistics of the signals. An ideal sound beam is such that the lateral intensity distribution at all positions in the focal region is a cylinder of uniform intensity within the beam width and zero intensity outside the beam width. The phase fronts inside of the beam width are assumed to be planar and equally spaced. An ideal velocity field is such that the velocity is uniformly the same throughout the entire field. The range cell is chosen to be much longer than the impulse response of the system. This has the immediate effect that the signals from the scatterers preceding and following the range cell are sufficiently small that they do not contribute appreciably to the range cell signal. Hence, the truncation effects of the range cell on the nearby scatterers can be ignored.

Let us first view the idea of the approach qualitatively for the two viewing angle extremes. Suppose that the velocity vector of the scatterers is directed along the ideal sound beam axis ($\theta=0$ degrees). Then the range cell of the first echo will look identical to the aligned range cell of

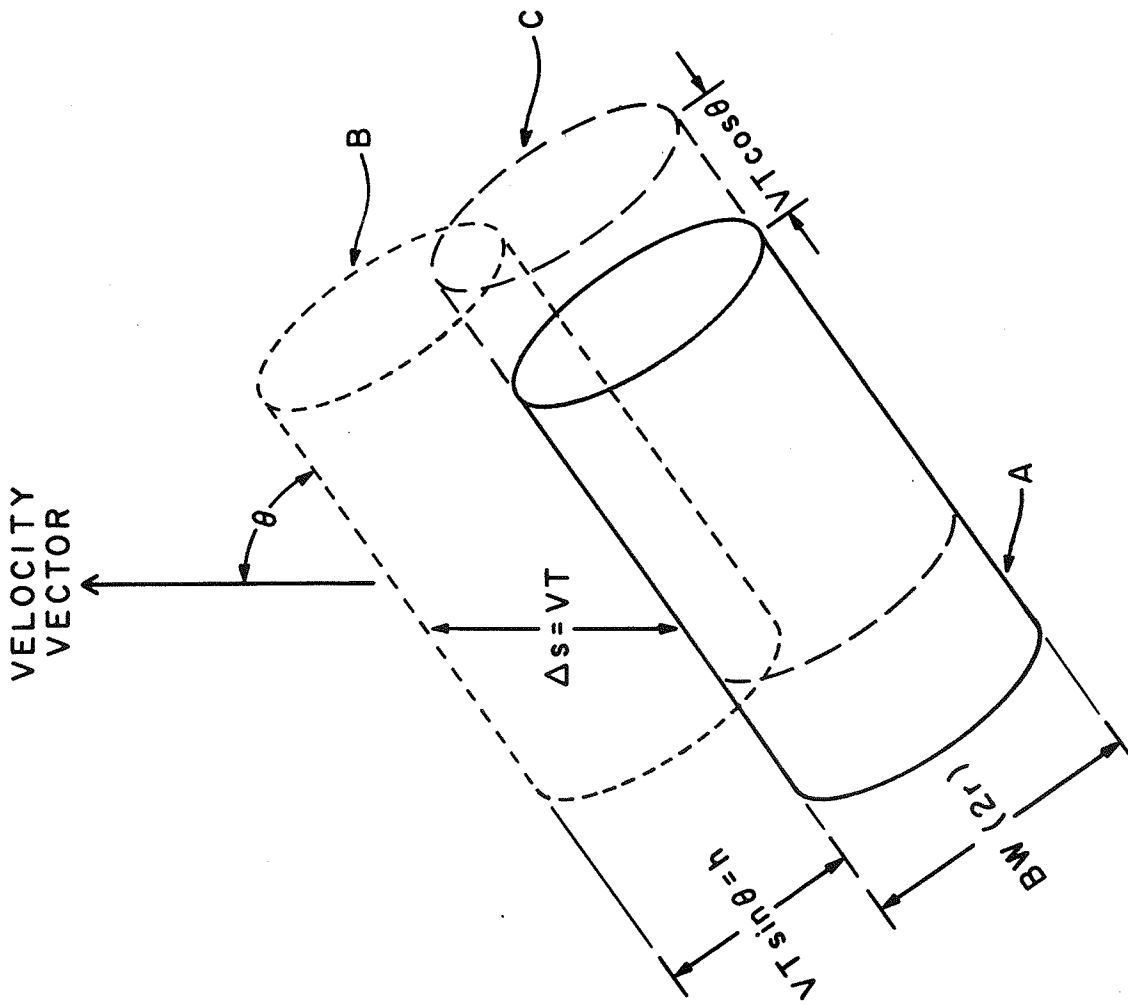


Figure 13. A schematic representation of the sound beam relative to the direction of flow of the scatterers for the determination of the viewing angle. Here, BW is the ultrasonic beam width, V is the magnitude of the velocity vector of the scatterer, T is the time interval between two successive ultrasonic pulses, and θ is the viewing angle.

the second echo, since the position of the scatterers would have changed range only with respect to the transducer and would not have moved out of the beam. This would result in the highest degree of correlation between the two range cells. When the sound beam axis is perpendicular to the velocity vector ($\theta=90$ degrees), the range cell of the first echo would begin to lose its resemblance to the same range cell of the second echo (no alignment is needed since there is no flow along the axis of the beam), because new scatterers would enter the range cell as old scatterers exit. The rate at which the resemblance is lost is dependent on beam size, the viewing angle, and the amount that the scatterers move across the beam width between the two pulses. As the resemblance is lost the correlation approaches zero.

To examine further the dependency of the viewing angle (at other than either 0 or 90 degrees) on the degree of correlation between the two range cells, let the time interval between transmission of the two ultrasonic pulses be designated by T . During time T , the scatterers of the first range cell (cylinder A in Figure 13) have moved a distance VT (cylinder B in Figure 13). The correlation method will align the first range cell (cylinder A) with the second range cell (cylinder C). The alignment is the result of sliding a range cell along the beam axis until the scatterers of the second range cell align in range with the scatterers of the first range cell (those that are still in the beam). The scatterers that the two range cells do not share are uncorrelated and hence do not contribute to the alignment

procedure.

To examine this quantitatively, equations for the two range cells are needed. Each range cell consists of the sum of the individual echoes (replica of the system impulse response $h(t)$) from each of the scatterers in the range cell. Expressed mathematically, the waveform of the first range is represented by

$$U(t) = \sum_{i=1}^N A_i h(t-t_i) + \sum_{i=N+1}^M A_i h(t-t_i) \quad \text{Eq. (II.16)}$$

where A_i is the scattering strength of the i^{th} scatterer, M is the number of scatterers in each range cell (both should have approximately the same number), N is the number of scatterers common to both range cells, t is time with $t=0$ at the beginning of the range cell, and t_i represents the range of the scatterer. The aligned second range cell is represented by

$$V(t) = \sum_{j=1}^N A_j h(t-t_j) + \sum_{j=N+1}^M B_j h(t-t_j) \quad \text{Eq. (II.17)}$$

where B_j is the strength of the j^{th} scatterer of the second range cell which is not found in the first range cell. The cross correlation between $U(t)$ and $V(t)$ is given by the following

$$R_{UV} = \int_{-\infty}^{\infty} U(t)V(t)dt = \sum_{i=1}^N A_i^2 \int_{-\infty}^{\infty} h^2(t-t_i)dt \quad \text{Eq. (II.18)}$$

The A_i and the B_i are zero mean random variables (see Section A of this chapter). The contributions from the cross terms are uncorrelated and assumed to be negligible. By making the change of variables $s=t-t_i$ for the i^{th} integral, the summation reduces to

$$R_{UV} = \sum_{i=1}^N A_i^2 \int_{-\infty}^{\infty} h^2(s)ds \quad \text{Eq. (II.19)}$$

The integration and summation processes can be separated (separation of variables) yielding the following result

$$R_{UV} = \left(\int_{-\infty}^{\infty} h^2(s)ds \right) \left(\sum_{i=1}^N A_i^2 \right) \quad \text{Eq. (II.20)}$$

On the average, the value of the cross correlation is given by

$$E[R_{UV}] = \int_{-\infty}^{\infty} h^2(s)ds E\left[\sum_{i=1}^N A_i^2\right] = N\sigma^2 \int_{-\infty}^{\infty} h^2(s)ds \quad \text{Eq. (II.21)}$$

where $E[.]$ is the expectation operator and σ^2 is the variance of the strength of a scatterer. Note that on the average the cross correlation is directly proportional to the number of scatterers (N) that the two range cells share. A

convenient form for the cross correlation is found by dividing it by the maximum value it can achieve ($N=M$). Using this scaling factor and naming the result the correlation coefficient (ρ_{uv}), the following form is found

$$\rho_{uv} = \frac{N}{M} \quad \text{Eq. (II.22)}$$

From the above equation the correlation coefficient is the fraction of scatterers remaining in the second echo that was in the first range cell. Hence, the correlation coefficient is equal to the fractional volume that the two cylinders share. For cylinders with a radius r and an axial separation of h , the fractional common volume is given by the following expression and graphed in Figure 14.

$$\rho_{uv}\left(\frac{h}{2r}\right) = \frac{2}{\pi} \left[\tan^{-1} \frac{\sqrt{1 - \left(\frac{h}{2r}\right)^2}}{\frac{h}{2r}} - \frac{h}{2r} \sqrt{1 - \left(\frac{h}{2r}\right)^2} \right] \quad \text{Eq. (II.23)}$$

When performing the time domain technique, two data parameters are utilized: 1) the distance that the aligned range cell of the second echo has moved relative to the range cell of the first echo ($VT\cos(\theta)$) and 2) the correlation coefficient of the two range cells. From Figure 14 the equivalent lateral shift of the scatterers of the range cell of the first echo with the location of the same scatterers at a later time T can be extrapolated based on the correlation

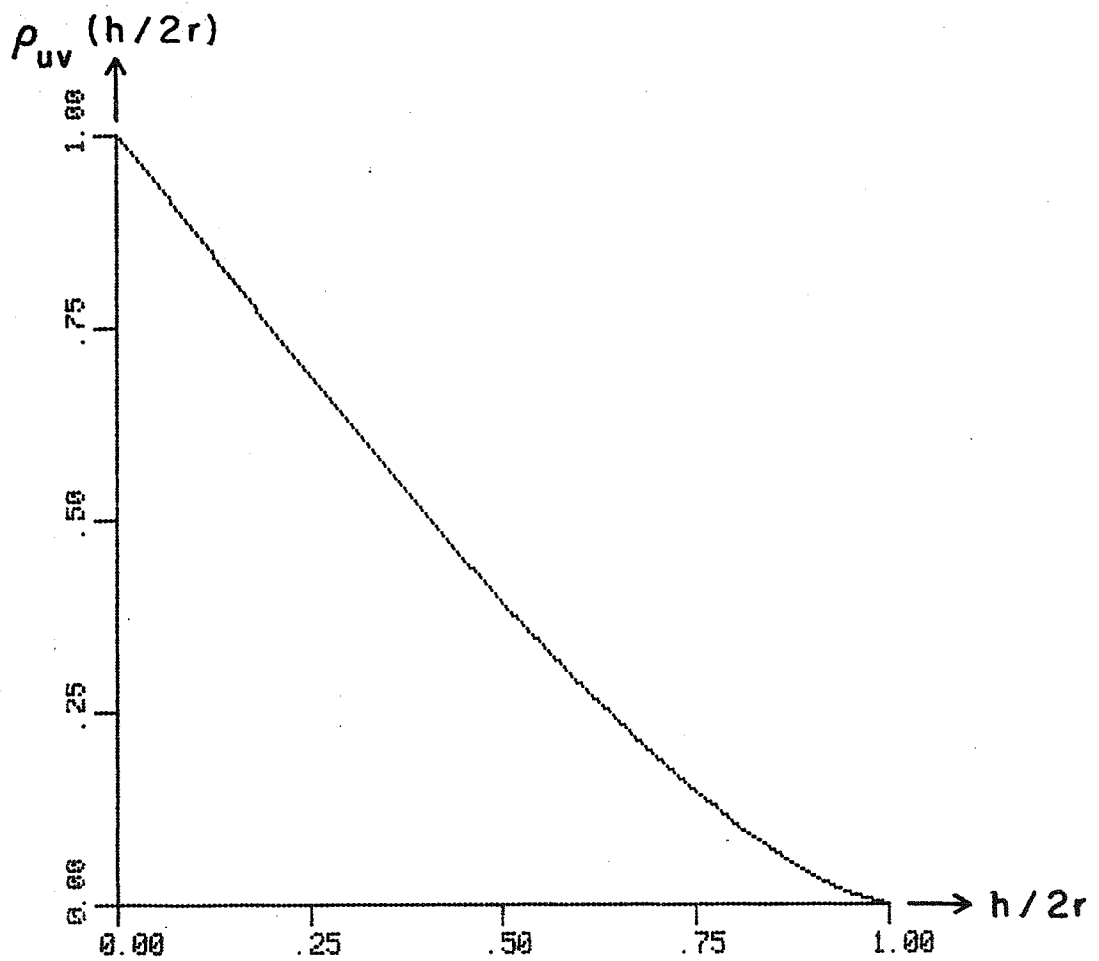


Figure 14. A graphical representation of the correlation coefficient as a function of the distance between the axes of the two ultrasonic beams and an ideal flow velocity field. The curve is the result of an ideal circular field pattern.

coefficient yielding $VT\sin(\theta)$. For example, if a correlation coefficient of 0.5 is determined, then from Figure 14 the value of $\frac{h}{2r} = 0.39 = \frac{VT\sin\theta}{2r}$ is obtained. From this information the two independent variables V and θ can be determined.

In practice the transducer has a beam pattern different from the above ideal one. But in order to implement this approach to determine the viewing angle from the statistics of the echo returns, one only needs to develop a lookup table (similar to that in Figure 14) for the particular transducer.

III. COMPUTER SIMULATION OF THE TIME DOMAIN METHOD FOR DETERMINING FLOW PROFILES

A computer simulation was performed in order to determine the effects of system parameters on the estimation of the velocity of the scatterers at various points across a vessel. The parameters which were varied included:

- 1) the vessel diameter,
- 2) the velocity profile across the vessel (radial symmetry is assumed),
- 3) the distance moved by a scatterer on the axis of the vessel in the time interval between pulse transmissions (axial position change, VT , see Figure 13).
- 4) the intensity pattern across the ultrasound beam (radial symmetry is assumed),
- 5) the system Q (normalized bandwidth),
- 6) the correlation length of the velocity estimation algorithm,
- 7) and the angle between the beam axis and the vessel axis (viewing angle).

All distance measurements are in wavelengths relative to the center frequency of the ultrasound pulse. In the following discussion Figure 15 will be a helpful guide. Here the axis of the vessel, defined as the z -axis, and the sound beam axis are in the xz plane. These two axes intersect at the origin. The width of the sound beam is BW and within the beam width the intensity is nonzero; outside the beam width it is assumed that no sound exists. The simulation does not include the effects of the wavelength becoming longer in the focal region. To compensate for this effect, the estimated velocity profiles graphed in the figures of this chapter should be scaled by $1-(a/2f)$ where a is the radius of the

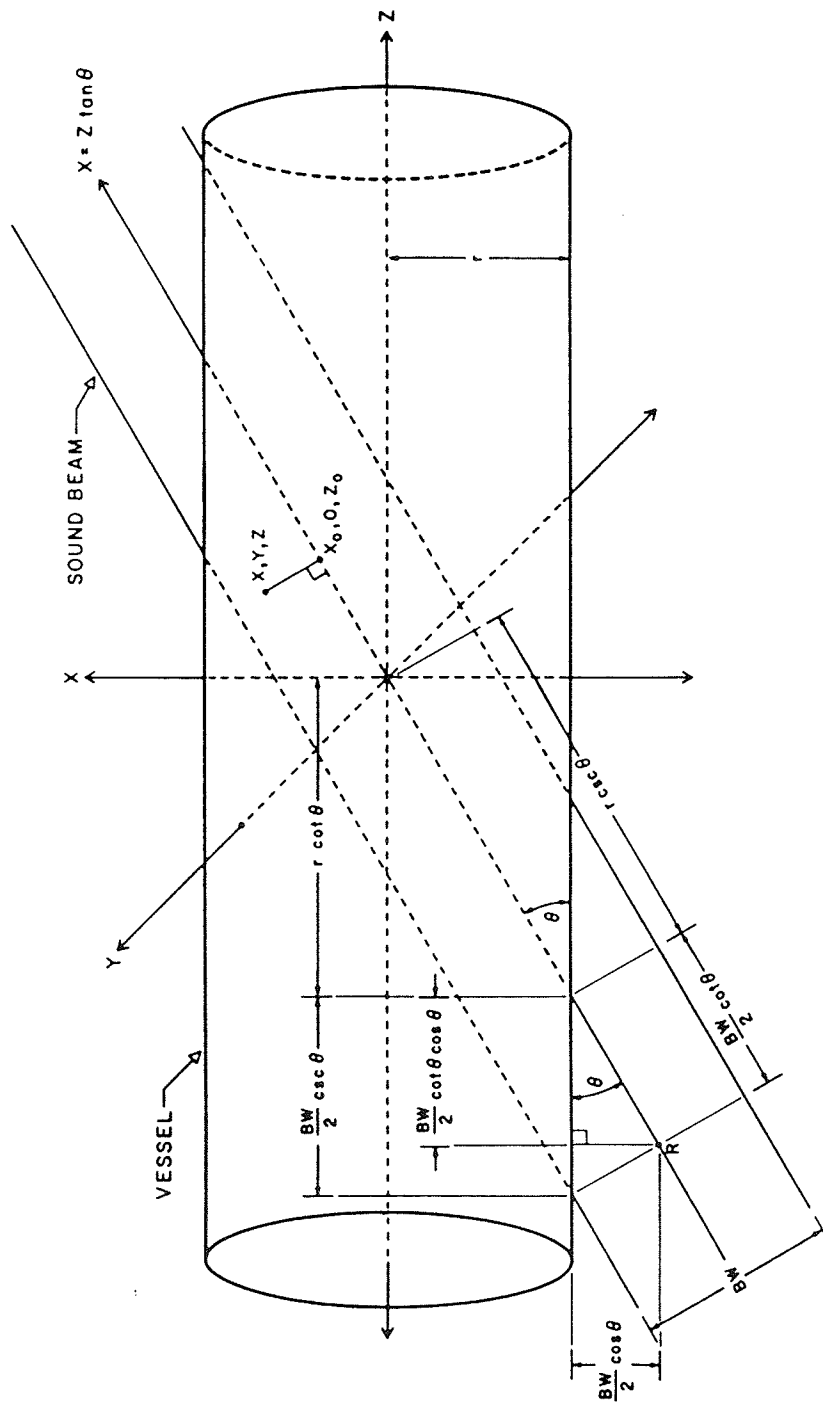


Figure 15. A schematic representation of the geometry of the sound beam and vessel used in the computer simulation.

transducer and f is the focal length (see Eq. (II.8)). The viewing angle is θ .

Execution of the simulation involved the following steps:

- 1) Input the seven system parameters listed above.
- 2) The scattering model discussed in Section A of Chapter II suggests that the scatterers are randomly located throughout the volume of the vessel with all positions having equal probability of being occupied by a scatterer. To simulate this model the simulation generates randomly distributed scatterers throughout the volume of the vessel length (the length of the vessel was chosen to be slightly longer than the length necessary to enclose the beam). The length of the vessel where the sound beam exists is from $-BW \cdot \csc\theta/2 - r \cdot \cot\theta$ to $BW \cdot \csc\theta/2 + r \cdot \cot\theta$.

Three random numbers are needed to define a scatterer's position (one coordinate per dimension). The random locations are generated by a random number generator. The uniformly distributed random number generator is modeled after the subroutine RANDU in the IBM Scientific Subroutine Package. For the largest vessel (24 wavelength in diameter) the number of scatterers in the sound beam (2 wavelength beam width) was 1024. Increasing the number of scatterers showed no statistical significance at the 99% confidence level over the 1024 number. The scatterers that fell outside

the sound beam were discarded (approximately 5% of the scatterers fell inside the beam, hence around 20,000 randomly distributed scatterers were generated per echo). For larger beam widths and for a smaller vessel the percentage of scatterers that fell inside the sound beam increased substantially.

- 3) The scattering model (Section A of Chapter II) requires that each scatterer has a randomly distributed Gaussian amplitude. Hence, a random Gaussian amplitude is assigned each scatterer contained in the vessel. The Central Limit Theorem states that the average of many random variables, regardless of their probability distribution, will result in the average being a Gaussian random variable [22]. Exploiting this idea, the simulation generates Gaussian random variables by averaging eight uniformly distributed variables. The probability distribution function of the eight was found to be sufficiently close to a Gaussian curve so that a larger number of averages was not needed. Also, extensive averaging will occur when the scatterers are passed through the digital filter (see below) and also during the correlation procedure; hence, even if the random variables were not Gaussian, the additional processing would make them more Gaussian.
- 4) The scattering strength of each scatterer must now be scaled by the field pattern of the transducer (beam width modulation). To determine the amount to scale the

amplitude of each scatterer, the perpendicular distance to the sound beam axis must be found. The modulation must be the square of the pressure field pattern since the same transducer is used for transmitting and receiving. The axial distribution of the sound beam is assumed to be uniform since the axial intensity pattern falls off much more slowly than the lateral intensity pattern. The simulation used the Airy function for the pressure field because this is the theoretical lateral distribution for a spherically focused transducer at the focal range [20]. Only the main lobe was used because the energy in the side lobes accounts for less than 0.3% of the total energy (see Table II.1). The side lobes showed no statistical difference at the 99% level from the results that used only the main lobe. For a scatterer at (x, y, z) the projection onto the beam axis occurs at $(\sin\theta \cdot \cos\phi \cdot (x \cdot \tan\theta - z), 0, \cos\theta \cdot (x \cdot \tan\theta - z))$ and is shown as $(x_0, 0, z_0)$ in Figure 15. The perpendicular distance is the distance between the two ordered triplets.

- 5) The range of each of the scatterers must be known in order to place the scatterer at the correct range in the echo. The transducer is located in the lower left of Figure 15. The range is at the intersection of the projection of each scatterer onto the sound beam axis. The range is the distance from R (the earliest possible location for a scatterer) to the projection point. The range must be multiplied by two to account for the round

trip length. In the simulation, the range was divided into 16 points per wavelength. The number 16 was used because any larger number of points per wavelength showed no statistical difference at the 99% confidence level. Once the range in wavelengths was determined, the range was multiplied by 16 (number of points per wavelength). The strength of the scatterer (amplitude and beam width modulation) was then shared by the two members in the array in which the range of the scatterer fell between. The weighting of the strength at a particular array member was determined by the fraction lost in the truncation. If the fraction was 0.5, then each member received half the strength; if the number was 0.25, then the first member received 75% of the strength and the second 25%, etc.

- 6) The second echo must account for the movement of each scatterer of the first echo during the time interval between the transmission of the two pulses. This is done in the following manner. The scatterer is moved the programmed amount and the strength of the scatterer stored in a second array. One of the parameters entered into the program is the amount a scatterer on the vessel axis moves in the time between the two echoes. With the profile known (also entered in the program) the amount that a scatterer anywhere in the vessel moves is determined. If the scatterer at (x, y, z) moves Δs amount, then the new position is $(x, y, z + \Delta s)$. The members of the second array were determined in the

same way as the first were by using the new ordered triplet.

- 7) To simulate the bandlimiting of the system both echoes (arrays) are passed through a digital filter (the same digital filter discussed in Chapter II). The Q of the filter was an input parameter.
- 8) To find the shift between the two echoes at various ranges the correlation algorithm in (B) of Chapter II is used. At wavelength increments across the vessel an estimate of velocity is taken. The length of the correlation was an input parameter.
- 9) Repeat steps 2-8 a sufficient number of times to obtain reasonable statistics of the velocity estimation algorithm (mean and variance at each wavelength across the vessel). The number of times was found to be 1024 (by trial and error); increasing the number resulted in no statistical difference at the 99% level.
- 10) The results described below were then printed.

Figure 16 is a schematic representation of the four curves generated by this procedure. One of the top curves is the actual velocity profile that an unbiased ultrasonic flow meter would measure (see Eq. (II.11)). The midstream value of this profile is $2 \cdot \Delta s \cdot \cos(\theta)$. This is the round trip distance that the scatterer on the vessel axis moves between echoes projected onto the sound beam axis (Figure 13). The

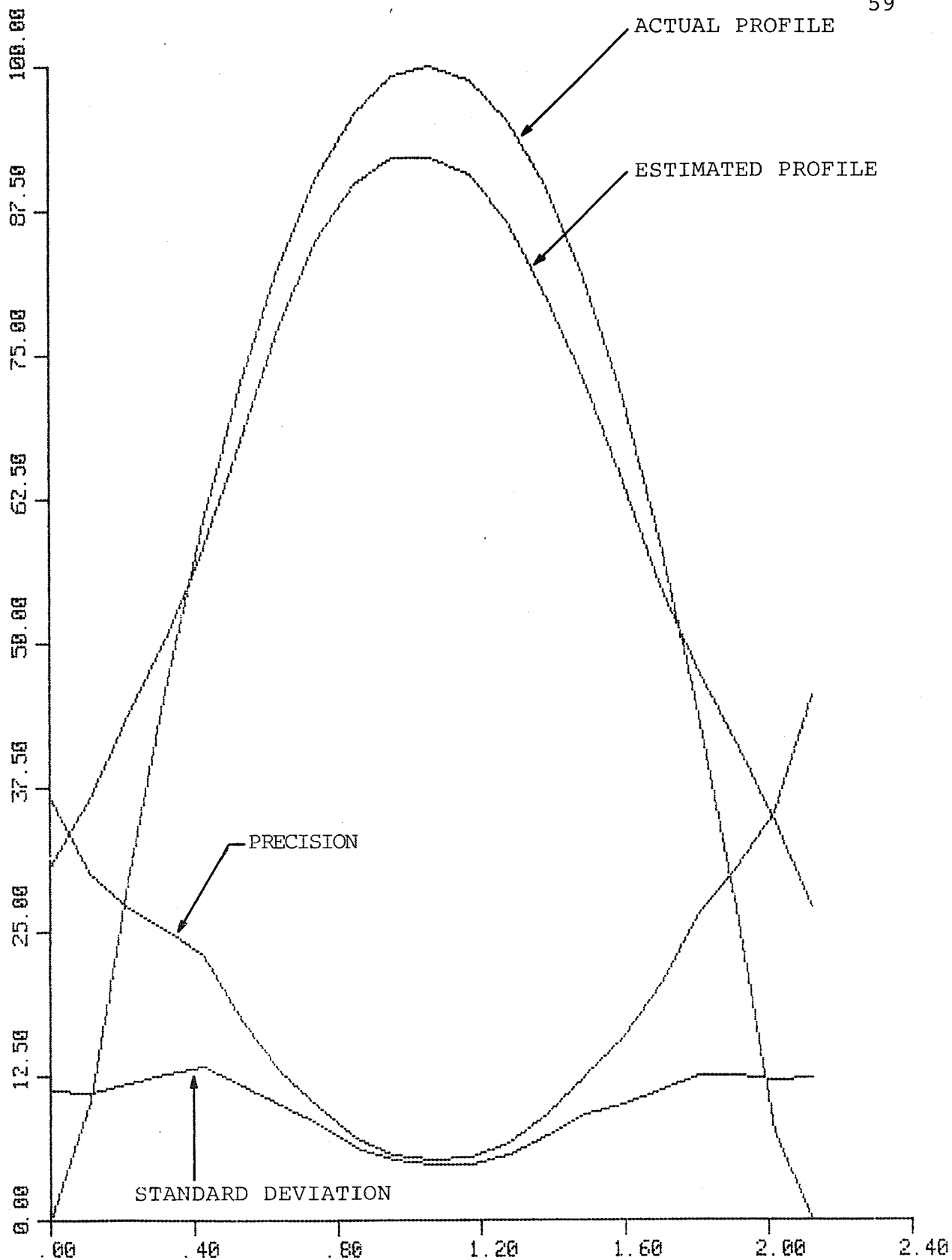


Figure 16. Graphic representation of the velocity profiles of the scatterers across the vessel for the computer simulation of the time domain velocity extraction technique. This is the model curve for Figures 17, 18, and 19.

other top curve is the estimated velocity profile. This is the TDM estimate of the actual profile. Both of the top curves are normalized (divided) by the midstream value of the actual flow. This places the maximum of the actual flow at 100% allowing for ease in comparing graphs with different parametric values. The third curve is the jitter of the estimate normalized by the above factor. The fourth curve is a measure of the precision of the TDM. The curve consists of the jitter (standard deviation of the estimate of the mean) divided by the estimate of the mean and then multiplied by 100:

$$\text{precision (\%)} = 100 \cdot \frac{\sqrt{E[(V - E[V])^2]}}{E[V]} \quad \text{Eq. (III.1)}$$

where $E[.]$ is the expectation operator and V is the estimate of velocity using the TDM. This curve is not normalized as were the above-mentioned three curves. When the value exceeds 100% it is truncated to 100%.

Figure 17 shows the simulated results of the time domain method on a system with the following parameters:

- 1) vessel diameter of 24 wavelengths,
- 2) parabolic velocity distribution,
- 3) axial position change of a half wavelength,
- 4) Airy beam pattern with a 3 dB beam width equal to 2 wavelengths,
- 5) system Q is 4,
- 6) correlation length is 8 wavelengths, and
- 7) a viewing angle varying from 45 degrees to 75 degrees in 10 degree increments.

Figures 18 and 19 use the same parameters as above except that the vessel sizes are 12 and 6 wavelengths, respectively.

The jitter from beam width modulation is present in Figures 17-19. However, along with this jitter is the jitter

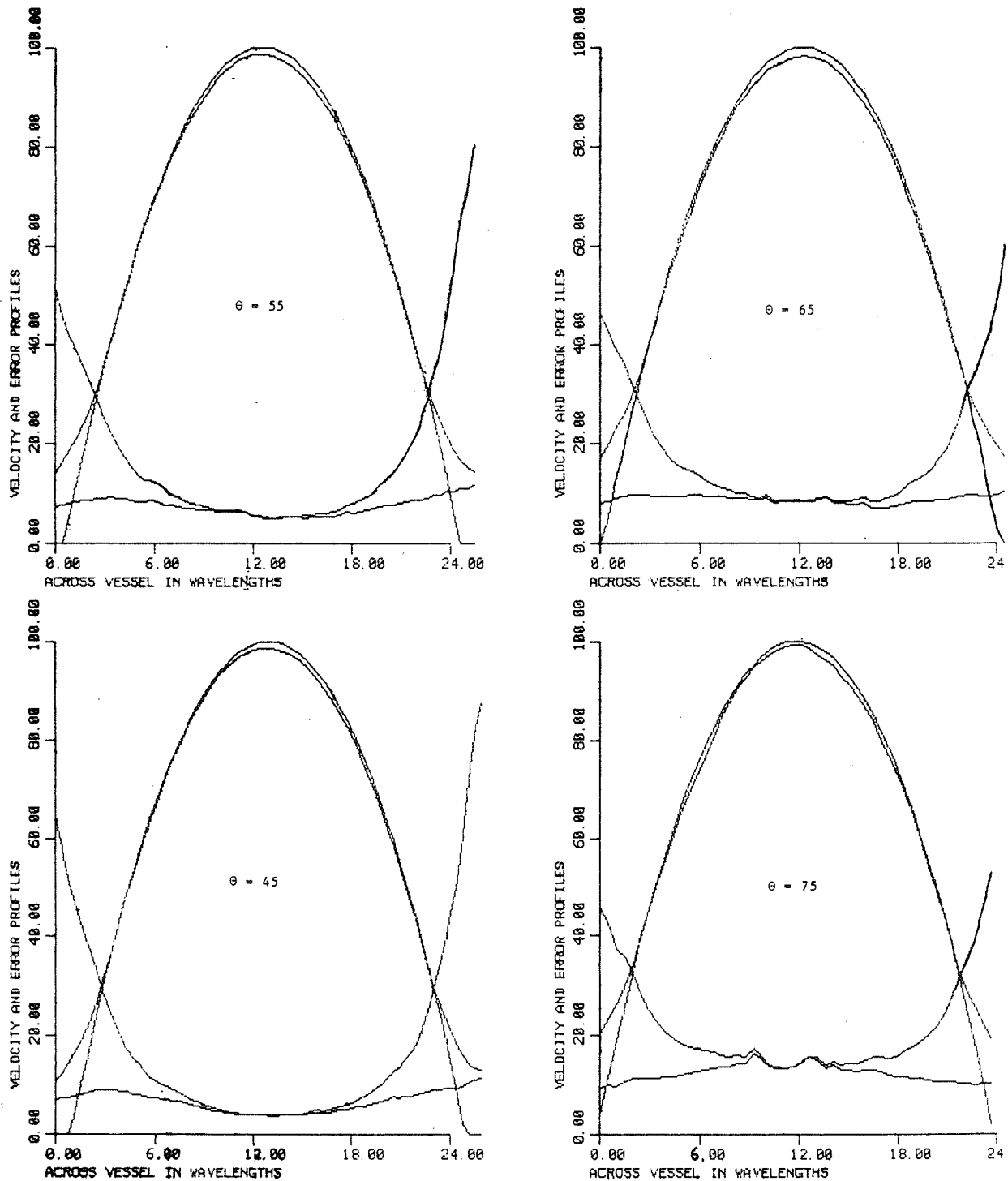


Figure 17. Results of the computer simulation of the time domain method using the following parameters in wavelengths: vessel diameter of 24, Δs of 0.5, transducer beam width of 2, and a correlation length of 8. The viewing angle varies from 45 to 75 degrees and the system Q is 4.

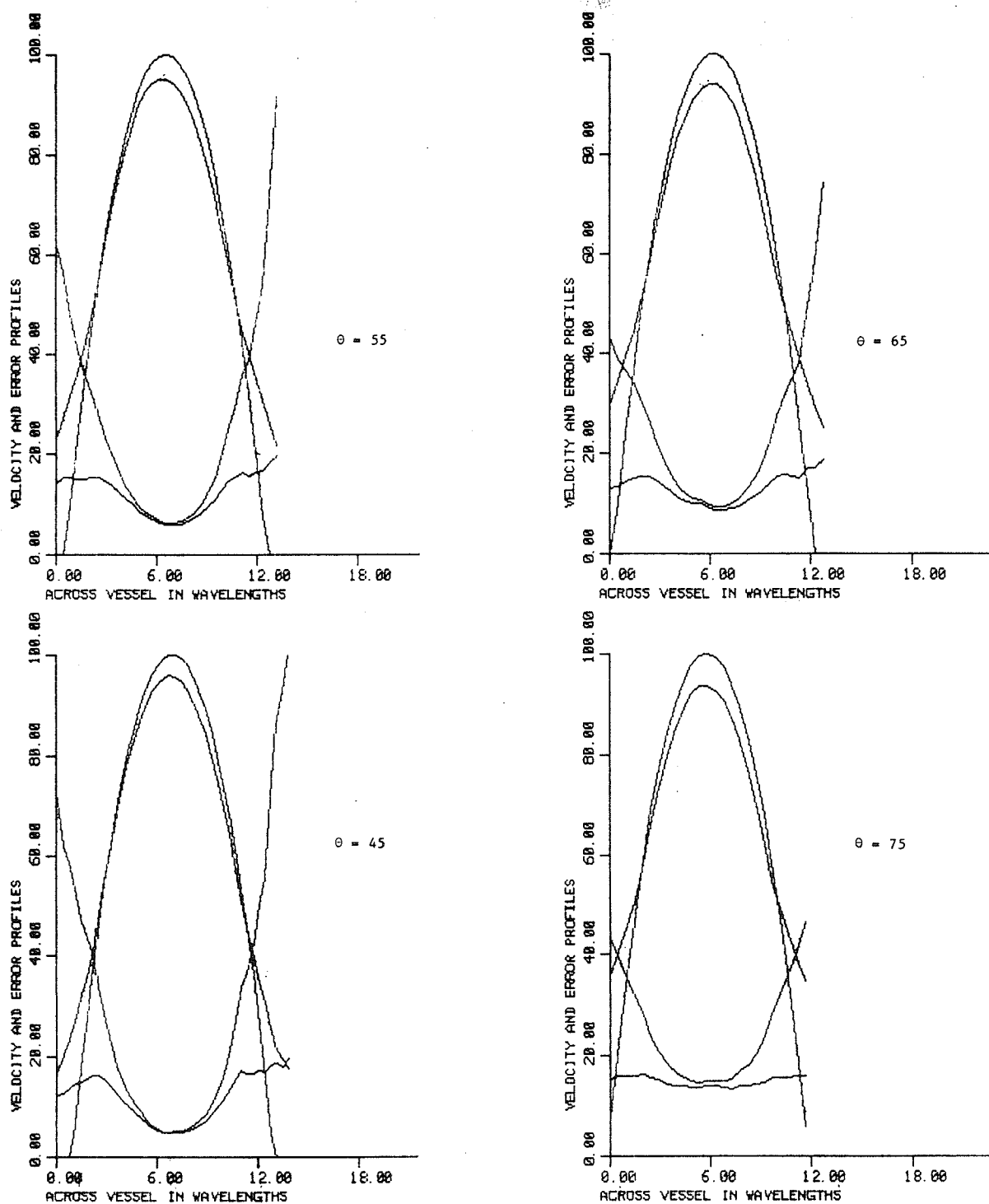


Figure 18. Results of the computer simulation of the time domain method using the following parameters in wavelengths: vessel diameter of 12, Δs of 0.5, transducer beam width of 2, and a correlation length of 8. The viewing angle varies from 45 to 75 degrees and the system Q is 4.

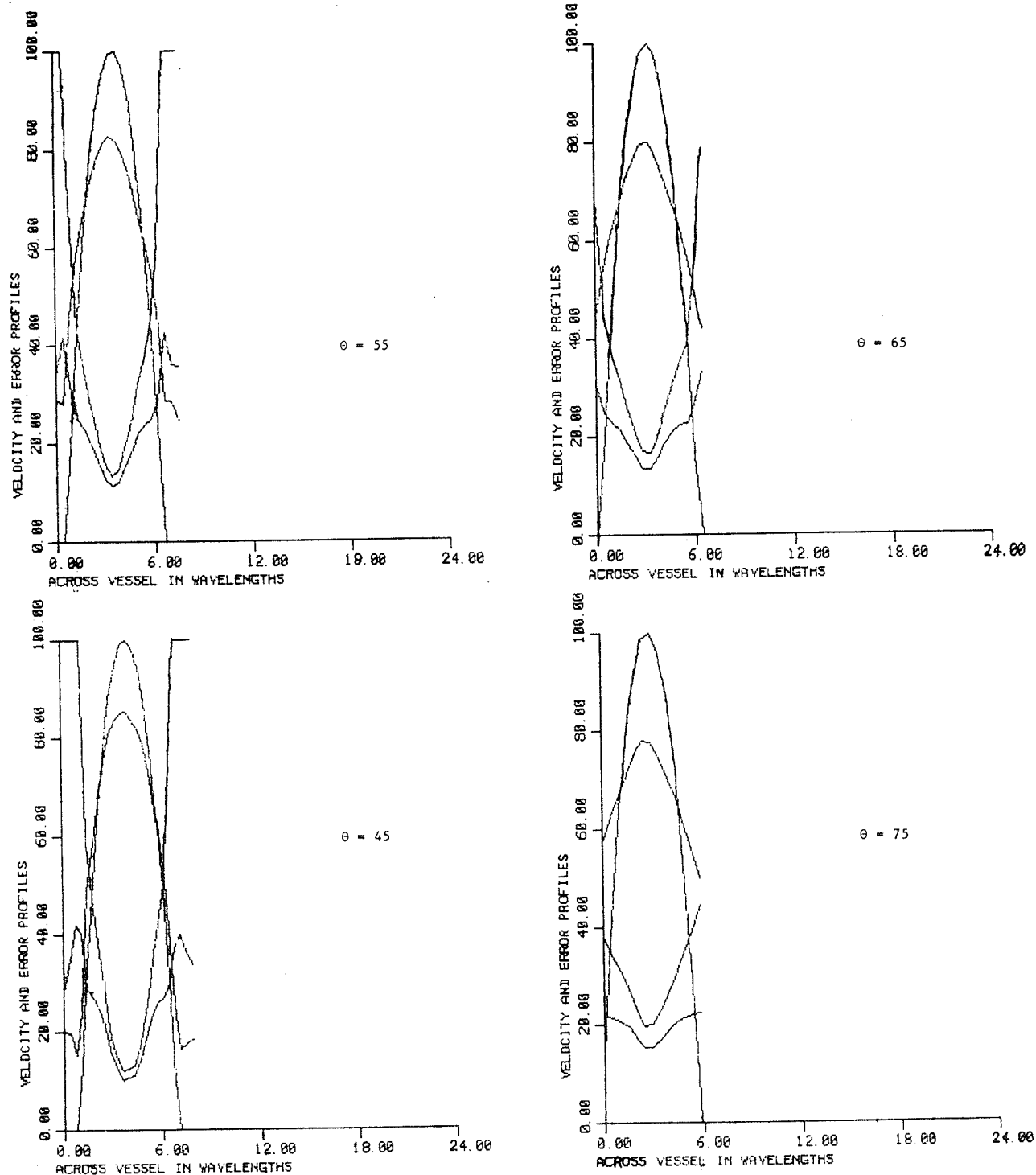


Figure 19. Results of the computer simulation of the time domain method using the following parameters in wavelengths: vessel diameter of 6, Δs of 0.5, transducer beam width of 2, and a correlation length of 8. The viewing angle varies from 45 to 75 degrees and the system Q is 4.

from velocity gradients across the range cell. The figures all have the same size range cell (only the vessel diameter was changed), hence, the velocity gradient across the range cell will be smallest in the largest vessel where the flow is nearly constant over a greater distance. To minimize the contribution to jitter from velocity gradients, the midstream jitter of the largest vessel at the smallest viewing angle (45 degrees) will be examined. A smaller viewing angle will result in a longer path through the vessel minimizing further the effect of velocity gradients. In Figure 17 midstream jitter is 3.7%.

Using the theory in (C) of Chapter II and Figure 12 the theoretical jitter will now be calculated. The perpendicular positional change (Δs_{\perp}) of a scatterer with respect to the beam axis is related to the axial positional change (Δs) of the scatterer by the sine of the viewing angle:

$$\Delta s_{\perp} = \Delta s \cdot \sin(\theta) \quad \text{Eq. (III.2)}$$

Hence, the perpendicular positional change is $0.5 \cdot \sin(45^{\circ})$ or 0.354 wavelength. The curves in Figure 12 are normalized by the sound beam width. The sound beam width used in Figure 17 is two wavelengths. Hence, the normalized perpendicular positional change is $0.354/2 = 0.177$. From Figure 12 this corresponds to a jitter of 2.6%. In order to compare this value of jitter with the normalized jitter in Figure 16, the 2.6% value must be divided by the normalizing factor of $2 \cdot 0.5 \cdot \cos(45^{\circ})$, yielding a normalized jitter of 3.7%. This value agrees with the value in Figure 16. Hence, the

midstream value of jitter for the 45 degree case in Figure 16 is largely a result of beam width modulation. The midstream values of jitter for the smaller vessels and larger angles are larger than the 3.7% baseline value for beam width modulation, indicating that the jitter introduced by velocity gradients is increasing.

The jitter from velocity gradients can be observed in Figures 17-19 at the edges of the vessel where the effects of beam width modulation are minimal. For example, the beam width modulation of Figure 17 is largest at midstream (since the scatterers are moving the fastest here) with a value of 3.7%. All other jitter above this baseline is a result of velocity gradients, and near the edges of the vessel the jitter from velocity gradients will account for much of the jitter below this baseline.

In Figures 18 and 19 the jitter is much farther above the 3.7% baseline set by beam width modulation. This follows because the vessels are more narrow but have the same axial flow velocity and range cell size as the 24 wavelength diameter vessel in Figure 17, hence, the velocity gradients must be greater.

A rough calculation can be made from the theory in (C) of Chapter II on the amount of jitter at the vessel wall for Figure 17 and viewing angle of 45 degrees. The measured axial shift of a scatterer is $2 \cdot \Delta s \cdot \cos(\theta)$ or $2 \cdot 0.5 \cdot \cos(45^\circ) = 0.7$. The range cell will have an acoustic length of approximately half the sum of the correlation length (8), the impulse response length (2), and the length

of the projection of the beam width along the vessel axis (2). Hence, taking the length to be approximately six wavelengths and substituting these values into Eq. (II.14) and letting $r=D/2$ (interested in the gradients near the vessel wall), the value of separation is about 0.35. This corresponds to a jitter of 7% (from Figure 10, $LEN=8$). Normalizing the 7% by the normalizing factor of 0.7 the resulting jitter in Figure 17 should be 10%. Looking at the figure, the jitter is seen to be maximal at the vessel edge with a value of 10%.

Table III.1 examines the interdependencies of four parameters in the estimation of the velocity profile. The four parameters are correlation length (4 and 8 wavelengths), 3 dB beam width of 2 and 4 wavelengths, vessel diameter (6, 12, and 24 wavelengths), and viewing angle (45, 55, 65, and 75 degrees). The fixed parameters are: the velocity profile is parabolic, the Q of the system is 4, the axial separation is 0.5 wavelength, and the lateral ultrasonic field pattern is an Airy distribution. These parameters are approximately the same as the experimental parameters and hence allow the results of the simulation to be compared to the theory. Table III.1 consists of pairs of numbers. Numbers without parentheses are the estimates of the actual flow at midstream divided by the actual flow at midstream multiplied by 100 (the bias). The numbers in parentheses are the precisions of the velocity estimation (see Eq. (III.1)).

Table III.1

Results of a computer simulation of the estimation of midstream flow (the number without parenthesis) and the precision in the velocity estimation (the number in parenthesis). The parameters varied are: the vessel diameter, the correlation length (LEN), the beam width of the transducer (BW), and the viewing angle (THETA).

			TUBE DIAMETER (in wavelengths)		
			24	12	6
BW=4	LEN=4	THETA=45:	98.0(2.9)	93.1(6.6)	79.9(24.9)
"	"	THETA=55:	97.9(4.2)	92.6(7.6)	78.4(24.6)
"	"	THETA=65:	98.3(5.5)	93.0(8.4)	77.8(25.7)
"	"	THETA=75:	98.3(10.1)	93.2(12.7)	77.6(22.0)
"	LEN=8	THETA=45:	97.6(2.2)	91.8(5.0)	76.8(23.9)
"	"	THETA=55:	97.6(2.9)	91.1(5.8)	73.9(22.2)
"	"	THETA=65:	97.6(4.1)	90.9(6.5)	70.8(21.3)
"	"	THETA=75:	97.5(7.2)	90.8(8.1)	69.6(20.0)
BW=2	LEN=4	THETA=45:	98.8(6.3)	97.0(7.0)	89.6(12.4)
"	"	THETA=55:	99.1(8.5)	96.4(8.6)	88.2(14.1)
"	"	THETA=65:	98.5(13.3)	96.1(14.1)	87.7(17.9)
"	"	THETA=75:	100.1(21.3)	95.3(22.9)	86.9(23.2)
"	LEN=8	THETA=45:	98.6(3.7)	95.7(4.9)	85.2(12.1)
"	"	THETA=55:	98.4(5.1)	94.8(6.3)	81.9(14.6)
"	"	THETA=65:	98.1(8.3)	93.7(9.1)	80.0(16.4)
"	"	THETA=75:	99.2(13.6)	93.4(14.9)	77.4(19.8)

Using the data from Table III.1 the effects of varying one parameter while keeping the other parameters fixed are examined.

1) Increasing the viewing angle results in a decrease in the precision of the velocity estimation. This trend is followed for all combinations of the other three parameters except the 6 wavelength vessel with a BW=4 wavelength and LEN=8 and LEN=4. The reason for this exception is the fact that the estimate of the midstream flow is decreasing faster than the variance of the estimate. Hence, the precision (the ratio of the two above quantities) will increase.

2) Increasing the correlation length results in more

precision. The theory in (D) of Chapter II and the results displayed in Figure 7 predict this result.

- 3) Reducing the tube diameter decreases the precision. The velocity gradients are higher in the narrower tubing than in the large tubing for identically sized range cells.
- 4) A larger beam width has a greater precision in the larger tubes where the velocity gradients are small across the range cell.
- 5) The smaller the correlation length the less bias there is in the velocity estimate. Bias is the deviation of the estimate from 100% flow. The shorter correlation length allows less local averaging of the velocity profile.
- 6) The smaller the tube diameter the greater the bias. Here the size of the range cell remained constant, but due to the narrowing of the velocity profile, the range cell must now contain a larger number of scatterers of differing velocities, hence, biasing the results (downward).
- 7) Bias gets worse for increasing viewing angle, especially for the smaller tubes. The larger angles reduce the length of the echo (by the cosine of the viewing angle), hence, increasing the velocity gradients in the range cell (the range cell dimensions are independent of angle but dependent on beam width, correlation length, and impulse response).
- 8) Large beam widths have a greater bias. The beam width will smooth out velocity information, hence, detail in the range cell will be lost.

The effect on the estimation of velocity of different

axial position changes of the scatterers is given in Table III.2 for a typical experimental setup used in this thesis.

Table III.2

Amount of bias and precision in the computer simulation for differing shifts. The parameters used in the simulation were: a 24 wavelength diameter vessel, a transducer with a 2 wavelength beam width, a viewing angle of 45 degrees, and the correlation lengths (LEN) listed.

	LEN=4	LEN=8
SHIFT=0.25	98.8(6.1)	98.6(3.5)
" 0.50	98.8(6.3)	98.6(3.5)
" 0.75	98.8(6.4)	98.6(3.5)
" 1.00	98.8(6.9)	98.6(4.1)

Note that the bias is independent of the amount of axial position change (SHIFT); however, the precision is slightly smaller at the larger values of axial position change.

Some conclusions can be drawn from the results of this chapter. The bias is directly related to the size of the range cell (a smaller range cell will average over a smaller portion of the velocity profile). Several parameters control the precision;

- 1) The beam width of the range cell. A narrower beam width will result in a smaller amount of beam width modulation under the same circumstances for a larger beam width.
- 2) The correlation length of the window. A shorter correlation length will have a smaller precision in the estimate of the actual shift than a longer length.
- 3) Too large a range cell will result in the establishment of velocity gradients across the range cell resulting in a smaller precision.

Parameters 1) and 2) must be traded off against 3).

IV. EXPERIMENTAL VERIFICATION

In this chapter the estimation of speed of the scatterers and the standard deviation of the estimate are examined under different flow conditions to test the validity of the theory that was developed in Chapter II and which was examined with computer simulation techniques in Chapter III.

A. Experimental Setup

Figure 20 shows a block diagram of the experimental arrangement used for testing the time domain method. The Perkin-Elmer 7/32 computer is a 32-bit machine with two 5 megabyte discs and 384 kilobytes of memory. Typical execution time for floating point multiplication instructions is 10.25 microseconds.

The computer controls an analog-to-digital converter (A/D) interface which was designed and fabricated in the Bioacoustics Research Laboratory of the University of Illinois. Detailed circuit diagrams are included in the Appendix. The analog-to-digital converter consists of two TRW 8-bit flash A/D converters (model number TDC1007J) operating in parallel at 25 MHz for a combined speed of 50 MHz. The A/D unit contains a 8192 byte bipolar memory and the circuitry necessary for generating the programmed pulse repetition frequency for the trigger to the pulse generator, for delaying a predetermined amount of time before sampling, and for digitizing the programmed number of samples per echo. All digitization is performed synchronously. The A/D unit will be discussed in more detail in Section B of this Chapter.

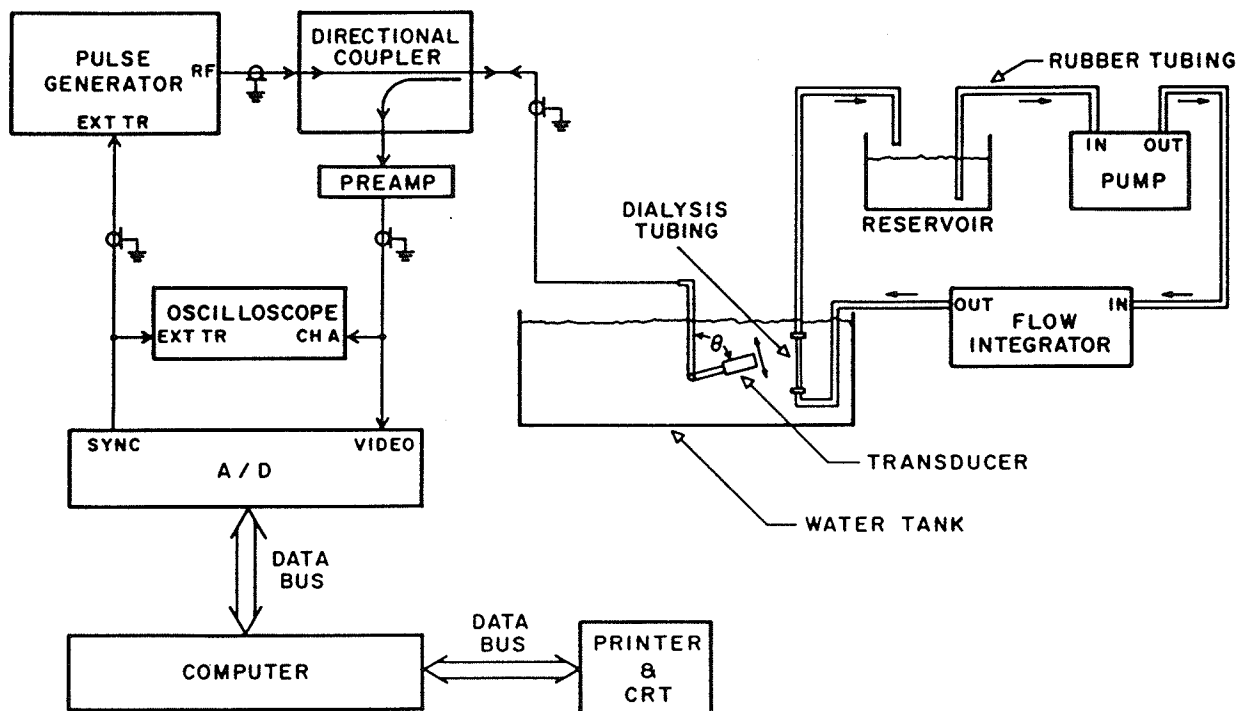


Figure 20. Experimental setup used to verify the time domain method.

The pulse generator is a Panametrics 5050PR. The two Panametrics transducers that are used (model number V309 and V307) operate at a center frequency of 5 MHz, have diameters of 12.7 mm (0.5 inch) and 25.4 mm (1 inch), are focused at 50.8 mm (2 inches), and are heavily damped. Each transducer has its own matched directional coupler that prevents the received echo from traveling back to the pulse generator. The output impedance of the transducer is transformed to an optimal value for the preamp by a RF transformer in the coupler. The preamp is a low noise amplifier (1.8 dB noise figure) used to amplify the echoes from the scattering medium. The amplifier provides enough power gain (30 dB to 90 dB) to drive the A/D unit. The Q of the whole system (preamp, transmitting and receiving with the same transducer, and the frequency dependent properties of the water) was measured to be approximately 4. Details of the measurement of the Q are in Section C of this Chapter.

The commercial pump (March Manufacturer Incorporated, model number 212) has the capacity to pump 50 - 1000 ml/min. The flow integrator consisted of two integrators operating in series whose net effect was to smooth the pulsatile output of the pump. The first integrator consisted of a 50 ml plastic hemisphere (2.88 cm radius) with the input and output ports on opposite sides. The second integrator is a 1000 ml Erlenmeyer flask with a two hole stopper and the necessary glass tubes and rubber connecting tubing needed to connect the two integrators together.

Buttermilk was used instead of blood as the scattering

medium because of convenience. The signal properties of the echoes returning from buttermilk are shown to be BPWGN in Section C (the same as the signal model for blood discussed in A of Chapter II). The scattering strength of buttermilk may be different from that of blood, but as long as the returning echo can be amplified to the level needed for the A/D's, the TDM makes no distinction in the original echo strength. The preamp has sufficient gain to ensure that the signals to the A/D's are at the needed level, and for testing the TDM, buttermilk is a suitable replacement for blood.

Two types of tubing were used in the experiment for transmitting and receiving ultrasound through the buttermilk: dialysis tubing and heat shrinkable tubing. However, for convenience, dialysis tubing will refer to both types. The dialysis tube was positioned vertically. Preliminary experiments with the time domain method suggest that if the tube were positioned other than vertically, the flow distribution across the vessel would not be symmetric about the vessel axis. This flow phenomenon was not investigated further and the tube was kept vertical. The length of the tube was approximately 10 cm.

The experimental design was to generate laminar, non-pulsatile flow through the dialysis tube. Theoretically, an infinite length of tubing is needed to set up parabolic flow, but fully developed laminar flow usually refers to axial flow that is within 1% of the value for an infinite tube [23]. Theoretically, the distance from the inlet of the tube necessary to develop fully laminar flow when the flow is

uniform at the inlet is given by [23]

$$L = 0.073 \frac{\rho Q}{\mu} \quad \text{Eq. (IV.1)}$$

where L is the length of the tube necessary to fully develop laminar flow, Q is the volume flow through the tube, ρ is the density and μ the viscosity of the fluid in the tube (all units in the expression must be mks). A conservative estimate of the viscosity of buttermilk is 1 cP; (for whole milk at 20°C the viscosity is 2.12 cP and for skim milk the viscosity is 1.37 cP at 25°C [24]). The viscosity of water at 20°C is approximately 1 cP. The density of buttermilk was measured by the author to be approximately 1000 kg/m³. In the experimental system the volume flow, Q, was restricted to values below 4 ml/s. This corresponds to an L of about 3 cm. Hence, the 5 cm distance between the tube inlet and where the ultrasonic beam intercepted the tube satisfies the above conditions for fully developed laminar flow.

The transducer was angulated by a precision platform. The resolution of the angle θ was 0.5 degree. The absolute angle between the transducer and the dialysis tube was not known accurately and was the primary source of experimental error (discussed below).

A typical experiment day would proceed in the following way: Buttermilk was purchased at a local convenience store, sometimes two days before the experiment and at other times during an experiment. When the buttermilk was not needed immediately, it was refrigerated. The water tank was then filled with cool tap water (temperature of 20°C). Then the

buttermilk was pumped through the tubing and allowed to warm up to the temperature of the water. If the buttermilk was cooled by ice to 10°C , the scattering properties of the buttermilk were found to be weaker. A typical experimental run time was six hours; after six hours the buttermilk lost its scattering ability and had to be replaced. During the six hours, different viewing angles, midstream flow velocities, orientations of the transducer to vessel, and system parameters are varied (see above) to study the TDM.

The sound beam was positioned in the following manner: The sound beam was moved laterally (by moving the transducer laterally) across the tubing, stopping at the position where the echo was widest and had the greatest amplitude. This position was taken to be the center of the tubing since at this position the echo would ideally be widest and have greatest amplitude. Then the greatest estimated speed along the echo was taken to be the midstream speed of the tube since for laminar flow the speed of the flow is greatest at the axis of the tube.

The parameters that were varied and are discussed in detail are: the vessel diameter, the ultrasonic beam width, the correlation length, the viewing angle, and the distance the scatterers move between echoes.

1) Focal region lateral beam width: Two transducers were used in the experiment. They will be called XTAL1 and XTAL2. Both transducers were spherically focused at 50.6 mm (2 inches) and had a center frequency of 5 MHz. The field plots of XTAL1 and XTAL2 are contained in Figures 21

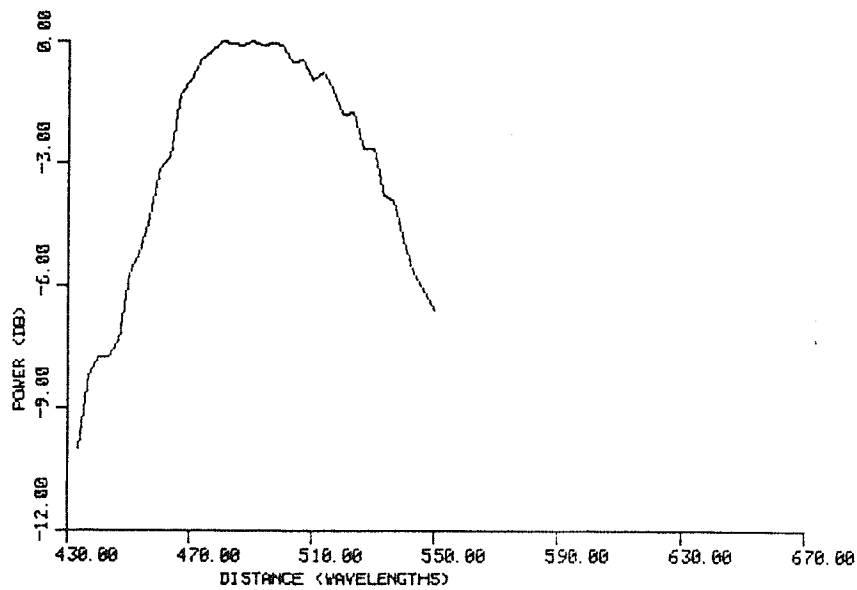
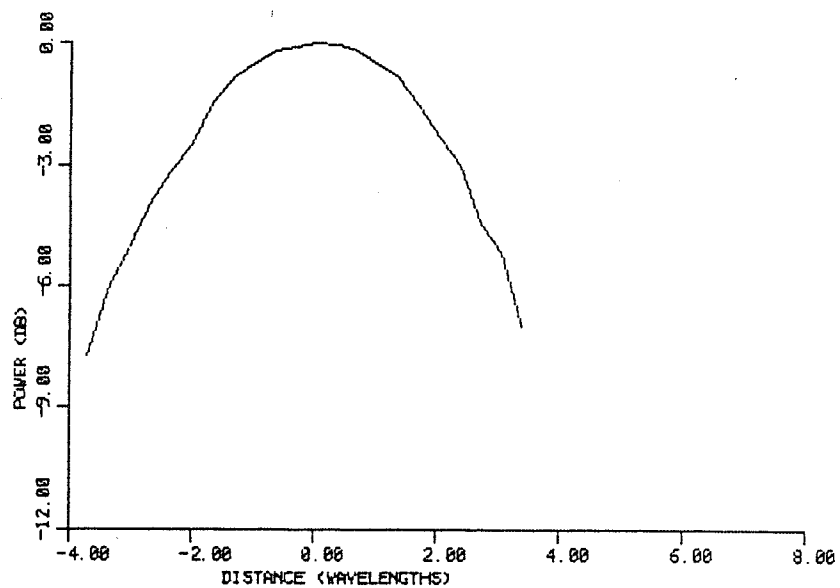


Figure 21. The top and bottom curves are the lateral and axial beam intensity plots, respectively, of XTAL1 at the focal point.

and 22, respectively. XTAL1 had a 12.7 mm (0.5 inch) aperture diameter, a 3 dB lateral width of 4.6 wavelengths of center frequency (1.4 mm), and an axial beam width of 109 wavelengths (33 mm). XTAL2 had a 25.4 mm (1 inch) diameter, a 3 dB beam width of 2.3 wavelengths (0.7 mm), and an axial beam width of 28 wavelengths (8.4 mm). These transducers were selected because they were commercially available and are representative of the clinical transducers currently being used.

- 2) The flow rate: The flow rate was varied by adjusting the pump speed. The volume flow from the pump was determined by the duration of time (measured with a stop watch) the flow took to fill a known volume (graduated cylinder). The accuracy of the volume flow measurement was $\pm 1\%$. The average flow rate is determined by dividing the volume flow rate by the cross-sectional area of the dialysis tube. The midstream flow rate is twice the average flow rate for fully developed laminar flow [21].
- 3) The viewing angle: Four viewing angles of 45, 55, 65, and 75 degrees were used. The angle was changed by rotating the transducer through an arc on the precision platform. The error in the angle of the arc was ± 0.5 degrees.
- 4) Correlation length of the window: Two lengths were chosen: 41 points (4 wavelengths at 5 MHz) and 81 points (8 wavelengths at 5 MHz). These values are rather arbitrary and correspond to axial resolutions of approximately 0.6 mm and 1.2 mm, respectively. The 4 wavelength correlation length is not so small as to cause

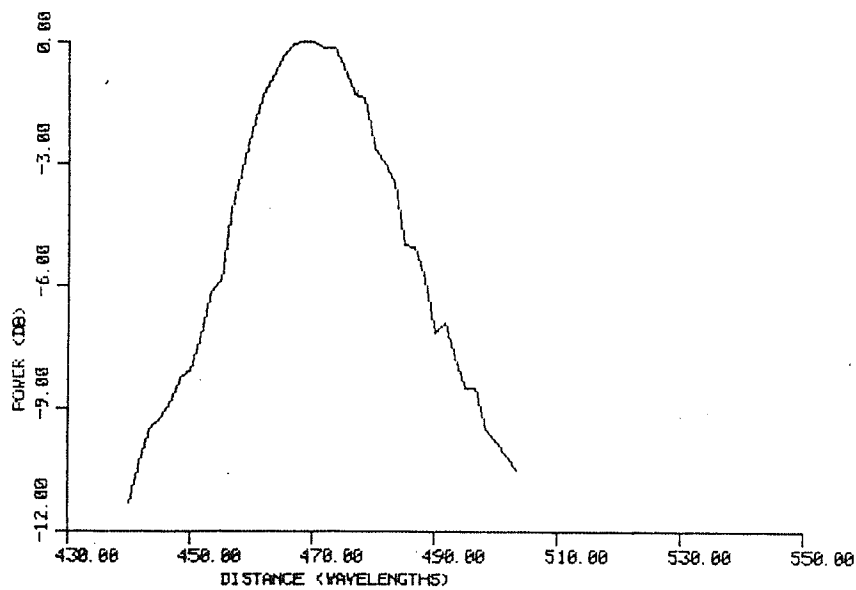
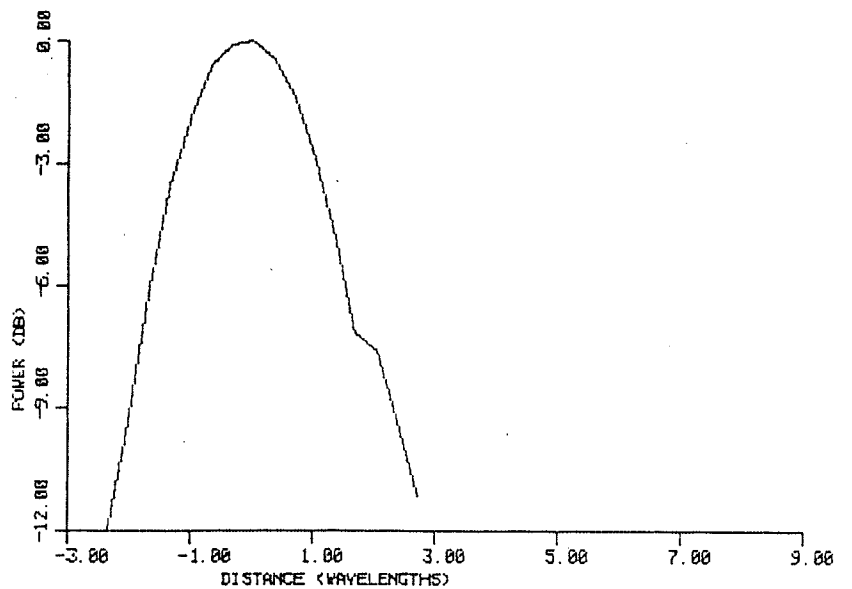


Figure 22. The top and bottom curves are the lateral and axial beam intensity plots, respectively, of XTAL2 at the focal point.

excessive errors from windowing, and the 8 wavelength value not so large as to cause excessive velocity gradients across the cell.

- 5) Dialysis tube diameter: Three sizes of dialysis tubing were used. Their inside diameters were 6.96 mm for the dialysis tubing (0.05 mm wall thickness) and 3.84 mm and 2.24 mm for the heat shrinkable tubing (0.46 mm wall thickness). This corresponds to inside diameters in wavelengths at 5 MHz of 23.2, 12.8, and 7.5. The error in the measurement of the inside diameters of the tubes was ± 0.05 mm. No degradation of the echoes was noticed by the walls of the tubes. But the TDM can take into account wall echoes. For the 75 degree viewing angle, the wall was present in the echo. This stationary wall echo can be subtracted from the echoes before processing. The tubes were selected because they were commercially available and comparable in size to the vessels examined by pulsed Doppler techniques in human subjects.

The parameters that were kept constant include:

- 1) Transmitted wavelength: The frequency was restricted to 5 MHz. However, even though the center frequency was not varied, the different tube diameters provide the capacity to examine the time domain approach as a function of tube diameter in wavelengths. That is, measuring the 6.96 mm tube at 2.5 MHz is equivalent to measuring the 3.84 mm tube with 5 MHz since they are both approximately 12 wavelengths across at their respective frequencies.
- 2) System Q: The system Q was kept as small as possible

(approximately 4, see Section C) to increase the ability to discern the range of the scatterers. The system Q was measured to be approximately 4.

B. Description of A/D Unit

In this section the two interleaved A/Ds and the associated timing circuits will be discussed (the A/D box of Figure 20). Figure 23 is the block diagram of the A/D box in Figure 20 and will be useful as a guide for the following discussion.

The pulse repetition rate (PRF) generator (PRF COUNTER in Figure 23) consisted of a divide by 5 prescaler followed by a 24-bit programmable counter. The prescaler was an artifact of an earlier design and has remained with the PRF generator even though the prescaler is not necessary. The pulse repetition rate code that is to be loaded into the 24-bit programmable counters at the end of the PRF cycle is held in 24 bit latches. The latches are loaded under program control from the computer before data acquisition begins (before the echoes are digitized and stored). The PRF generator is free running. At the end of a PRF cycle the PRF counter reloads itself and begins counting up to the end of the next PRF cycle. At the time that the PRF counter reloads itself the sync pulse to the pulse generator is sent.

At the end of a PRF cycle the PRF generator sends a logic high to the flip-flop whose Q output feeds the enable to the range counter. The next clock sets the flip-flop and enables the range counter. At the end of the range gate the flip-flop is cleared and waits for the next PRF cycle to

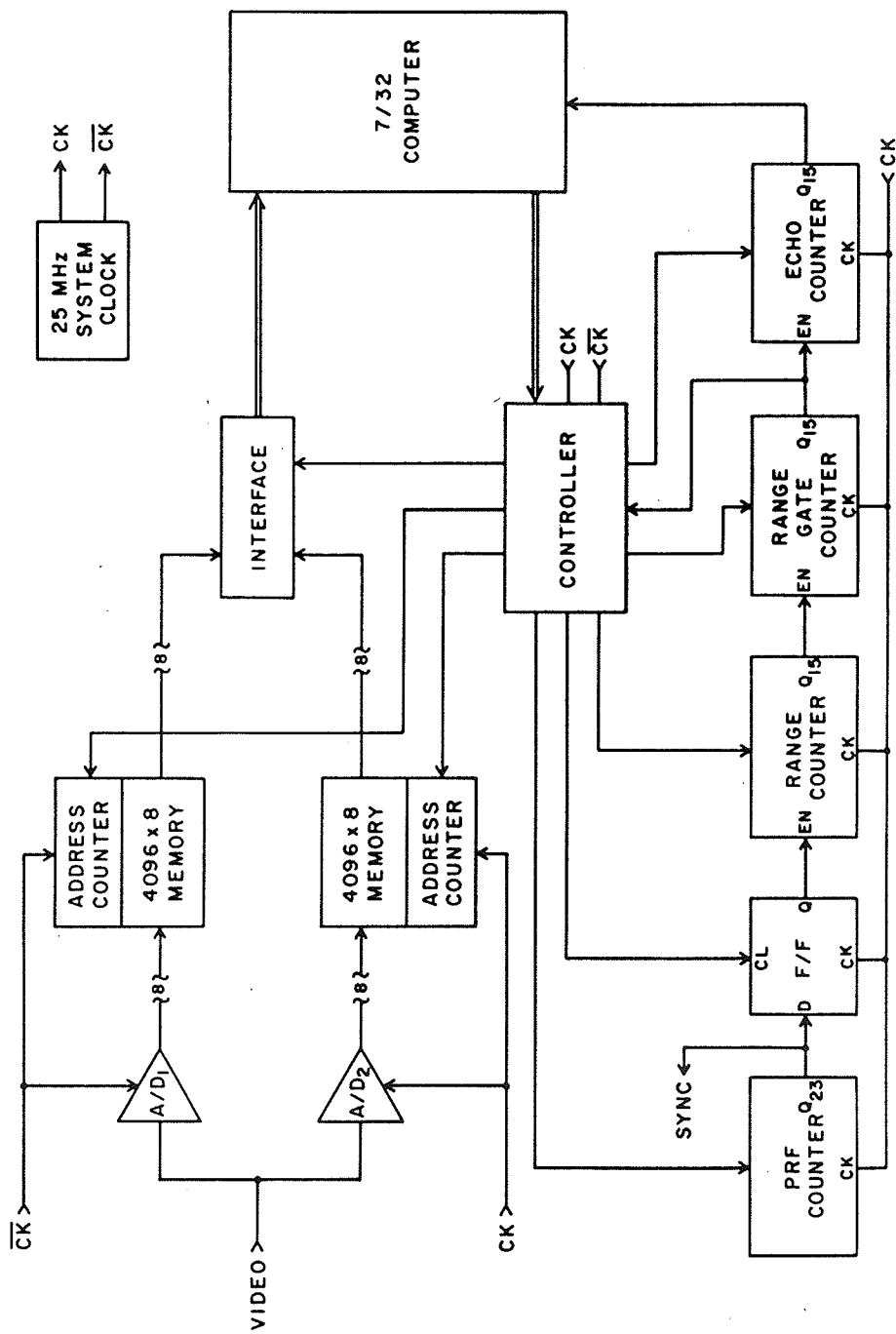


Figure 23. Block diagram of A/D unit.

become set. The flip-flop is first cleared at the beginning of data acquisition by a programmed clear (the flip-flop might have already been cleared by the echo counter, see below), and at the end of data acquisition, the flip-flop is held in a clear state until the next sequence of data acquisition.

The range counter (16 bit) is enabled at the end of the PRF cycle after the flip-flop sets. After the range counter has counted the programmed amount, Q15 goes high enabling the range gate counter. The range gate counter is programmed for the range over which the echoes are to be digitized. The programmed amount is held in a 16-bit latch loaded under program control before data acquisition begins. At the end of the range gate the range counter is reloaded with the data held in the latch and awaits the next enable from the flip-flop (which is also cleared at the end of the range gate).

The range gate counter (16 bit) begins counting when Q15 of the range counter goes high. The range gate counter is loaded with the width of the range gate needed to capture the echo. The information for loading the counter is held in a 16-bit latch that is programmed before data acquisition. At the end of the count the range gate counter reloads itself, loads the range counter (resetting Q15 of the range counter), and clears the flip-flop.

At the end of the range gate the echo counter (16 bit) is incremented. If the counter overflows, the computer is flagged that the data acquisition sequence has been completed

and the flip-flop is held in a clear state until the flip-flop is released under program control at the beginning of the next data acquisition sequence. If the counter does not overflow, the data acquisition sequence will continue. The data for loading the echo counter are held in a 16-bit latch and are programmed before data acquisition. If the same number of echoes from one data acquisition sequence to the next is required, then the echo latch does not need to be reloaded (this is true for all of the counters). The clear on the flip-flop is released at the beginning of the data acquisition sequence by loading the echo counter, hence removing the overflow condition.

The system clock (25 MHz) is generated by an ECL oscillator. The use of ECL allows the easy generation of a two phase clock so that the A/D's can operate off alternate half cycles. The duty cycle and relative delay from each other can be adjusted by single shots contained in the oscillator block. The A/D's need a particular duty cycle for optimal operation. The differences in the aperture delays (the point at which the video is taken for digitization after the leading edge of the clock) can be compensated by adjusting the relative delay of the clock between the two A/D's. The oscillator block has the provision of generating in phase clocks for the A/D for the case in which two different signals need to be converted simultaneously.

The A/D's are both TRW model TDC1007PCB. The A/D's are constantly converting the signal and outputting the 8-bit conversion to the memory. The A/D's are flash converters,

that is, with one clock the signal is converted fully. The A/D's are guaranteed to operate at 25 MHz and typically operate at 30 MHz.

The 8-bit output of the A/D's feed their own bipolar type memory (INTEL model 2115A 1Kx1 high speed memory). A high speed memory is required because the computer cannot store data at 25 megabytes per second. The size of each A/D memory is 4096 bytes (8 bits are one byte) organized as 4096x8. The address lines are generated by a 12-bit counter which shares the same clock as the A/D feeding the memory. The counter is enabled during the range gate or during the computer read cycle. At the beginning of the data acquisition sequence when the echo counter is loaded, the write line to the memory is enabled. When the echo counter overflows, the address counters are cleared and the write line disabled.

The tristate interface buffers the data from the bipolar memory to the computer I/O line. The interface is disabled when the A/D unit is not addressed by the computer insuring that there is no interference with other devices connected to the same I/O line.

C. Measured Statistics of the Echo Waveform

In this section the signal model of an echo from buttermilk will be shown to be BPWGN and, hence, a suitable replacement for blood in evaluating the TDM. The probability distribution function (pdf) and the spectrum will be examined for a Gaussian distribution and a bandpass spectrum, respectively.

The pdf was measured by sampling at one A/D sample point the voltage of the echo at midstream range. A large number (65536) of points was taken to determine the frequency of occurrence of the A/D levels, which is by definition the pdf. The midstream velocity of the buttermilk was a nominal 2 cm/sec and was contained by the 6.98 mm diameter tube. The PRF used was 151 Hz which is a rather slow experimental PRF, but this allowed for some degree of independence from sample to sample. Independence is not necessary to find the pdf, but independence allows the pdf to converge more quickly. The mean and variance of the voltage were also determined and a Gaussian curve generated with these parameters. In Figure 24 both curves are plotted.

A chi square test was performed on the experimental pdf with the experimentally measured pdf to see if the two curves were in agreement. The comparison was made on the data within two standard deviations of the mean of the experimental pdf curve to prevent the discrete nature of the number of samples in the tails of the curves from causing arithmetic faults in the computer program. The curves were found to compare favorably at the 95% level. Hence, the pdf appears to be Gaussian.

The spectrum of the echo was determined by finding the autocorrelation function of the echo and then taking the Fourier transform of the function with an FFT yielding the power spectrum. The autocorrelation function was measured by averaging it many times. The results of the FFT are given in Figure 25. There are approximately 10 A/D samples per cycle

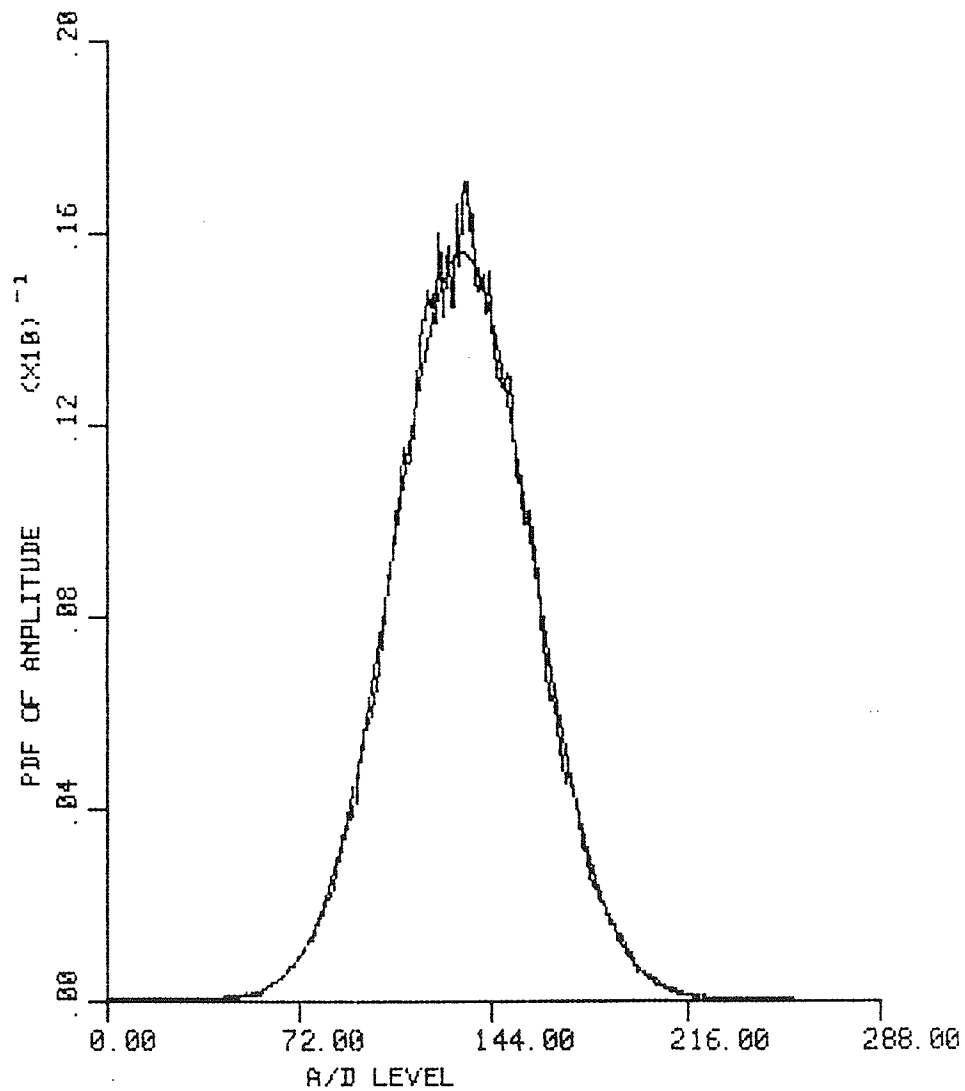


Figure 24. A graph of the measured probability distribution function of the received scattered ultrasound.

of the center frequency of the transducer (5 MHz) and the FFT is 128 samples long. Hence the spectrum should peak at $128/10$ or around 13. Included in Figure 25 is the autocorrelation function. Note that the function has a period of 10 samples, which is the center frequency of the transducer.

The Q of the system was determined by dividing the center frequency (5 MHz) of the transducer by the 3 dB bandwidth of the spectrum in Figure 25. Both transducers were found to have approximately the same Q of 4.

D. Velocity Profile Results

The time domain method was used to determine the velocity profile across a vessel. In each of Figures 26, 27, and 28, there are four graphs. Each represents the different viewing angles of 45, 55, 65, and 75 degrees. In each of the 12 graphs there are four curves. They are essentially the same as those of Figure 16 and are discussed in detail below. The three different tube diameters of 23, 13, and 7.5 wavelengths are represented in Figures 26, 27, and 28, respectively. The correlation length is 8 wavelengths and the beam width 4.6 wavelengths for Figures 26 and 27 and, for Figure 28, these variables are 4 and 2.3 wavelengths, respectively. The curves are normalized by the estimate of the midstream velocity value and are hence read from the relative velocity profile axis (the vertical axis in the figures). The curves in Figures 26, 27, and 28 are a result of averaging 256 measured profiles over a two-minute period. Using this number of profiles allowed for the accuracy of the

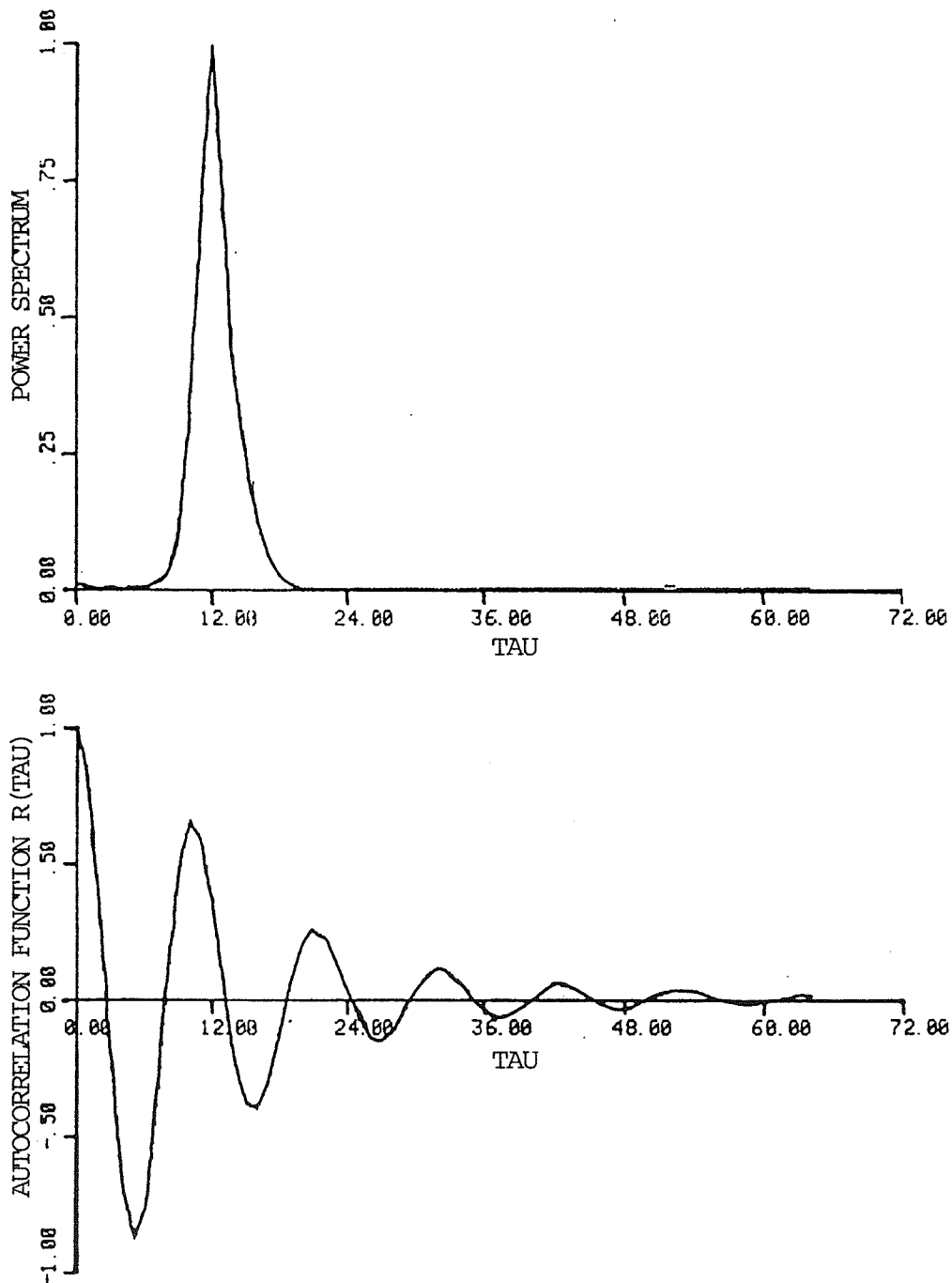


Figure 25. The autocorrelation function (bottom curve) and the power spectrum (top curve) of the echo.

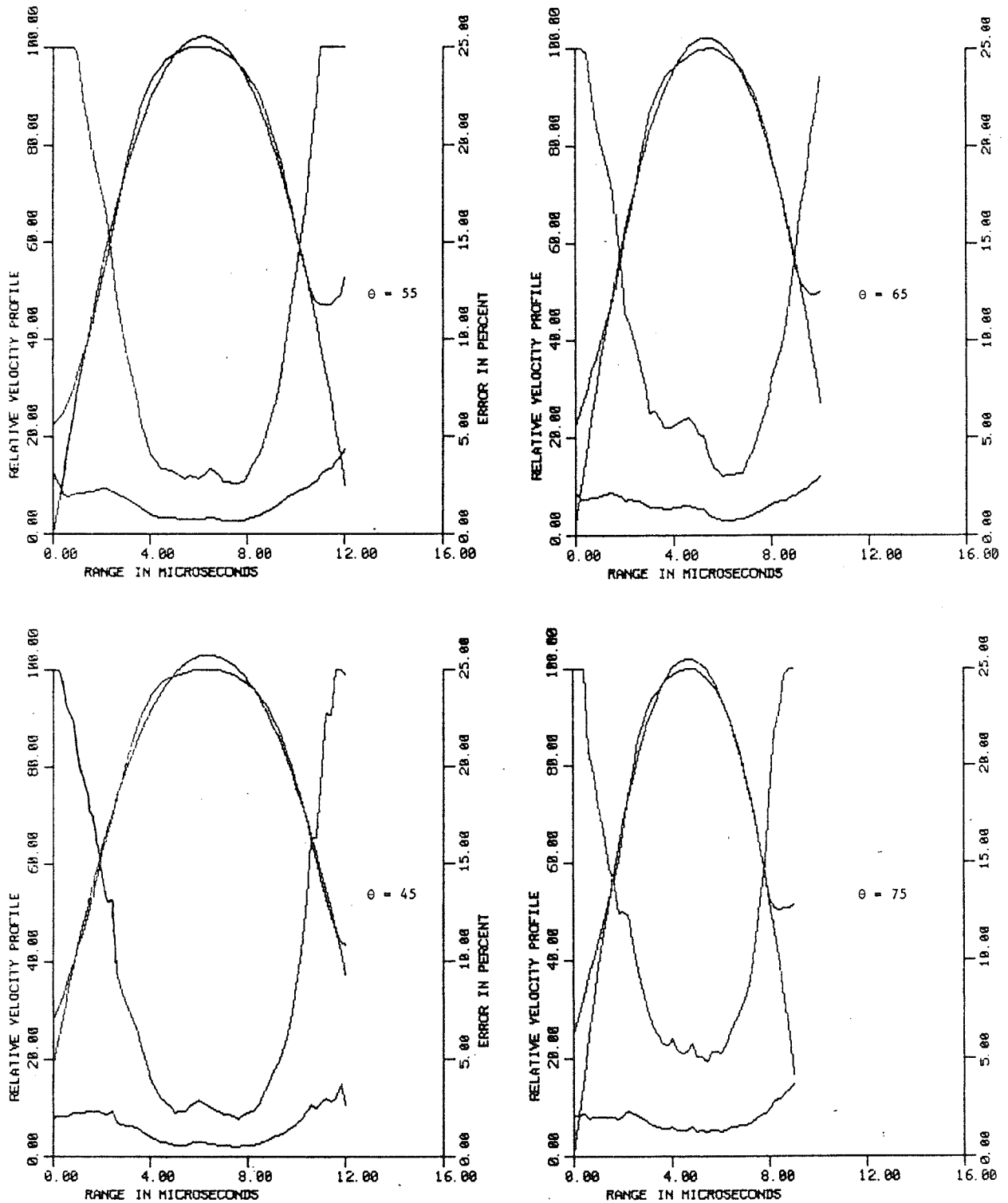


Figure 26. Experimentally measured velocity profile from a tube with a diameter of 23 wavelengths (6.96 mm), a correlation length of 8 wavelengths, and a transducer beam width of 2.6 wavelengths. Curves follow the model curves of Figure 16.

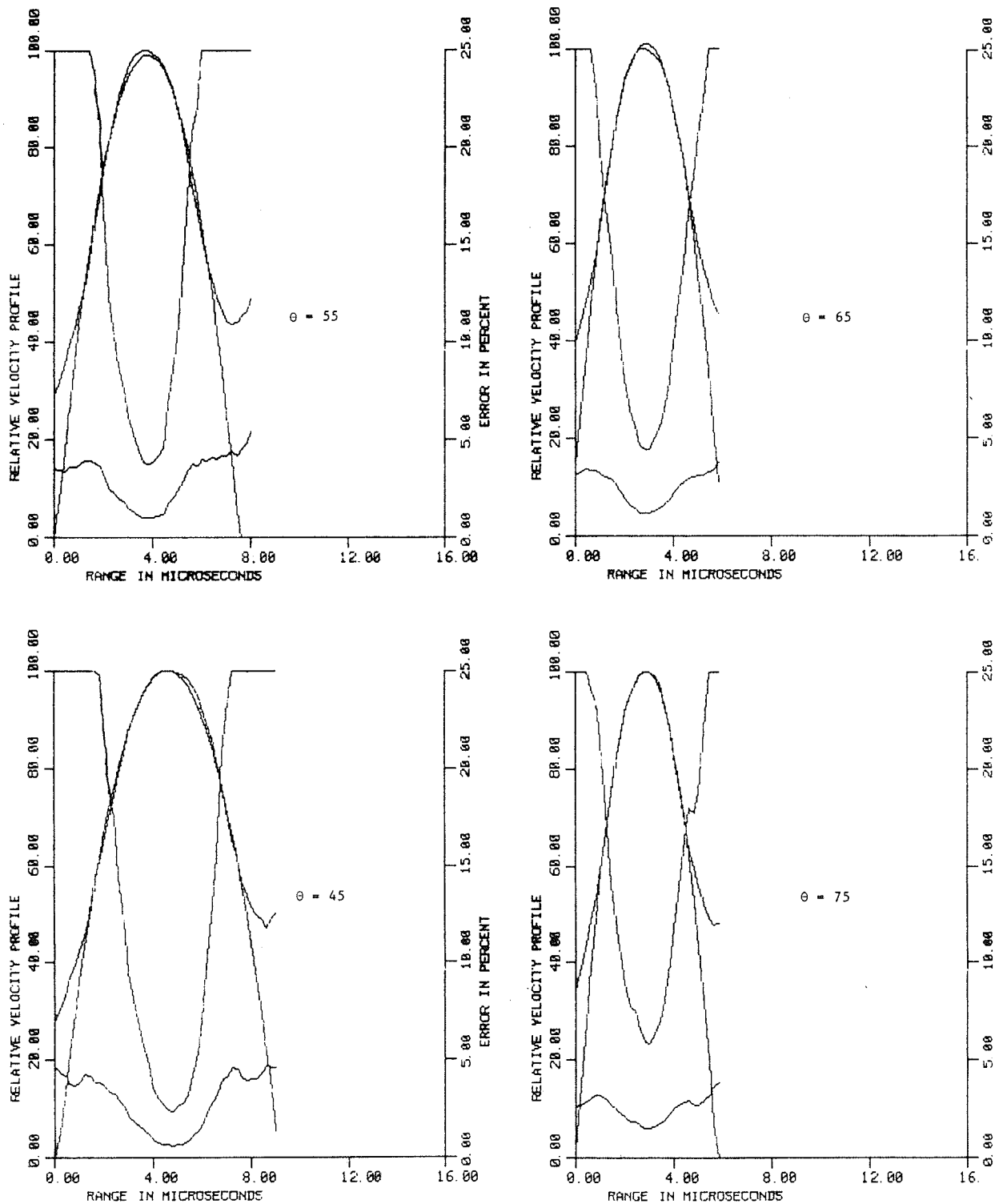


Figure 27. Experimentally measured velocity profile from a tube with a diameter of 13 wavelengths (3.84 mm), a correlations length of 8 wavelengths, and a transducer beam width of 4.6 wavelengths. Curves follow the model curves of Figure 16.

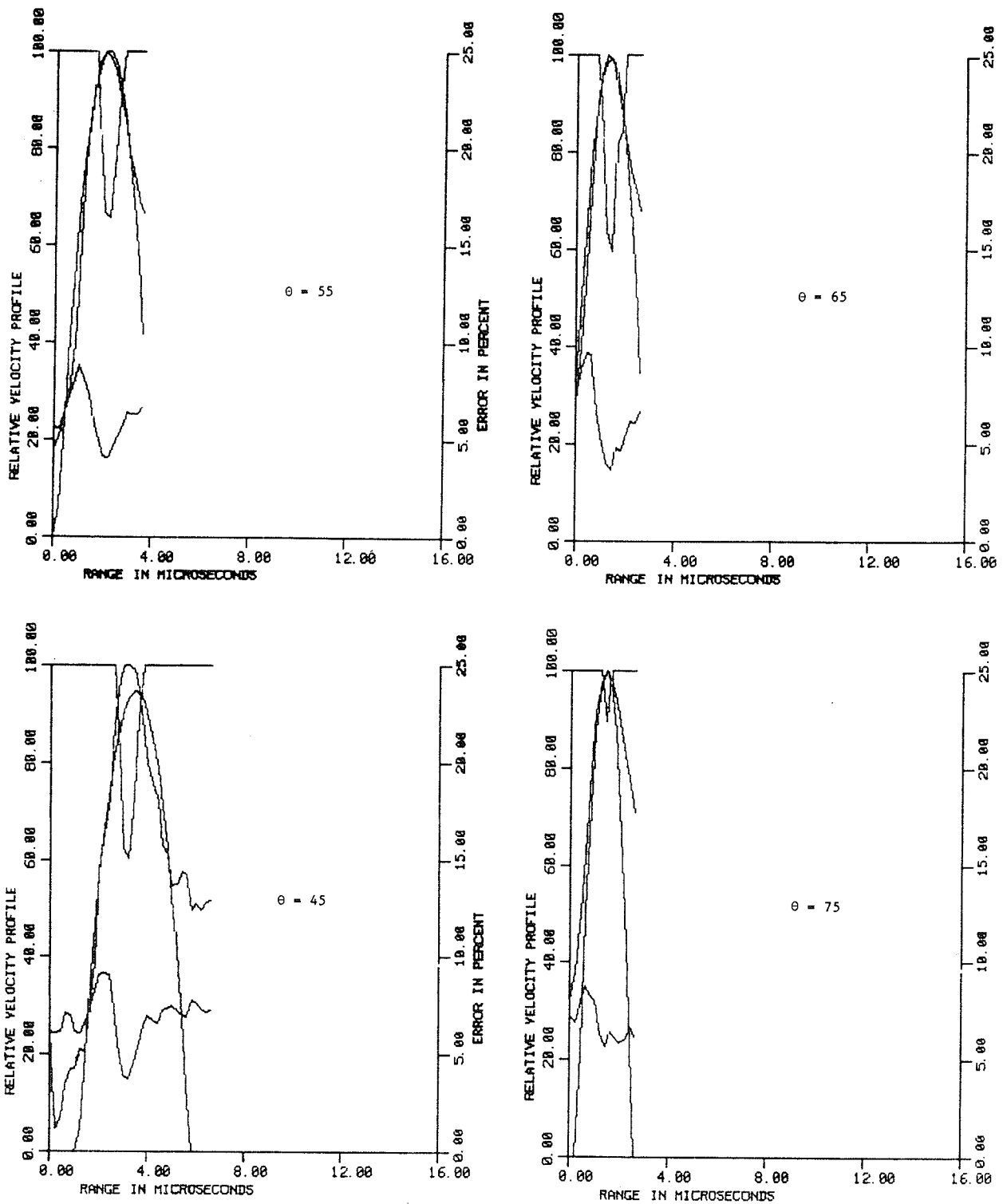


Figure 28. Experimentally measured velocity profile from a tube with a diameter of 7.47 wavelengths (2.24 mm), a correlation length of 4 wavelengths, and a transducer beam width of 2.3 wavelengths. Curves follow the model curves of Figure 16.

estimate of the jitter to be within 9.6% of the actual value of the jitter at the 95% confidence level (if the estimates are Gaussian distributed). When only the velocity profile is needed, the number of averages to take may be only one. The two-minute period could be reduced by three orders of magnitude by using a dedicated number cruncher. More averages are desirable to reduce the statistical error in the estimate of the jitter, but the corresponding increase in time precluded taking more averages. The amount that the scatterers in the buttermilk moved across the beam width between two successive echoes was approximately 10% of the beam width for XTAL1 and 20% for XTAL2 for a viewing angle of 45 degrees. At 75 degrees the amount doubled.

The velocity profiles obtained by the TDM are in Figures 26, 27, and 28. This profile is typically parabolic and somewhat flat at the top where the maximum occurs. The left-hand side of the profile usually gives a higher value than the other parabolic curve that traces the profile. The right-hand side tends to turn upward too.

In Chapter III the estimated profile was compared with the actual profile (see Figure 16). For the experimental examination of the TDM the actual profile is not precisely known. However, an estimate of this profile can be made because the experimental conditions were such as to assure parabolic laminar flow. Therefore, a least squared error parabolic fit [22] to the measured profile was performed on each of the estimated velocity profiles and graphed along with the estimated profile so that the deviation of the

estimated profile from a parabolic profile can be compared with the simulated results of Figures 16, 17, and 18. This profile is distinguishable from the measured profile by its perfect symmetry and smoothness. The midstream value of the parabolic fit is used to normalize the fit at midstream to 100%. The estimated velocity profile and the jitter are also normalized by this value (as are Figures 17, 18, and 19).

The third curve graphed in the figures is the standard deviation of the velocity estimate (jitter). This curve is the lowest curve of the four and its values are read from the left-hand vertical axis. The jitter tends to be smallest at midstream and largest at the wall of the tube.

The fourth curve in the figures is the precision of the estimate given by Eq. (III.1). Values above 25% were truncated to 25%. This curve is distinguished from the others by having a minimum at the center of the graph and both of the sides flattening out at 25% (use the right-hand vertical scale). As in Chapter III the error curve is a measure of the precision of the estimate of the flow.

E. Estimated Speed Linear Dependence on Actual Speed

Equation (II.6) predicts a linear relationship between the estimated shift (estimated velocity is equal to the estimated shift scaled) at a point in the flow using the time domain method to the actual speed at that point. This relationship has been experimentally examined by recording the estimate of the speed at a point for various volume flows and examining how well the data fit a least squared error fit of the data. Assuming that the profile remains laminar over

the volume flow rates, which are always less than 4 ml/s, and, therefore, are theoretically laminar for the tube length used (see Section A), the actual speed at any point should be linearly related to the volume flow. Figure 29 is the least squared error fit of the data taken with XTAL2 (BW of 2.3 wavelengths). The viewing angle was 45 degrees, the vessel diameter was 23 wavelengths (6.96 mm), and the correlation length was 8 wavelengths. The horizontal axis is the volume flow rate and the vertical axis is the measured midstream velocity. The speed of the midstream flow was chosen for analysis since this is the region of lowest error in the estimation of flow (see Figures 26-28 for experimental proof and Chapters II and III for theoretical proof). The choice of the largest vessel for the test of linearity allowed the speed estimation to have the least amount of jitter. The only source of experimental error is the measurement of the true volume flow rate which is approximately 2%. At this time only linearity of the TDM is examined, hence, the raw volume flow data will be used because converting this data to actual flow at the actual range would only increase the error in the horizontal coordinate without adding any other information about linearity. The least squared error line fits the data closely (standard deviation of 0.83%), insuring a linear relationship between measured volume flow and the estimate of midstream speed.

F. Estimated Speed Dependence on Viewing Angle

Theory predicts that the flow rate is directly proportional to the cosine of the viewing angle Eq. (II.6).

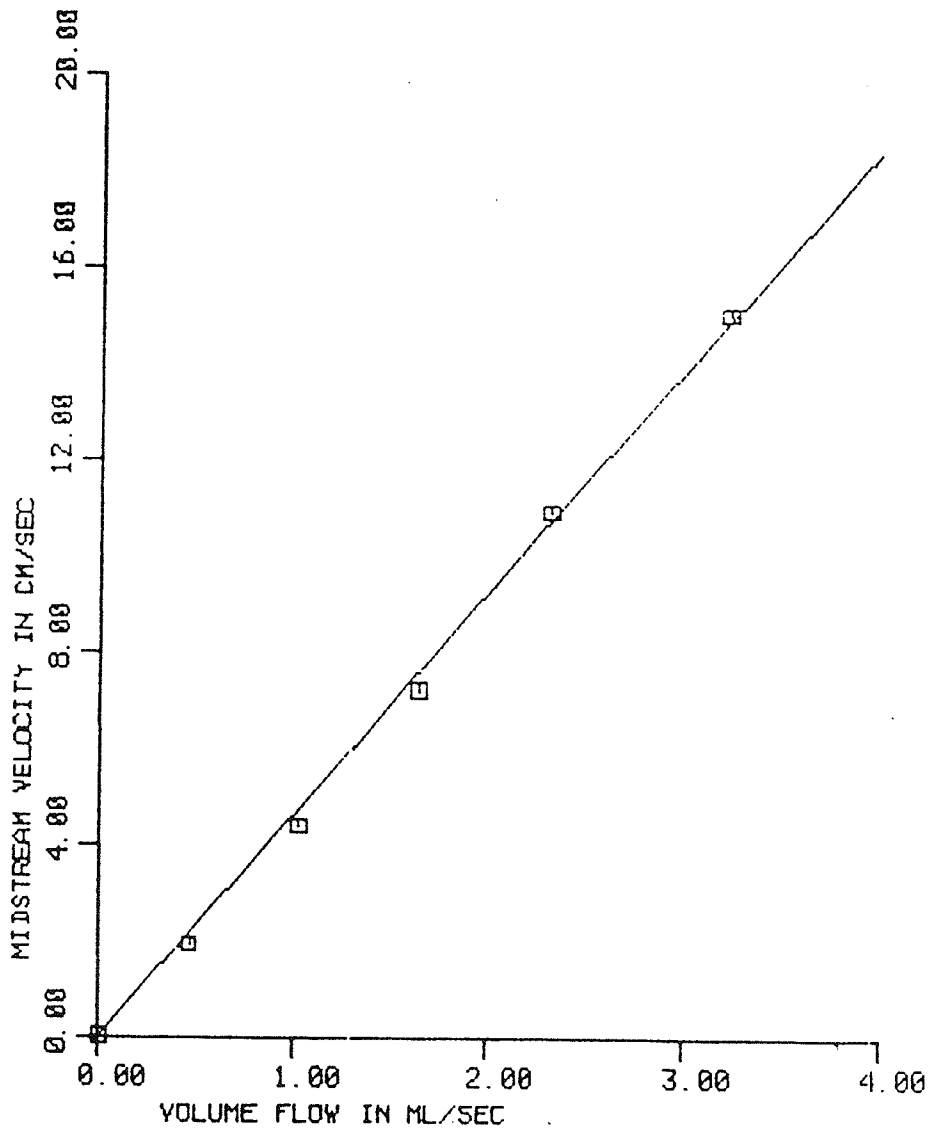


Figure 29. A graph of the measured midstream velocity with the TDM vs. measured volume flow for a tube diameter of 23 wavelengths (6.96 mm), a correlation length of 8 wavelengths, and a transducer beam width of 2.3 wavelengths.

This was experimentally examined by applying the TDM to the estimate of the midstream speed at four different viewing angles (45, 55, 65, and 75 degrees) and three different vessel diameter sizes (23, 13, and 7.5 wavelengths of 5 MHz) under constant midstream flows of 8, 21, and 37 ml/s, respectively. Figure 30 is the plot of the estimated midstream speed of the buttermilk (not normalized by the cosine of the viewing angle) for each of the three sizes of tubing. The three curves in the figure are the least squared error fit of the data for each tube to the curve

$$A \cdot \cos[\theta + 10 \cdot (i-1)], \quad i = 1, 2, 3, \text{ and } 4 \quad \text{Eq. (IV.2)}$$

where A and θ are the variables to be found. The curves in Figure 30 are from top to bottom from the 7.5, 13, and 23 wavelength diameter tubing, respectively. The only parameter varied was the viewing angle, hence, the only source of uncertainty in the deviation of the data from the cosine curve was the uncertainty due to measuring the actual viewing angle. This error is discussed below. Note that the data points closely fit the curve (the standard deviations of the departure of the data from its respective curves are from top curve to bottom curve 0.83, 0.87, and 0.78%, respectively) and the curves all cross the horizontal axis at 90 degrees and have a maximum at 0 degrees, as they must for the cosine function.

In testing for the dependency of estimated speed on the viewing angle, the errors in the measurements of volume flow and tube diameter are independent of viewing angle and,

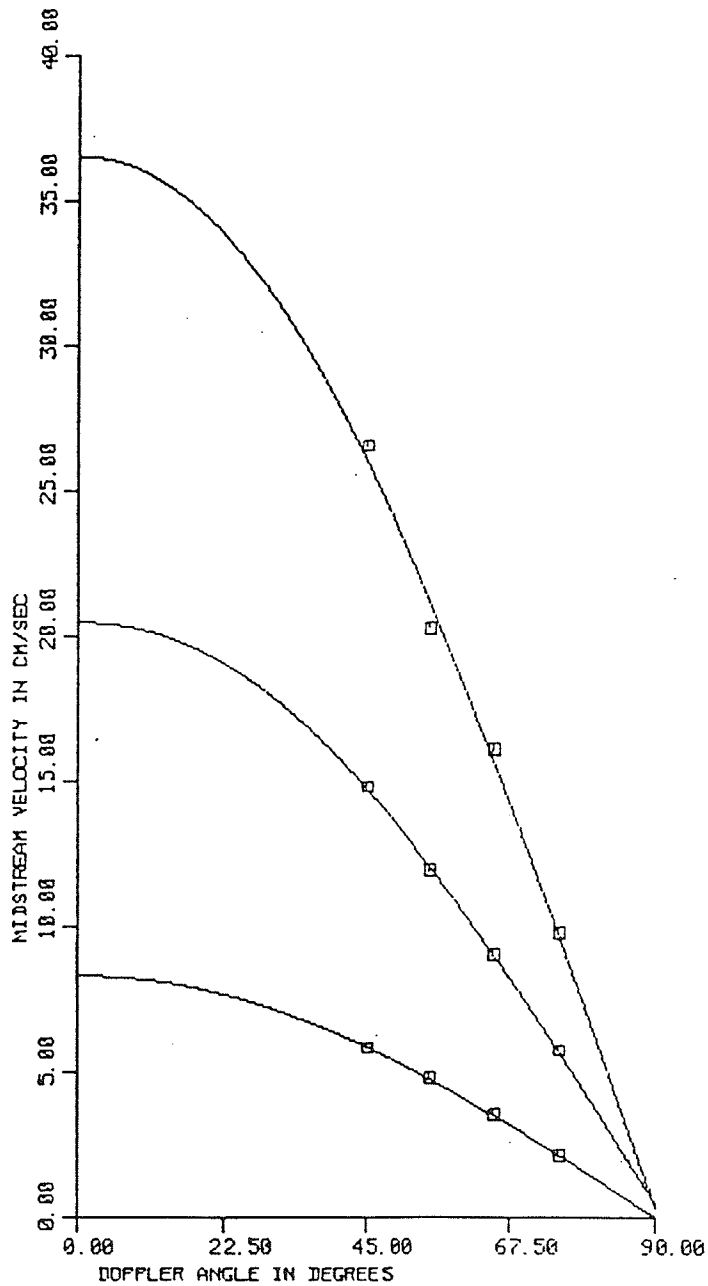


Figure 30. Measured midstream flow dependence on the viewing angle using a transducer with a beam width of 2.3 wavelengths, and a correlation length of 4 wavelengths. Three tube sizes were used; from the top curve to the bottom curve they are 7.4, 13, and 23 wavelengths, respectively.

hence, will not introduce errors into the test. However, there are three other sources of errors affecting the test. They are 1) the viewing angle, 2) the sound beam location relative to the tube axis, and 3) the sound beam refracting between the buttermilk and the surrounding medium.

The viewing angle was determined by first finding the angle that gave the lowest axial speed of the buttermilk under the experimental conditions used to determine the data in Figure 30. The estimated speed at a viewing angle of 90 degrees should be zero since the estimated speed is proportional to the cosine of the viewing angle. The precise angle at which the estimated speed was zero was difficult to ascertain since this null region around 90 degrees was rather broad (± 3 degrees). Once a 90-degree location was determined, the transducer was then rotated 15 degrees to the 75-degree viewing angle and the axial speed was estimated with the TDM. The change in angle was quite accurate with an uncertainty of ± 0.5 degree. Then the transducer was rotated an additional 30 to the 45-degree viewing angle and the axial speed estimated. If the two axial speeds estimates of 45 and 75 degrees were within 5% of each other, then the angles were considered acceptable. If the axial speeds were not within 5% of each other, the procedure was repeated by first adjusting the null angle by one degree (in the direction to increase agreement). The iteration was repeated until the two measurements were in the best agreement possible at the 1 degree resolution (typically, best agreement was when the two measurements were within 5% of

each other).

The equation of the error in determining the viewing angle by the above iterative approach is given by the following:

$$\text{ERROR} = 100 \cdot \frac{\cos(75+\Delta\theta)/\cos(45+\Delta\theta) - \cos(75)/\cos(45)}{\cos(75)/\cos(45)} \quad \text{Eq. (IV.3)}$$

The limits on $\Delta\theta$ for five percent error and assuming no angle dependent bias in the estimate is $[-1.07 < \Delta\theta < 1.03]$. The simulated results of Table III.1 show that the bias in the estimate of midstream flow is weakly dependent on the viewing angle for the correlation length of 4 wavelengths and for the smallest tube for which the bias is strongest (the bias is 3%). The error in the viewing angle as a result of ignoring the 3% bias is $[-1.73 < \Delta\theta < 1.63]$ (the 5% agreement would actually be increased to 8%).

The second source of error causes a potential nonlinearity in the determination of the viewing angle due to refraction between the surrounding medium and the buttermilk. This would cause the transmitted angle of the sound beam to refract in the scatterers to a different angle, as determined by Snell's law. A 1.0% difference in the speed of sound at an angle of incidence of 45 degrees would result in a change in the transmitted angle of 0.5 degree from the incident angle. At an incident angle of 75 degrees the transmitted angle would be off by 2.3 degrees. The speed of sound in buttermilk was determined by the author to be the same as the speed of sound in water (comparison was made at 20°C for both fluids) within an experimental accuracy of +/- 1%. Hence,

the incident angle must be within 2.3 degrees of the transmitted angle at 75 degrees (where refraction is the greatest).

When the experimentally determined viewing angle is different from the actual viewing angle, there will exist a relative error between the measured velocity and the actual velocity. The relative error is defined as the difference between the measured velocity and the actual velocity divided by the the actual velocity, then the ratio is multiplied by 100. From Eq. (II.6) the relative error is the ratio of the cosine of the experimentally determined viewing angle to the actual viewing angle (see Table IV.1).

Table IV.1

Relative error in velocity measurements when the actual viewing angle Θ is different from the experimentally determined viewing angle $\Theta + \Delta\Theta$.

Θ	$\Delta\Theta$						
	-3	-2	-1	0	+1	+2	+3
45	+5.10	+3.43	+1.73	0.00	-1.76	-3.55	-5.37
55	+7.34	+4.92	+2.48	0.00	-2.51	-5.05	-7.61
65	+11.09	+7.42	+3.73	0.00	-3.76	-7.55	-11.36
75	+19.39	+12.96	+6.50	0.00	-6.53	-13.09	-19.67

The third source of error is the alignment of the beam axis with the vessel axis. Without perfect alignment the maximum flow streamline would not be centered laterally with the range cell. Not being perfectly centered on the axis of the vessel is an experimental possibility (the length of the echo is used to determine the position of the axis) since there is no sharp distinction in the length of the echo as the sound beam is moved across the vessel. The reason for

the echo being widest when the sound beam passes through the axis of the tube is that the path the sound takes through the tube is maximal when the beam passes through the axis, and all along this path the ultrasonic energy will be scattered, hence, creating the longest possible echo. The error resulting from missing the axis of parabolic flow can be determined with the help of Eq. (II.11). The error in missing the vessel axis by 10% of the vessel diameter is the value of the flow at $r=D/10$ in Eq. (II.11) which is 0.96 of the axial flow. Hence, the error will cause the results of the estimation of the midstream flow to be low by 4%. The error in missing the midstream streamline is estimated to be less than 10% in the experimental setup.

G. Absolute Agreement Between Estimated Speed and Actual Speed

In this section the absolute agreement between the calculated midstream speed value (section A) and the TDM determination of midstream speed is examined. The bias of the estimate of the midstream speed of buttermilk using the TDM is listed in Table IV.2 for three different tube diameters and two different transducer beam width values. The calculated value of midstream speed is taken to be the actual midstream speed for the bias calculations.

Table IV.2

Amount of experimental bias in estimated flow. The bias of each entry in the table is obtained from a viewing angle of 45 degrees, a correlation length (LEN) of 4 wavelengths, and two different transducer beam widths (BW).

	TUBING DIAMETER (mm)		
	6.96	3.84	2.24
BW=2.3	94.2%	96.9%	75.0%
BW=4.6	96.0%	90.1%	88.9%

In comparing the estimated axial flow speed to the calculated speed, four additional sources of error must be evaluated. They are 1) the measurement of the cross-sectional area, 2) the skewness of the transducer plane of rotation (the plane that contains the viewing angle) to the axis of the tubing, 3) the value of c in Eq. (II.6) (the speed of sound in the scattering medium) needed to determine the speed of the scatterer must be known accurately, and 4) the wavelength difference between the focal region and the plane wave value.

The uncertainty of the tube's cross-sectional area measurement is twice the uncertainty for the diameter measurement. Using the tolerances in the diameter of the tubing listed in Section A, the uncertainties in the measurement of the cross-sectional area are $\pm 4.5\%$ for the 2.24 mm tube, $\pm 2.5\%$ for the 3.84 mm tube, and $\pm 1.5\%$ for the 6.96 mm tube. The uncertainty in measuring volume flow was approximately 2%. The uncertainty in measuring the tube diameter is independent of the uncertainty of measuring volume flow, hence, the uncertainty of the midstream speed is the sum of the two independent uncertainties. The errors in

determining the midstream flow are approximately $\pm 6.5\%$, $\pm 4.5\%$, and $\pm 3.5\%$ for the tubing in order of increasing diameter.

Ideally, the plane that contains the sound beam axes for the four viewing angles should contain the axis of the tube. Otherwise, for example, a 10 degree rotation of the transducer will not correspond to a 10 change in the angle of incidence of the sound beam to the tube axis, hence, the actual viewing angle will not be in agreement with the transducer's angle. The error due to skewness of the transducer plane of rotation to the axis of the tubing consists of a constant scaling factor (independent of the viewing angle) that biases the estimate of actual flow to a lower value. The scale factor is equal to the cosine of the angle of the skewness. For example, if the angle of skew is 10 degrees, then all of the flow estimates will be 98.5% (cosine of 10 degrees) of the actual flow (ignoring all other sources of errors). The angle of skew was unknown in the experimental arrangement but is estimated to be less than 10 degrees.

The estimated speed of the flow is directly proportional to the speed of sound in the buttermilk. As mentioned in Section F, the speed of sound appears to be approximately the same as that in water within $\pm 1\%$. For example, if the speed is 0.5% faster in buttermilk than the 1500 m/s value, then the estimate of the speed of the flow will be lower by this amount.

The results of Table IV.2 are experimental and thus

contain the bias due to the longer wavelength being in the focal region expressed by Eq. (II.8). The results from XTAL1 will be low by 0.39% and XTAL2 by 1.56% when compared to the actual flow speed or to the computer simulation which does not correct for this effect.

The experimental uncertainty in the determination of midstream velocity is at least the sum of the two major sources of uncertainty: the cross-sectional area of the tube and the viewing angle. The uncertainty in the viewing angle can be as great as 1 degree in the procedure discussed in Section F used for finding the viewing angle. From Table IV.1 this would correspond to a 1.76% uncertainty in the midstream velocity measurement. Adding this uncertainty to the uncertainty in the cross-sectional area for the 23 wavelength diameter tube mentioned above (3.5%) results in 5.26% uncertainty in the experimentally determined midstream velocity.

The uncertainty in the experimentally determined midstream velocity for the two smaller tubes is calculated in a similar manner. Since the viewing angle was held constant for the data of Table 4.2, the uncertainty due to the viewing angle is still 1.76%. Adding to this value of uncertainty the uncertainties in the cross-sectional area of the 3.84 mm and 2.24 mm tubes, the total uncertainties are found to be 6% and 8%, respectively.

The values of Table IV.2 were measured experimentally and the correction factor when the wavelength becomes longer in the focal region must be entered. For XTAL1 (BW=4.6) the

values of bias that the TDM should measure are $100\% - 0.39\% = 99.6\%$ and for XTAL2 (BW=2.3) the bias should be $100\% - 1.56\% = 98.4\%$.

The midstream velocity measurement using the TDM for the 2.24 mm tube and for a BW=4.6 resulted in a bias of 75%. If the 8% allowable uncertainty is included, the bias still is outside the 99.6% bias that the TDM should have measured. The lack of agreement between the midstream value determined with the TDM and the experimentally determined midstream velocity is due to the averaging effect of the range cell. When the averaging effects that the simulation predicts (Table III.1) are considered, then the agreement is within experimental error (see Chapter VI for further comparison).

H. Estimated Speed Dependence on the Amount of Shift Between Successive Echoes

The top curve in the two graphs of Figure 31 shows how the velocity estimate varies with the amount of shift between echoes (the bottom curve will be discussed in the next section). Shift is defined as the amount that the correlation procedure has estimated that the range cell has moved in the time interval between successive echoes. The shift is measured in wavelengths (the average period in the echo, hence, a scatterer that has moved 1 wavelength in distance away from the transducer will have moved 2.3 wavelengths in the echo (or shifted 2 wavelengths)). The graphs in Figure 31 are for XTAL2 using a correlation length of 4 wavelengths and a viewing angle of 45 degrees. The estimate is constant except for shifts less than 0.05

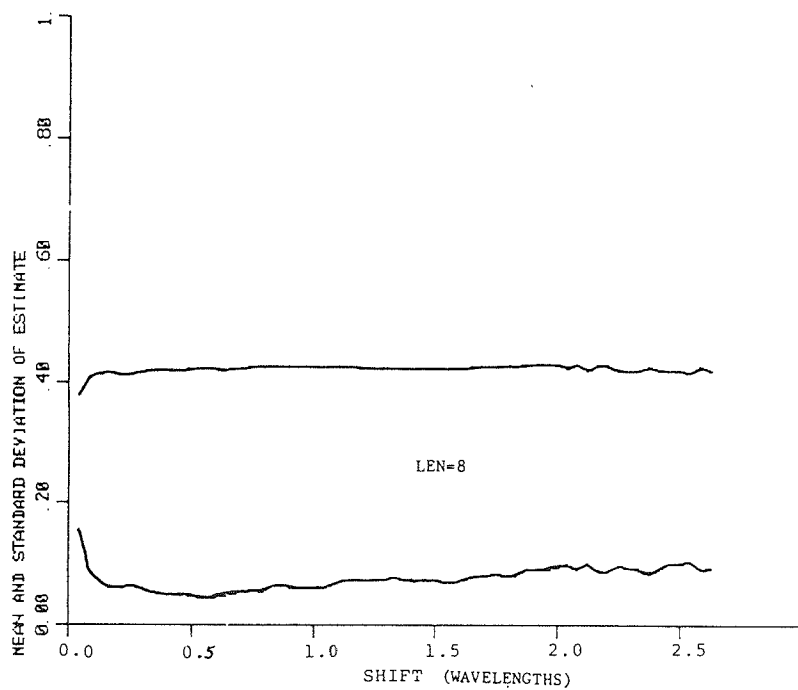
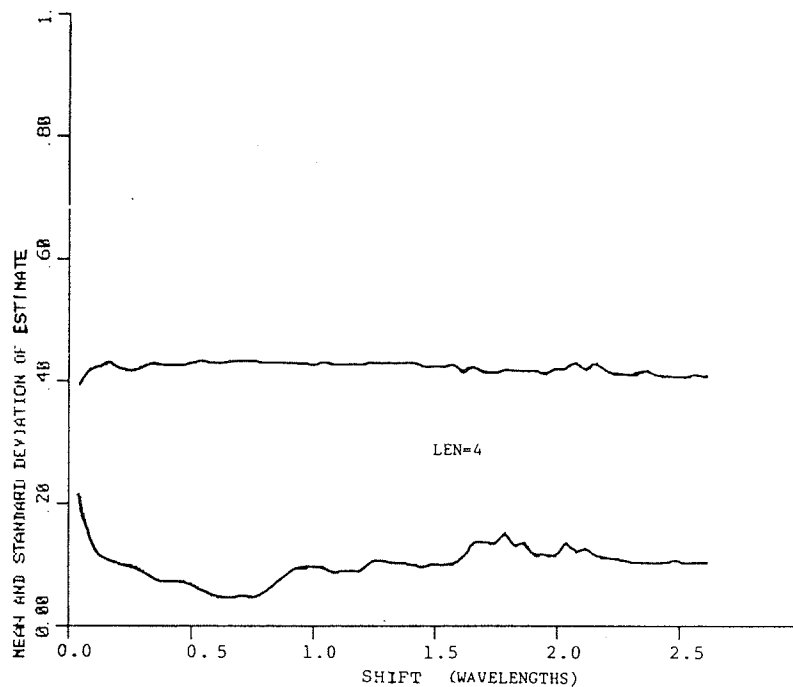


Figure 31. Midstream velocity measurement dependence on time separation between two echoes. The viewing angle is 45 degrees; the beam width of the transducer is 2.3 wavelengths. LEN is the correlation length used.

wavelength. The dip at the smaller values of shift is the result of the bias in the parabolic interpolation (discussed in Chapter V) of the location of the local maximum of the correlation function between the two range cells. The bias resulting from the alignment of two echoes shown is of the order 0.001 wavelength (see Chapter V). Hence, shifts of the order 0.1 wavelength will have a 1% error due to this bias. The error represents no limitation since the optimal shift is around 0.55 wavelength (as will be shown next).

I. Variance of the Estimate of the Midstream Flow

The bottom curves in each of the two graphs in Figure 31 show the precision of the velocity estimation. The mean and standard deviations of the estimate of midstream flow are the results of the statistics from 256 estimates of the midstream velocity using the TDM. Note that the precision has a minimum around a value of 0.75 wavelength for the shift between the two echoes. This is the optimal region to estimate the mean. The curve for a correlation length of 8 wavelengths has a broader minimum region than the 4 wavelength correlation length. The broad range of values for the shift over which the precision was minimized makes the choice of shift not very critical.

Table IV.3 is a tabulation of the precision using the TDM in the estimation of the midstream flow. Two different sized transducers, three different tube diameters, and four different angles were used in the preparation of the table. The midstream flow was selected since the error is smallest

in this region and a significant amount of the total flow occurs here.

Table IV.3

Results of the precision in the estimation of midstream flow. The parameters that are varied are: the beam width of the transducer (BW), the correlation length in wavelengths (LEN), the viewing angle in degrees (THETA), and the diameter of the tube.

		TUBING DIAMETER (in mm)			
		6.96	3.84	2.24	
				
BW=4.6	LEN=4	THETA=45:	2.5	3.0	23
		THETA=55:	3.5	4.0	23
		THETA=65:	4.0	5.0	>25
		THETA=75:	7.5	8.0	>25
BW=4.6	LEN=8	THETA=45:	2.0	2.5	21
		THETA=55:	3.0	3.0	>25
		THETA=65:	3.0	4.5	>25
		THETA=75:	5.0	6.0	>25
BW=2.3	LEN=4	THETA=45:	4.0	5.5	15
		THETA=55:	6.0	6.0	16
		THETA=65:	10.0	10.0	15
		THETA=75:	18.0	23.0	23
BW=2.3	LEN=8	THETA=45:	3.0	4.0	11
		THETA=55:	4.5	4.5	19
		THETA=65:	6.0	7.5	21
		THETA=75:	12.5	15.0	>25

Some observations can be drawn from the data of Table IV.3.

- 1) The precision decreases with the viewing angle. The reason for the decrease is that, as the angle gets larger, more uncorrelated scatterers slip into the range cell, corrupting the echoes.
- 2) As the tube diameter decreases the precision decreases. This is due to the existence of greater velocity gradients across the range cell.
- 3) Larger correlation lengths yield a higher precision except when the lengths are so large as to involve a substantial amount of the vessel (as in the 2.24 mm case), which results in a high velocity gradient across the range cell.

However, the larger correlation lengths allow more data to be averaged which results in a higher precision in regions of uniform flow.

- 4) Generally the less focused the transducer (BW=2.3) the better the precision unless a substantial amount of the vessel is within the range cell. The larger beam width allows more information to be averaged in uniform flow. In regions of high velocity gradients (the narrowest tubing), the more sharply focused transducer will provide better results since the velocity gradients will have a lesser effect.

J. Correlation Coefficient Measurements

The dependence of the correlation coefficient of the two range cells on the amount that their constituent scatterers moved perpendicularly to the sound beam axis has been examined. This was studied by allowing the time interval between pairs of echoes to get larger while determining the correlation between the two range cells at the midstream position. Two correlation lengths and one transducer were used.

If the correlation between two aligned range cells were to be used, the results would be biased since the alignment procedure aligns the range cells so that they are maximally correlated and not necessarily shifted by the actual amount that their constituent scatterers are shifted. For example, if two completely independent segments of BPWGN waveforms are first shifted to acquire a local maximum correlation, then this value is used for the correlation coefficient; the

result will be that these two independent waveforms are correlated (when in fact they were independent). By first determining the average shift for a certain reference PRF and then shifting the range cells by the average shift for the new PRF (without alignment), statistical independence of the correlation coefficient from alignment biases is assured.

To determine the amount to shift the second range cell before finding the correlation coefficient, the average shift per unit time was first determined at some PRF (a nominal value for PRF was 500 Hz). The PRF was chosen so that the average shift between successive echoes was 0.7 wavelength so that the jitter in the estimate of average shift was minimal (see Section I). Then the PRF was set at 8 kHz and 64 successive echo segments were digitized (128 A/D samples of the echo at midstream made up each segment). Next, the range cell of the first echo was correlated with the range cell of each of the successive 63 echo segments at the range that the constituent scatterers of the first range cell had moved in the echo segments. The range was calculated by the time interval between the the first echo and the echo being correlated multiplied by the shift per unit time. In the case that the correlation required a noninteger amount to shift the range cell, the range cell was shifted through three different positions, with the middle position being closest to the noninteger amount. A parabolic iteration was performed to approximate the correlation coefficient at the noninteger value.

Figure 32 is the experimentally measured correlation

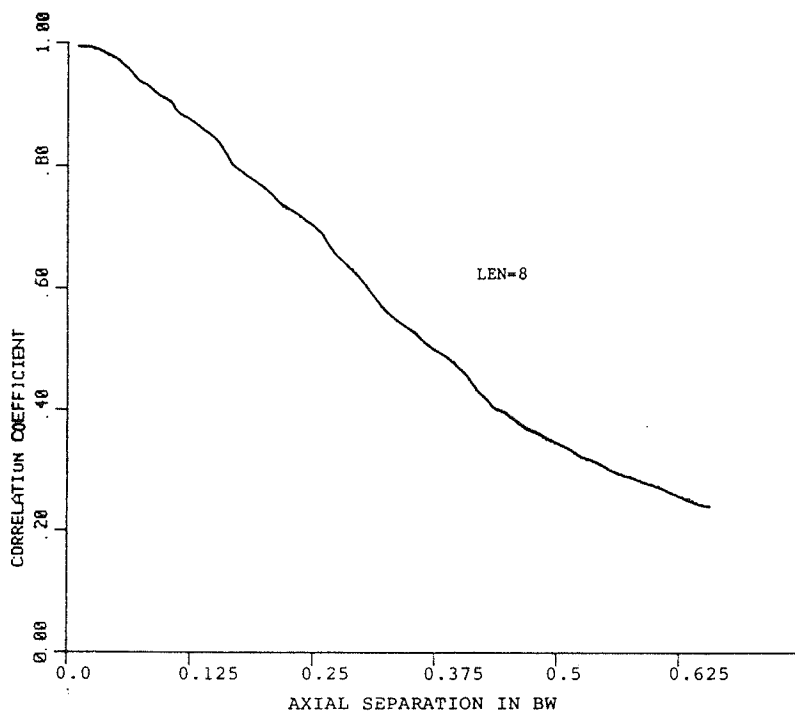
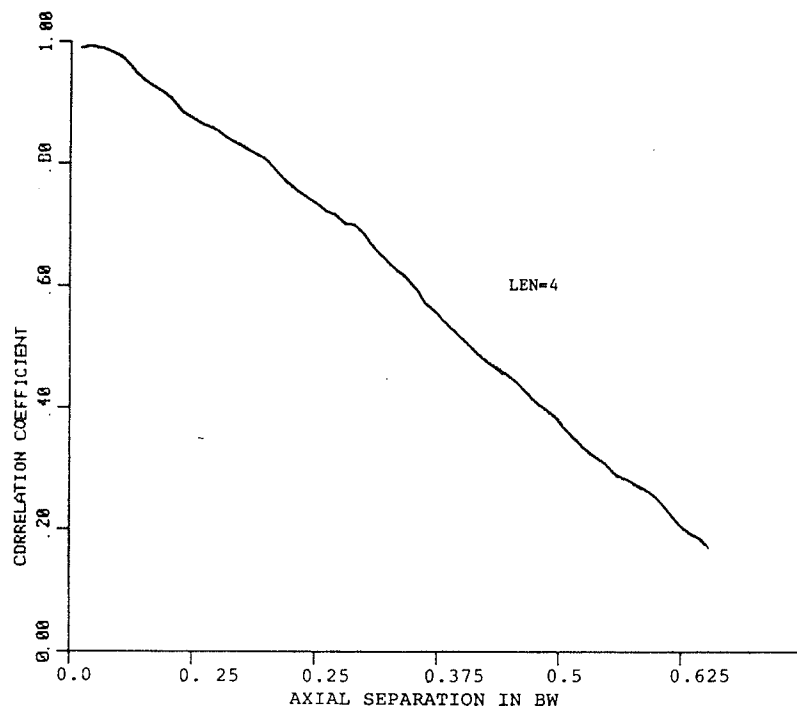


Figure 32. Midstream correlation coefficient dependence on the change in perpendicular distance to the sound beam that the scatterers travel between echoes. A tube diameter 23 wavelengths (6.96 mm), a transducer beam width of 2.3 wavelengths, and a viewing angle of 45 degrees were used.

coefficient between two range cells in the midstream flow as a function of the scatterers' perpendicular displacement relative to the sound beam axis of the second echo moved relative to the first echo. The correlation coefficient is obtained by

$$\frac{\sum_i x(i)*y(i) - \sum_i x(i) * \sum_i y(i)}{\sqrt{\left[\sum_i x(i)*x(i) - \left(\sum_i x(i)\right)^2\right] * \left[\sum_i y(i)*y(i) - \left(\sum_i y(i)\right)^2\right]}}$$

Eq. (IV.4)

where $x(i)$ is the i^{th} member of the correlation window of the first echo and $y(i)$ is the corresponding member of the second echo. The perpendicular displacement is measured in units of the transducer beam width for purposes of comparison with the theoretically derived result of the ideal cylindrical beam of Figure 14. In Figure 14, $h/2r$ ($2r$ is the beam width of the ideal beam used in Figure 10) is equal to the axial separation listed in Figure 32. The data were taken from the midstream point where flow is most uniform. XTAL2 (BW=2.3) was used with the 6.96 mm diameter tube and the top curve was from a correlation length of 4 wavelengths and the bottom curve from 8 wavelengths. The viewing angle was 45 degrees. The choice of XTAL2 allowed the beam width to be small. The choice of the large tube allowed the midstream velocity field to be as uniform as possible. The two curves in Figure 32 are approximately the same. The curve for the correlation length of 4 wavelengths (the top curve) has slightly higher values than the curve for a correlation length of 8 wavelengths. For example, the values of 0.73 and 0.70 are

found at an axial separation of 0.25 BW for the top and bottom curves, respectively.

In an effort to examine how the correlation coefficient is affected by the system parameters of beam width, correlation length, tube diameter, and viewing angle, Table IV.4 was constructed. The correlation was taken at the midstream point and the PRF was set so that on the average the two range cells would need 1 wavelength of shift to align. The value of 1 wavelength was chosen because this value allowed the correlation coefficients of the 6.96 mm vessel to take on midrange values (larger than 25% and less than 75% approximately).

Table IV.4

Experimentally measured correlation coefficients at midstream. The parameters that vary are: the transducer beam width (BW) in wavelengths, the correlation length in wavelengths (LEN), the viewing angle in degrees (THETA), and the tube diameter. The correlation coefficients are for 1 wavelength of shift between successive echoes.

			TUBE DIAMETER (in mm)		
			6.96	3.84	2.24
BW=4.6	LEN=4	THETA=45:	0.79	0.58	0.80
"	"	THETA=55:	0.73	0.51	0.52
"	"	THETA=65:	0.71	0.43	0.42
"	"	THETA=75:	0.62	0.37	0.54
"	LEN=8	THETA=45:	0.78	0.60	0.75
"	"	THETA=55:	0.72	0.53	0.51
"	"	THETA=65:	0.47	0.44	0.45
"	"	THETA=75:	0.41	0.39	0.45
BW=2.3	LEN=4	THETA=45:	0.77	0.60	0.72
"	"	THETA=55:	0.68	0.58	0.71
"	"	THETA=65:	0.59	0.48	0.42
"	"	THETA=75:	0.38	0.26	0.24
"	LEN=8	THETA=45:	0.76	0.77	0.42
"	"	THETA=55:	0.65	0.55	0.30
"	"	THETA=65:	0.55	0.46	0.27
"	"	THETA=75:	0.37	0.22	0.24

Several trends can be observed in the table.

- 1) As the viewing angle gets larger, the correlation coefficient gets smaller. This is a result of more uncorrelated scatterers entering the range cell at higher angles than for lower angles with the same amount of shift between echoes. At higher angles the scatterers move more perpendicularly to the beam axis allowing more uncorrelated scatterers (new to the range cell of the second echo) to enter the range cell than for a range cell at a smaller angle with the same amount of shift between echoes. Hence the correlation coefficient is lowered.

The viewing angle for a large vessel can be determined by comparing the midstream correlation coefficient of the vessel to an experimentally derived table such as Table IV.4. For example, if a correlation coefficient of 0.68 was found using a correlation length of 4 wavelengths and a beam width of 2.3 wavelengths at midstream of a large vessel, then by Table IV.4 the viewing angle is 55 degrees. If the correlation coefficient fell between two values listed in the table, then the angle could be interpolated since the correlation coefficient is monotonic (Figure 32). Once the viewing angle and the shift between successive echoes are known, then by using Eq. (II.6) the speed of the scatterer is determined. Hence, from the shift and the statistics of the range cell of two successive echoes, the speed of the scatterers can be determined.

- 2) In general, the correlation coefficient gets smaller as the diameter of the tubing gets smaller. However, this

trend is violated 50% of the time for the 2.24 mm tube for reasons unknown. This results from the velocity gradients across the range cell becoming larger. It is impossible to align two echoes perfectly (with the present correlation method) that have a velocity gradient across them, because under the best of conditions the second range cell looks like a stretched version of the first and a direct correlation can not compensate for this effect. The lack of alignment keeps some of the data points in the first range cell from being correlated with their counterparts in the second echo.

- 3) The difference between the correlation coefficient for a beam width of 4.6 wavelengths compared with a beam width of 2.3 wavelengths is greatest at the higher viewing angles (where the axial separation is greatest). The theory presented in Chapter II predicts that the correlation coefficient is dependent on the amount of axial separation between the two echoes, normalized (divided) by the beam width of the transducer field pattern. XTAL1 (BW=4.6) has a beam width twice that of XTAL2 (BW=2.3) so that the axial separation in beam width in the case of the echoes from XTAL1 should be twice as small as XTAL2, resulting in a larger correlation coefficient. However, computations assume a uniform flow profile in the range cell. The large beam width of XTAL1 (20% of the vessel if the correlation window length and a nonzero system Q are included) will receive signals from a range of velocities, degrading the correlation.

V. ERRORS INTRODUCED BY QUANTIZATION OF THE ECHOES

The implementation of the time domain method resulted in the conversion of the echoes into a digital format so that the computer could be utilized to investigate the technique. The identified errors associated with the A/D conversion process and data manipulation are as follows:

- 1) the A/D has a finite number of bits of accuracy,
- 2) only a limited number of samples of the waveform may be taken per wavelength, and
- 3) the correlation function will exist only at discrete points and the maximum can (and does most of the time) fall between two points, hence limiting the accuracy of the estimation of the correlation peak.

The estimation of the value of a point in the echo will have an uncertainty of plus or minus one half of the least significant bit (LSB) and the uncertainty is normally assumed to be uniformly distributed within these bounds [25]. The variance of the uncertainty is $1/12$ the width of an LSB squared [25]. This is equivalent to a 50 dB signal-to-noise ratio for a sine wave with a peak-to-peak voltage covering the entire range of the 8-bit A/D [25].

When comparing the waveform in a range cell of an echo with the waveform in the aligned range cell of the successive echo, it is found that the two waveforms do not look exactly alike. By subtracting the aligned range cell waveform from the first, the noise in the second waveform is found. The signal-to-noise ratio can then be found by squaring and then integrating the difference (by Simpson's rule) and then dividing by the average power in the second echo (squaring and integrating). For a nominal experimental setup of a

viewing angle of 45 degrees, a shift between range cells of 0.7 wavelength, a tube of diameter 6.98 mm, and a transducer BW of 2 wavelengths, the measured signal-to-noise ratio varied between 18 and 28 dB. The noise in the echo is from the scatterers changing their positions with respect to the beam position, rather than electronic sources of noise. Hence, in comparison to the noise in the aligned range cell of the successive echo, the finite resolution of the A/D represents an insignificant error.

A computer simulation was performed to analyze the dependence of jitter (the standard deviation of the estimate of a point in the velocity profile) on the number of bits of the A/D. In the simulation a segment of BPWGN ($Q=4$) was generated (as discussed in Chapter II.C.1). The sampled value of each point in the segment was then truncated to the desired number of bits, and that segment was correlated with itself. The position of maximum correlation was determined and this procedure repeated a large number of times (2048) so that doubling the number showed no statistical difference in the estimate of the jitter at the 95% level. The results of the simulation are shown in Figure 33 for three correlation lengths, which allow the effect of correlation length on the jitter to be studied. From Figure 33, 4 bits of resolution differ less than 0.1% from 8 bits of resolution. Hence, it is not necessary to have more than 4 bits of resolution (to remove stationary echoes, more are probably needed) for the TDM because the jitters from beam width modulation and velocity gradients are far greater (see Chapter II.D).

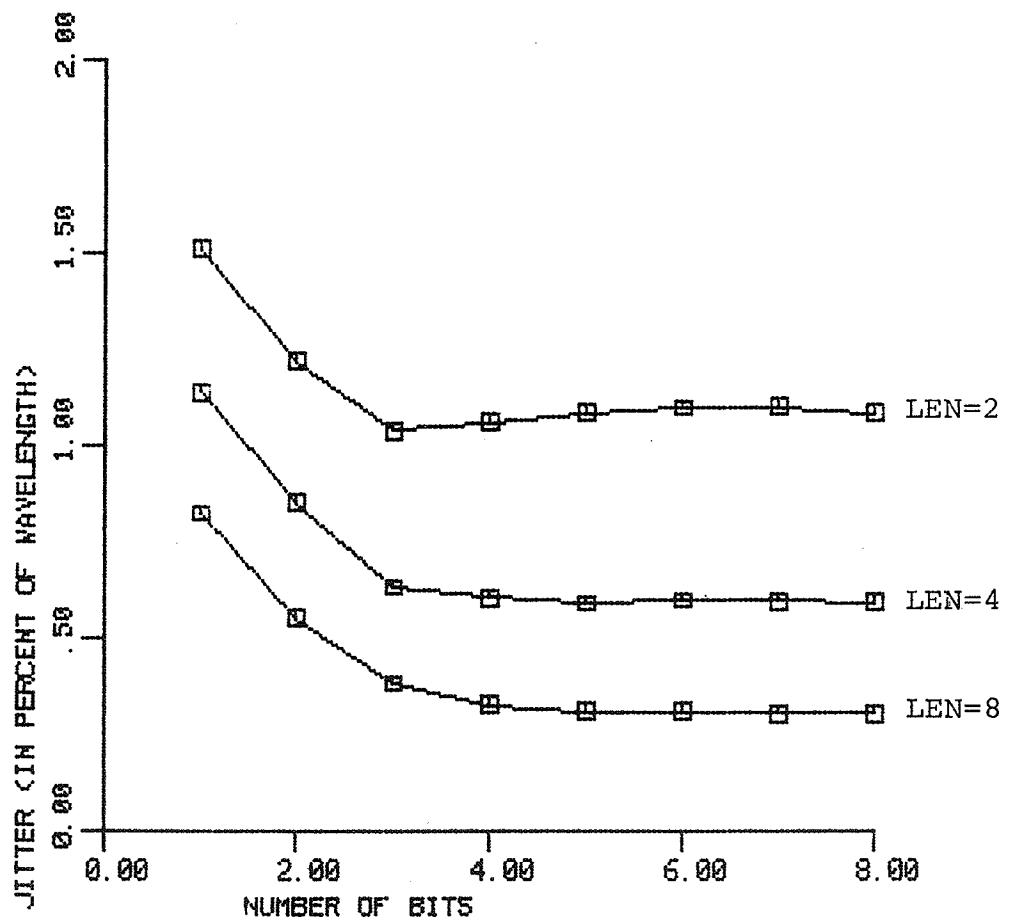


Figure 33. A graphical representation of jitter as a function of the number of bits of resolution of the A/D for various correlation lengths (LEN).

The effect of lowering the number of bits of resolution on estimating the velocity profile of a parabolic profile is shown in Figure 34. The curves were generated by changing the number of bits of resolution in the simulation program of Chapter III. The parameters of a typical system used in this thesis were used in the simulation: vessel diameter of 12 wavelengths, beam width of 2 wavelengths, correlation length of 4 wavelengths, a viewing angle of 45 degrees, and a system Q of 4. In the figure, the parabola is the actual velocity profile. The other four curves are the jitter curves resulting from the different number of bits of resolution. Note that using 1 or 2 bits of resolution increases the jitter by only 2%.

The number of samples per wavelength of the echo is limited by the size of the memory necessary to hold the samples and the maximum sampling rate of the A/D. However, since the echoes are band limited it is necessary to sample at only twice the rate of the highest frequency in the signal. In this work, typically, 10 samples are taken at four times the highest frequency to reduce the effect of aliasing from the residual energy outside the band. The experimental system employed in this study sampled at 8 times the highest frequency.

The Nyquist theorem states that the values of the echoes between the samples may be recovered completely if sampled at or above the Nyquist rate. When recovering a value of a waveform between two sampled values of the waveform with an A/D with finite resolution, the recovered point is a random

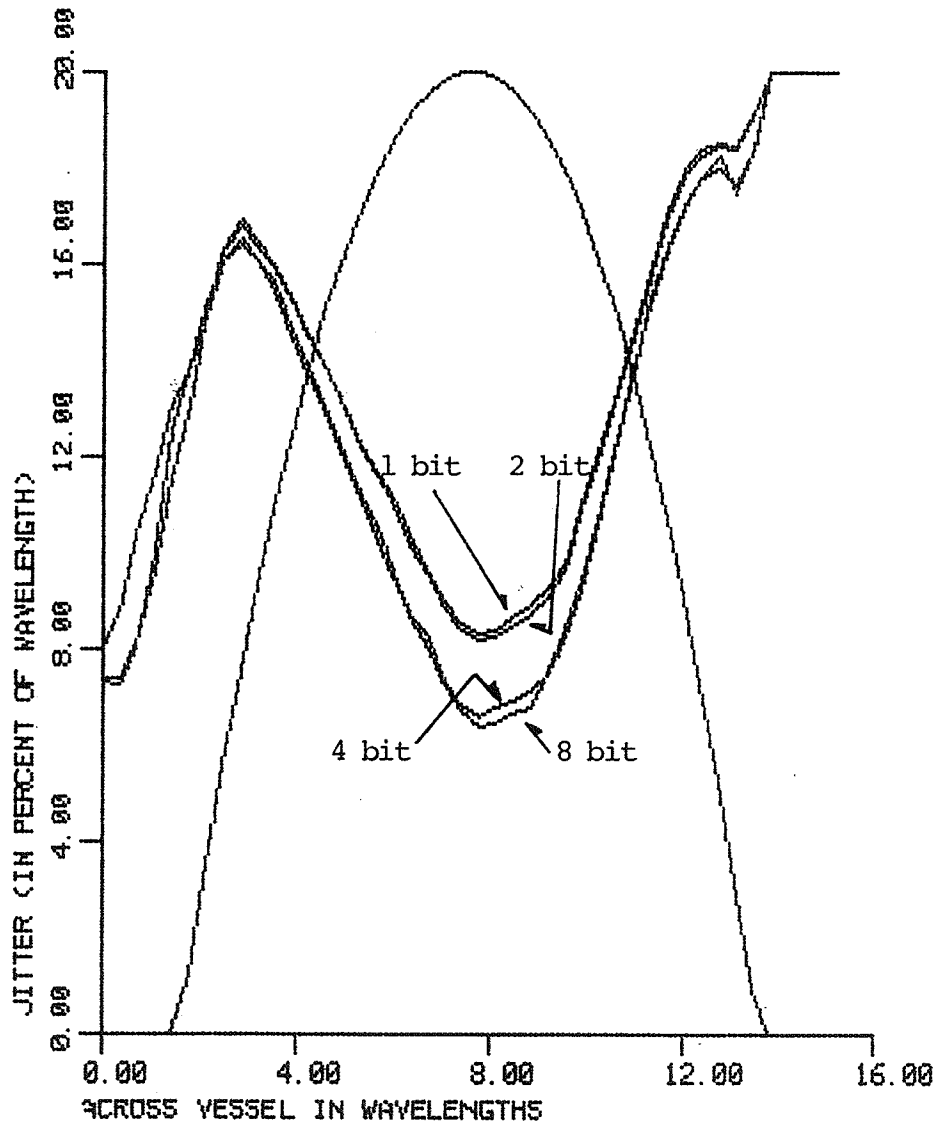


Figure 34. A graphical representation of the jitter associated with the velocity profile estimation of a parabolic profile using different number of bits of accuracy. The parameters used in the simulation were: a vessel diameter of 12 wavelengths, a transducer beam width of 2 wavelengths, a correlation length of 4 wavelengths, a system Q of 4, and a viewing angle of 45 degrees.

variable with a mean equal to the true value of the data point in the waveform. The variance is identical to the variance associated with the finite resolution of the A/D. Hence, sampling above the Nyquist rate will not give a better estimate of the echo than sampling at the Nyquist rate and interpolating. The proof follows.

From the Nyquist theorem all points of the waveform may be recovered by

$$f(t) = \sum_{k=-\infty}^{\infty} f(k) \cdot \text{sinc}(t-k), \quad \text{Eq. (V.1)}$$

where $f(t)$ is the recovered point, $f(k)$ is the sample of $f(t)$ at point $t=k$, and the sampling period is assumed to be one unit of time. The sample from the A/D, $\tilde{f}(k)$, can be modeled as the true signal at the quantized point $f(k)$ plus the noise associated with the quantization noise $n(k)$.

$$\tilde{f}(k) = f(k) + n(k) \quad \text{Eq. (V.2)}$$

The noise has a mean of zero and a variance (σ^2) of $1/12$ the least significant bit (LSB) squared, and uniformly distributed between $-LSB/2$ and $+LSB/2$. The autocorrelation function is the Dirac impulse function scaled by σ^2 (quantizing errors are assumed to be independent from sample to sample providing that several A/D states were passed, which is the usual case) [25]. The recovered point at time t is given by

$$\tilde{f}(t) = \sum_{k=-\infty}^{\infty} [f(k) + n(k)] \cdot \text{sinc}(t-k). \quad \text{Eq. (V.3)}$$

The mean of $\tilde{f}(t)$ is identical to the mean of $f(t)$ where $E[.]$

is the expectation operator:

$$\begin{aligned}
 E[\tilde{f}(t)] &= E\left[\sum_{k=-\infty}^{\infty} (f(k)+n(k)) \cdot \text{sinc}(t-k)\right] \\
 &= \sum_{k=-\infty}^{\infty} E[f(k)+n(k)] \cdot \text{sinc}(t-k) \\
 &= \sum_{k=-\infty}^{\infty} f(k) \cdot \text{sinc}(t-k) \\
 &= f(t) \qquad \qquad \qquad \text{Eq. (V.4)}
 \end{aligned}$$

The variance of $\tilde{f}(t)$ is determined by

$$\begin{aligned}
 \text{Var}[\tilde{f}(t)] &= E[(\tilde{f}(t)-f(t))^2] \\
 &= E\left[\sum_{j=-\infty}^{\infty} \sum_{k=-\infty}^{\infty} n(j) \cdot n(k) \cdot \text{sinc}(t-j) \cdot \text{sinc}(t-k)\right] \\
 &= \sum_{j=-\infty}^{\infty} \sum_{k=-\infty}^{\infty} E[n(j) \cdot n(k)] \cdot \text{sinc}(t-j) \cdot \text{sinc}(t-k) \\
 &= \sum_{j=-\infty}^{\infty} \sum_{k=-\infty}^{\infty} \sigma^2 \delta(j-k) \cdot \text{sinc}(t-j) \cdot \text{sinc}(t-k) \\
 &= \sigma^2 \sum_{k=-\infty}^{\infty} \text{sinc}^2(t-k)
 \end{aligned}$$

But $\sum_{k=-\infty}^{\infty} \text{sinc}^2(t-k) = 1$. This is the dc response from a triangular filter in the frequency domain centered at the origin.

$$\therefore \text{Var}[\tilde{f}(t)] = \sigma^2 \qquad \qquad \qquad \text{Eq. (V.5)}$$

The correlation function is available only at discrete

points. Since frequently the maximum will not fall at these points, some way of estimating the maximum must be found. The autocorrelation function of a band limited waveform is also band limited (even more severely than the waveform) [26]. The complete autocorrelation function could be determined by the Nyquist theorem; however, this is a time-consuming computation. A shorter method would be to take the maximum point and its two neighboring points of the discrete correlation function, fit a parabola to the points and determine the maximum of the parabola. Using the point with the largest value and its two neighbors, the position on the x axis where the maximum occurs is given by

$$x = \frac{f(x_0+1) - f(x_0-1)}{2 \cdot [f(x_0+1) - 2 \cdot f(x_0) + f(x_0-1)]} \quad \text{Eq. (V.6)}$$

where the terms are shown schematically in Figure 35.

The jitter associated with determining the point of maximum correlation from the above approximation is graphed in Figure 36 for a BPWGN signal with a 6 pole, 1 dB ripple, bandpass Chebyshev response. The jitter was determined by computer simulation. In the simulation a BPWGN waveform was generated; a second waveform was generated from the first by shifting the first waveform from -0.5 to +0.5 of a sample point in 17 steps. This was accomplished by generating the BPWGN waveform at 16 times the sampling rate under examination. The first waveform consisted of every sixteenth sample point beginning with the ninth point in the enlarged waveform. The second waveform was generated by starting with a point contained in the first seventeen positions and then

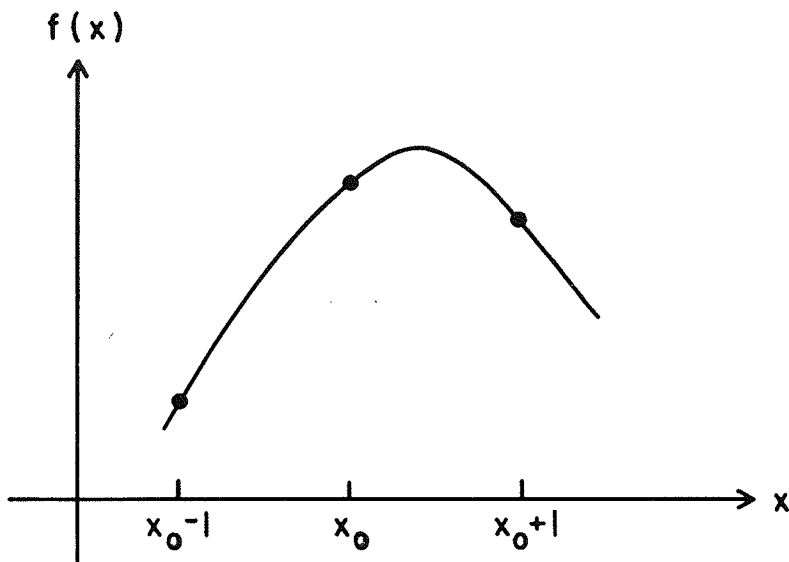


Figure 35. A graphical representation which shows that the three points of the correlation function can be approximated by a parabola.

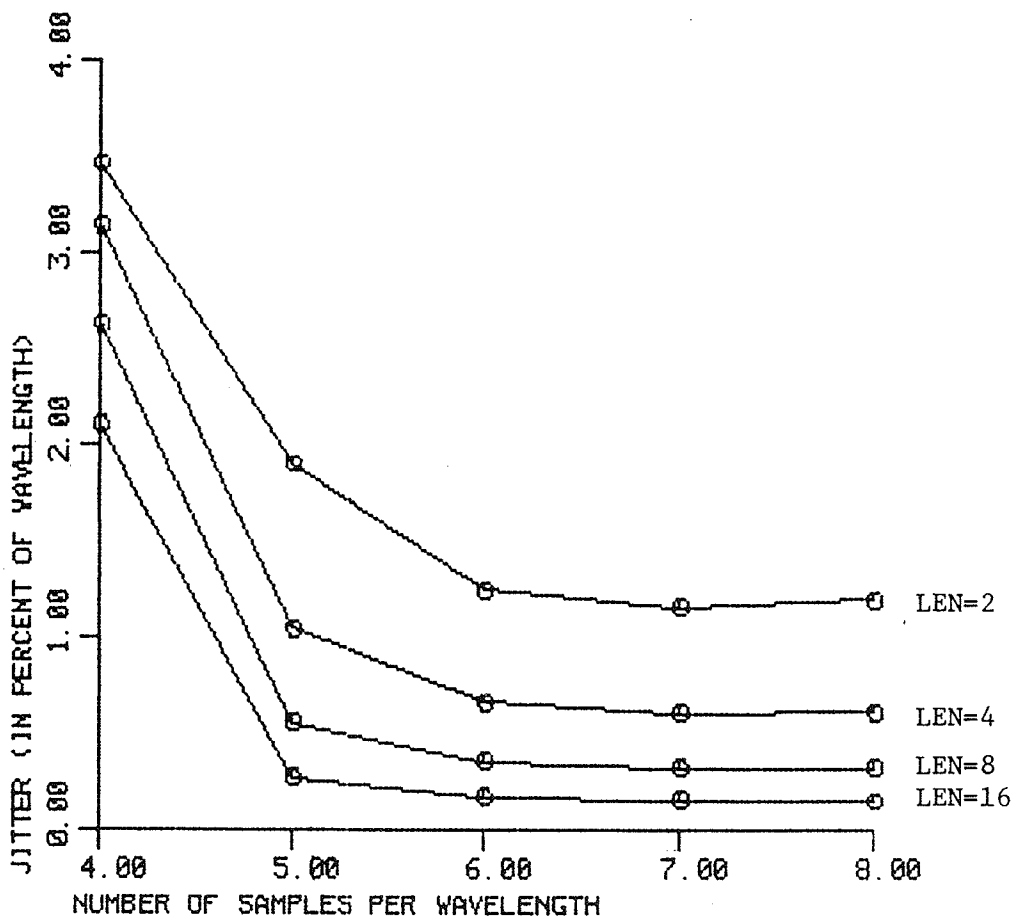


Figure 36. Jitter associated with determining the maximum point of correlation due to the parabolic approximation of the correlation function using the quantized data points under various correlation lengths (LEN). The system Q is 4.

skipping every sixteenth point. Next the two waveforms were passed through the correlation algorithm. The amount of shift from the actual offset was recorded and the procedure was repeated a number of times (2048) so that doubling the number resulted in no statistical difference in the jitter at the 95% level. The Q of the experimental system ($Q=4$) was taken as the Q for the simulation in Figure 36. The number of samples per wavelength and the length of the correlation window strongly influence the jitter.

The measured shift from the actual shift was found to be slightly biased. The bias was on the order of 0.01 of a sample point, causing the estimate of actual shifts that were greater than zero to be more positive, and those estimates of actual shifts less than zero to become more negative. For example, if the actual shift is 0.80 of a sample point, then the estimate will be 0.79, an underestimate of the shift. This effect can be seen in the experimental results graphed in Figure 31 where the mean of the estimate decreases slightly for small values of shift. The shifts most often sought are near 0.7 wavelength, corresponding to 7 sample points with the 50 MHz A/D used, hence, this bias is negligible.

The jitter from the parabolic approximation (Figure 36) flattens out at about 6 samples per wavelength. The apparent dips at 7 samples per wavelength for the correlation lengths of 2 and 4 are statistically insignificant at the 95% level used in the figure. From Figure 36 it is apparent that sampling above 6 samples per wavelength will decrease the

jitter by less than 0.25%, which is a minor improvement when the jitters from beam width modulation and velocity gradients are considered (in all the simulations and experimentally determined jitter in the velocity profile estimate in this work, the jitter has never been less than 2.5%). Note that as the correlation length becomes greater the jitter decreases, as shown in Figure 7 in Chapter II. The errors in the approximation of the maximum of the correlation function are considered negligible in the experimental results (there were 10 samples per wavelength in the experimental system used).

VI. DISCUSSION

A. Comparison Between Computer Simulation of the Theory and Experimental Results

The echo from buttermilk was shown in Chapter IV.C to have a Gaussian probability distribution and a bandpass spectrum. It follows then that buttermilk provides a BPWGN scattering medium. The scattering strength of blood may be greater than that of buttermilk, but this is not an important factor in the TDM since the gain of the preamp is adjustable to compensate for a difference in scattering strength; the signal from buttermilk is of sufficient strength that noise from the preamp is small, at least 40 dB down. Hence, buttermilk is a suitable replacement of blood in examining the TDM.

In comparing the experimentally estimated profiles by the TDM on three vessel sizes, 23, 13, and 7.5 wavelength diameters shown in Figures 26, 27, and 28, respectively, with the roughly equivalent simulated estimated profiles in Figures 17, 18, and 19, respectively, several trends are observed. The estimated profiles are flatter at midstream and broader at the vessel wall than their companion ideal parabolic curves. The estimated velocity profiles in the simulation and the experiment are symmetric about the midstream value. In Figures 26, 27, and 28 the estimated velocity profile and the jitter were not normalized by the actual midstream value as were Figures 17, 18, and 19, because the actual midstream value was not known. Hence, no comparison between Figures 17, 18, and 19 can be made with

Figures 26, 27, and 28 concerning the relative heights of the estimated velocity profile to the actual parabolic profile from these graphs.

In Chapter IV.G the estimated midstream velocity using the TDM was found to be in apparent disagreement with the experimentally measured values. For example, the estimated midstream value, using the smallest diameter tube (7.5 wavelengths, 2.24 mm) and the transducer with a beam width of 4.6 wavelengths, was measured to be 75.0%. The maximum uncertainty was approximately 8%. The bias value of the TDM should have ideally read is 99.6% (this includes the effect of the wavelength of sound becoming longer in the focal region). However, the averaging effect of the large range cell to vessel diameter ratio has not been considered. In the simulation where averaging is considered, the value of bias for a vessel with a 6 wavelength diameter is 76.8% (Table III.1), hence, the values are within experimental error. When the effects of averaging are included (use Table III.1) then the estimated midstream velocity is in agreement with the experimentally measured flow.

The figures that contain the velocity profiles (both simulated and experimental) also contain the jitter associated with estimating various parts of the velocity profiles. Note that the jitter is smallest at midstream and largest at the vessel walls as are the jitters in Figures 17, 18, and 19, except for 75 degrees in Figure 17. However, at 75 degrees the jitter in Figure 26 (the rough experimental equivalent of Figure 17) is nearly flat, hence, the

discrepancy between the two figures is not great.

Comparing the results of the experimental precision curve with the simulated precision curve in the figures, the following trends are observed. The precision is largest at midstream and smallest at the sides in both sets of figures. As the viewing angle increases, or as vessel diameter decreases, the precision becomes worst. The precision curves of Figures 26, 27, and 28 does not touch the jitter curves as in Figures 17, 18, and 19 because the precision curves of the former figures are scaled differently to enhance the midstream precision readability.

The degree of precision at midstream flow using the TDM experimentally can be compared with the precision of the simulation by comparing Tables IV.2 (page 101) and III.1 (page 67), respectively. Table IV.2 shares the results from 23, 13, and 7.5 wavelength diameter tubes. Table III.1 uses roughly the same diameters: 24, 12, and 6 wavelengths. The author considers a factor of 2 difference between the experimental precision and the simulation precision to be significant. Searching the first column (largest vessel) in both tables, the difference in precision is found not to be significant. For the second column of the two tables only one entry of the 12 entries is found to be significantly different, the one for $BW=4$ and $LEN=4$. The precision is found to be experimentally 2.2 times better than for the simulation. The reason for the disagreement is unknown but could perhaps be attributed to a statistical fluke. For the third column in the tables there is no significant

difference.

Equation (II.6) predicts that the shift between two successive echoes is linearly related to the axial velocity of the flow. This was shown to be true in Chapter IV.E with the help of Figure 29 (see Chapter IV.E for the details). The equation also predicts that the amount of shift is linearly related to the time duration between the two echoes. This was experimentally verified in Chapter IV.H with the help of Figure 31 (see Chapter IV.H for the details). The simulation does not vary midstream velocity or the time interval between echoes, but varies the amount of axial positional change ($\Delta s = VT$) between successive echoes. Equation (II.6) predicts a linear relationship between shift and Δs . The data in the table list the bias of the estimate of the midstream velocity for various amounts of Δs . The amount of bias is found for various amounts of Δs to be the same, indicating that Δs and the amount of shift between successive echoes are linearly related.

Equation (II.6) predicts that the measured shift between two successive echoes is directly related to the cosine of the viewing angle. The data of Table III.1 support this relationship. The data were taken from the largest vessel (24 wavelengths) where the velocity field is the most uniform since Eq. (II.6) assumes uniform flow. Looking at the data for the range cell with the minimum amount of jitter (BW=4, LEN=8), the biases of the four viewing angles are all within $\pm 0.1\%$ of each other. Some disagreement should be expected because as the viewing angle becomes larger the range cell

averages an increasing amount of the velocity profile which tends to lower the bias. The experimental dependency of the measured midstream velocity on the four viewing angles is shown in Figure 30. The deviations of the four data points for the 23 wavelength tube are within experimental error (see Chapter IV.F).

There is an optimal value of shift to allow between the range cells of two successive echoes in the measurement of midstream velocity. The shift that produces the best precision (defined by Equation III.1) will be defined as the optimal value of shift. The optimum value of shift must be large enough so that the jitter associated with the correlation procedure is much smaller than the estimate of the mean midstream flow (see Figure 7). However, the optimum shift must not be so large as to incur a large amount of jitter from beam width modulation (see Figure 12). Hence, the optimal value of shift lies between these two extremes. The theory of Chapter II did not determine the value of optimal shift, but in Chapter III (Table III.2) the optimal value is shown to be broad, and the jitter changes less than $\pm 0.4\%$ for shifts from 0.25 to 1.00 wavelength for the LEN=4 case. The jitter does not change at all for the LEN=8 case for shifts between 0.25 and 0.75 wavelength. The 24 wavelength vessel, the transducer with a 2 wavelength beam width, and a viewing angle of 45 degrees were used in the simulation to generate Table III.2. In Chapter IV the optimal value of shift is found experimentally by graphing the amount of precision against the amount of shift. In the

figure, the optimal value of shift is found to be broad and to lie between 0.5 and 0.75 wavelength. The vessel and transducer used in the preparation of the graph had a 23 wavelength tube diameter, a 2.3 wavelength beam width, and a viewing angle of 45 degrees. Hence, the simulation and the results of the experiment show that the optimal value of shift is broad and lies in the region of 0.5 to 0.75 wavelength for the above system parameters.

The field pattern used to approximate the pulsed field pattern of the transducer in the simulation had the following characteristics: equally spaced phase fronts, constant intensity in the axial direction of the beam, and an Airy distributed intensity across the beam. Since the above remarks show that the experimentally observed results are in agreement with the simulation with the noted few exceptions, the field pattern used for the approximation of the pulsed field pattern appears to be valid within the above listed agreement criteria.

The agreement between the correlation coefficient of the experimentally determined value and the theoretical value for various shifts will now be compared. In Figure 14, $h/2r$ is equal to the axial separation listed in Figure 32. The experimentally obtained correlation coefficient taken from the midstream flow of the largest tube (23 wavelengths) where the flow is most uniform is graphed against the amount of shift between successive echoes in Figure 32. The horizontal axis of Figure 32 was scaled so that the axis is in the same units as the theoretical graph (Figure 14). The theoretical

graph is the correlation coefficient from an ideal cylindrical sound beam. On comparing the measured dependency of the correlation coefficient on the amount that the scatterers move perpendicularly to the beam axis (Figure 32) with the ideal theoretical results of the cylindrical ideal sound beam (Figure 14), it is observed that both curves are monotonically decreasing at about the same rate. The value of the correlation coefficient for an axial separation of 0.25 BW from Figure 14 is 0.68, which is lower than the value of 0.73 obtained from Figure 32. Exact agreement between the two curves is not expected because the theoretical curve is a result of a greatly simplified field pattern. However, independent of the agreement, the values in Figure 32 would provide an excellent lookup table for the transducers used with the listed correlation lengths.

B. Comparison of Pulsed Techniques with the Time Domain Method

In this section the TDM and pulsed and pseudorandom Doppler methods will be compared as to their measurement of the velocity profile and the amount of jitter in the measurements.

Since both the TDM and the frequency domain methods use an acoustic range cell with nonzero dimensions, the estimate of the velocity profile will be biased by the averaging of the velocities in the range cell. Hence, the estimated profile will be flatter at midstream than the actual profile and will taper off slowly at the wall of the vessel.

Jorgensen [3] has measured the amount of bias at midstream using pulsed Doppler. The diameter of the vessel was 6.85 mm, the viewing angle was 60 degrees, the center frequency of the transducer was 5 MHz, and the 3 dB length of the range cell was 4.2 mm. The amount of bias was found to be 70%. The length of this range cell is longer than any range cell used in this thesis for a comparable size vessel (6.96 mm). However, using the TDM with typical parameters, the bias is 94.2% (see Table IV.2). The typical parameters are: 6.96 mm vessel, 4.6 wavelength transducer beam width, system Q of 4, transducer center frequency of 5 MHz, a correlation length of 8 wavelengths, and a Doppler angle of 45 degrees. The lower value of bias reported by Jorgensen is expected since the range cell is larger than the typical TDM range cell, and hence the larger range cell will average the velocity profile more which results in a lower bias.

It is not possible to compare the jitter of pseudorandom and pulsed Doppler techniques with the TDM since the literature does not contain the jitter of the two Doppler techniques [5, 6, and 7].

The TDM can be shown in theory to have a smaller amount of jitter in the estimation of flow than pseudorandom or pulsed Doppler techniques. There are two main sources of errors in pulsed Doppler techniques that the time domain method does not share; 1) pulsed (and pseudorandom) Doppler techniques are estimating a random variable, the mean Doppler shift and 2) pulsed Doppler techniques do not use all the available energy in the echo. Using the BPWGN model for

echoes from a scattering medium, Angelsen [27] calculated the error (the standard deviation of the estimate of the mean Doppler shift divided by the mean of the Doppler shift) in the estimation of the mean Doppler shift. He has shown that for a 5% error, 73 cycles of the mean Doppler shift must be used in the estimation. On the other hand, the TDM using the experimental arrangement in Chapter IV yielded an error of 3% (Table IV.3) with only two echoes processed. (The table averaged 256 velocity profiles to get a better estimate of the jitter, and fewer samples are needed for a good estimate of the mean.) The time between the two transmitted echoes was about half the period of the mean Doppler frequency. Since the velocity estimates of the TDM are roughly independent of each other after a period of time has passed equal to the Doppler shift period, approximately 73 independent estimates of the speed of the scatterers could be found in the time period that the pulsed Doppler method took to achieve 5% error. Hence, the velocity estimate from the TDM could be averaged over the same time to reach an error of less than 1%.

The time domain method uses all the energy in the pulse (and not just one spectral line as in pulsed Doppler techniques). Hence pulsed Doppler techniques will have a lower signal-to-noise ratio than the TDM. The decrease in the signal-to-noise ratio is proportional to the duty cycle of the transmitted ultrasound; the decrease can be as great as 19 dB (see Chapter I).

The disadvantage of the time domain method could be the

cost of the high speed A/D and the processing circuits. The frequency domain methods use inexpensive circuitry similar to that found in a radio.

C. Further Predictions of the Simulation in Chapter III

In Figure 37 the degree of bluntness of the flow is varied for a 12 wavelength diameter tube, with a viewing angle of 45 degrees, a correlation length of 8 wavelengths, and a beam width of 2 wavelengths. Note that the variance of the estimation of the flow is constant in the midstream. Hence, for the parabolic flow case most of the error in the midstream must be a result of beam width modulation and not velocity gradients (otherwise the error in the parabolic case would be larger than for the other cases).

Figure 38 is the computer simulation of the effect of increasing the beam width of the transducer. The vessel is 6 wavelengths across, inclined at 45 degrees, and the beam width has values of 2, 4, 8, and 16 wavelengths (starting in the lower left and proceeding clockwise in the figure). Note that as the beam width is increased the midstream estimate becomes biased downward and the error increases. For the case of a beam width of 16 wavelengths the estimation of midstream speed is near 50% of flow which is in fact the average flow in the vessel (and in the range cell).

In Figure 39 the correlation length is varied (2, 4, 8, 16 wavelengths) for a 6 wavelength vessel inclined at 45 degrees. The midstream flow is biased downward to 67% of flow (for the length of 16). The average flow of the scatterers in a line through the vessel axis is 67% of

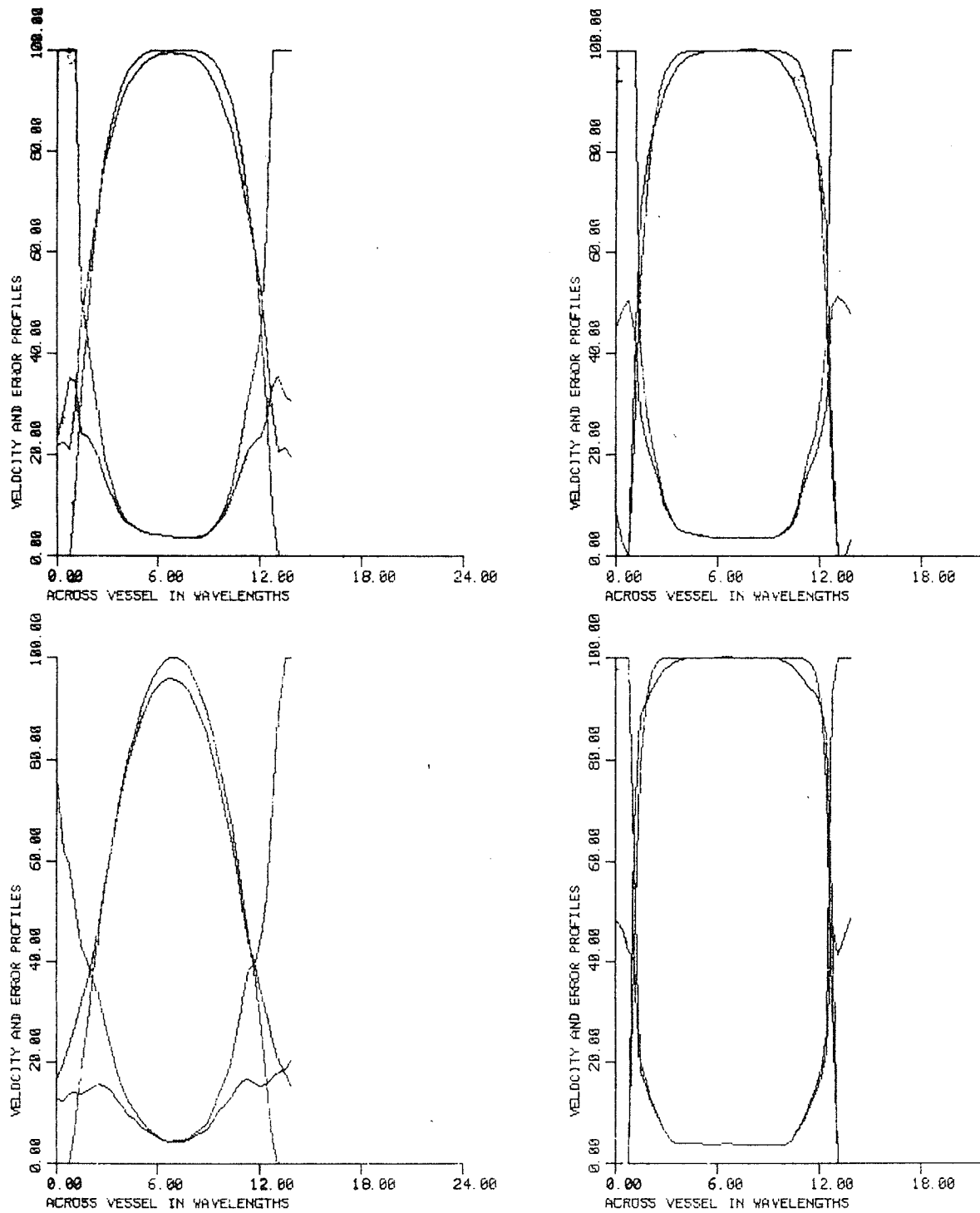


Figure 37. Results of the computer simulation when the degree of bluntness in the flow is varied. The parameters (in wavelengths) used are: vessel diameter of 12, correlation length of 8, transducer beam width of 2, a system Q of 4, and a viewing angle of 45 degrees.

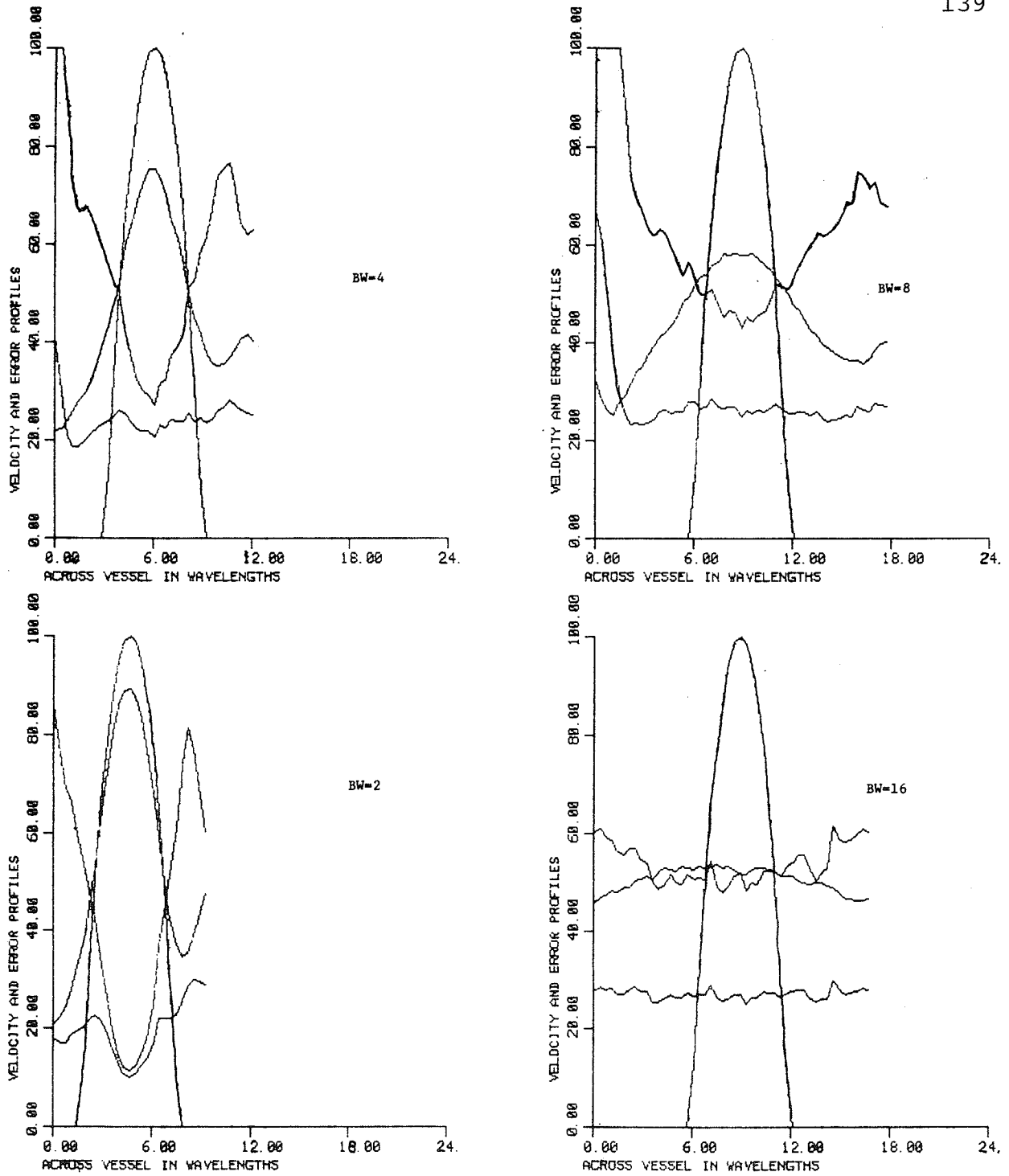


Figure 38. Results of the computer simulation where the beam width of the sound beam was varied. The parameters (in wavelengths) used are: vessel diameter of 6, correlation length of 4, a system Q of 4, and a viewing angle of 45 degrees.

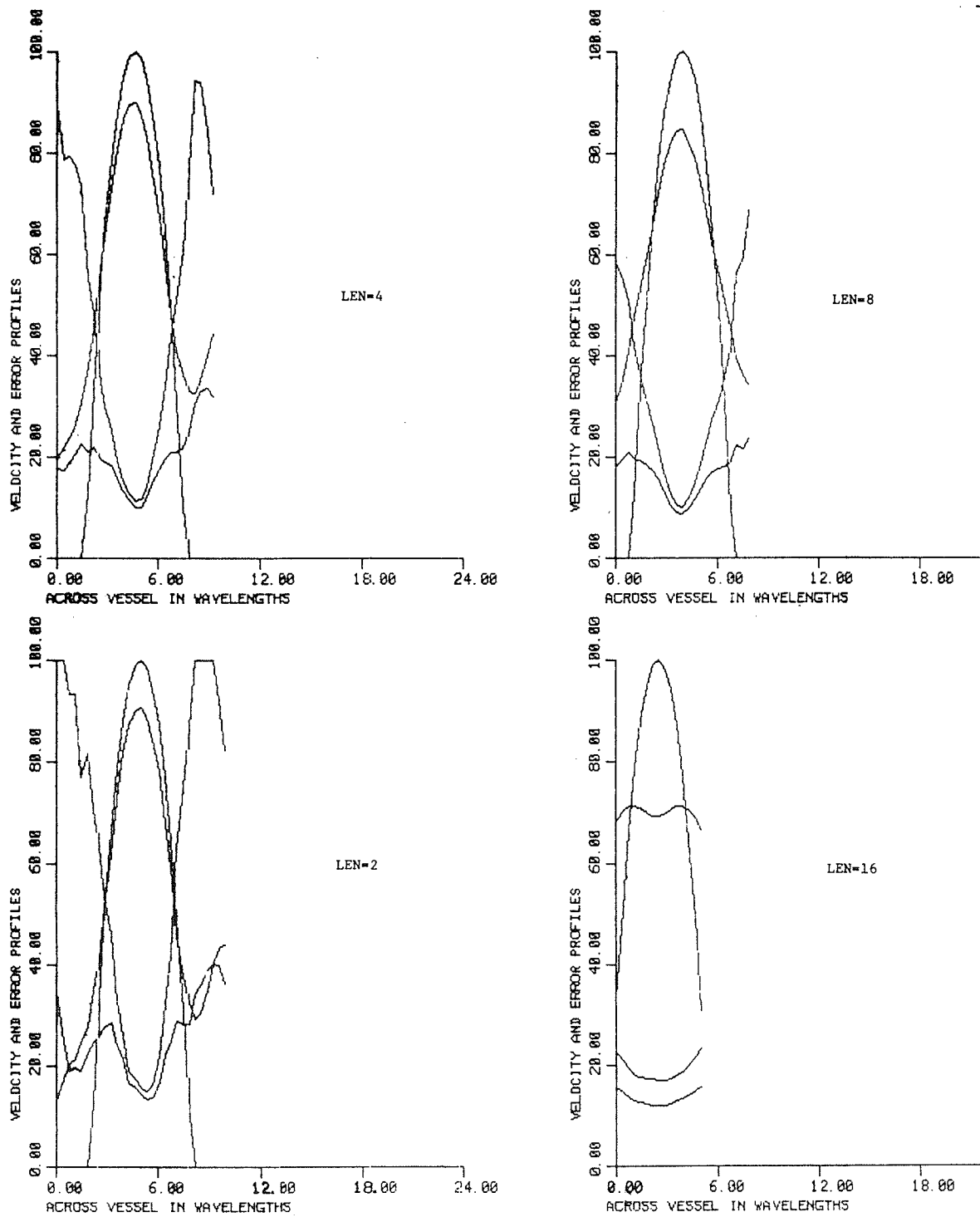


Figure 39. Results of the computer simulation when the correlation length (LEN) was varied. The parameters (in wavelengths) used are: vessel diameter of 6, transducer beam width of 2, a system Q of 4, and a viewing angle of 45 degrees.

midstream flow. The range cell in the case where the correlation length is 16 wavelengths is a long narrow beam through the vessel (approximating a line).

Figure 40 illustrates the effect of system Q on the determination of the velocity profile. The vessel is 6 wavelengths across and inclined at 45 degrees. The Q used in each graph is 1, 4, 16, and 64 starting at the lower left and proceeding clockwise. The jitter increases with Q because the range cell length becomes larger with increasing Q . A larger range cell length causes a greater velocity gradient to occur across the range cell which leads to an increase in jitter (Chapter II.D). The range cell for the system Q of 64 is a long narrow beam passing through the vessel. From Eq. (II.15) we find that the half power width of the impulse response of a system Q of 64 is about 26 wavelengths. Since the viewing angle is 45 degrees, the power width corresponds to a 9 wavelength distance (perpendicular to the beam axis) across the 6 wavelength vessel. Hence, the half power width of the impulse response is larger than the diameter of the vessel. The estimate of midstream flow is biased downward to 67% for increasing flow which is exactly the average value of the speed of the scatterers along the sound beam.

D. Scaling

The results of the simulation can be scaled to any size wavelength provided the A/D continues to take at least eight samples per wavelength.

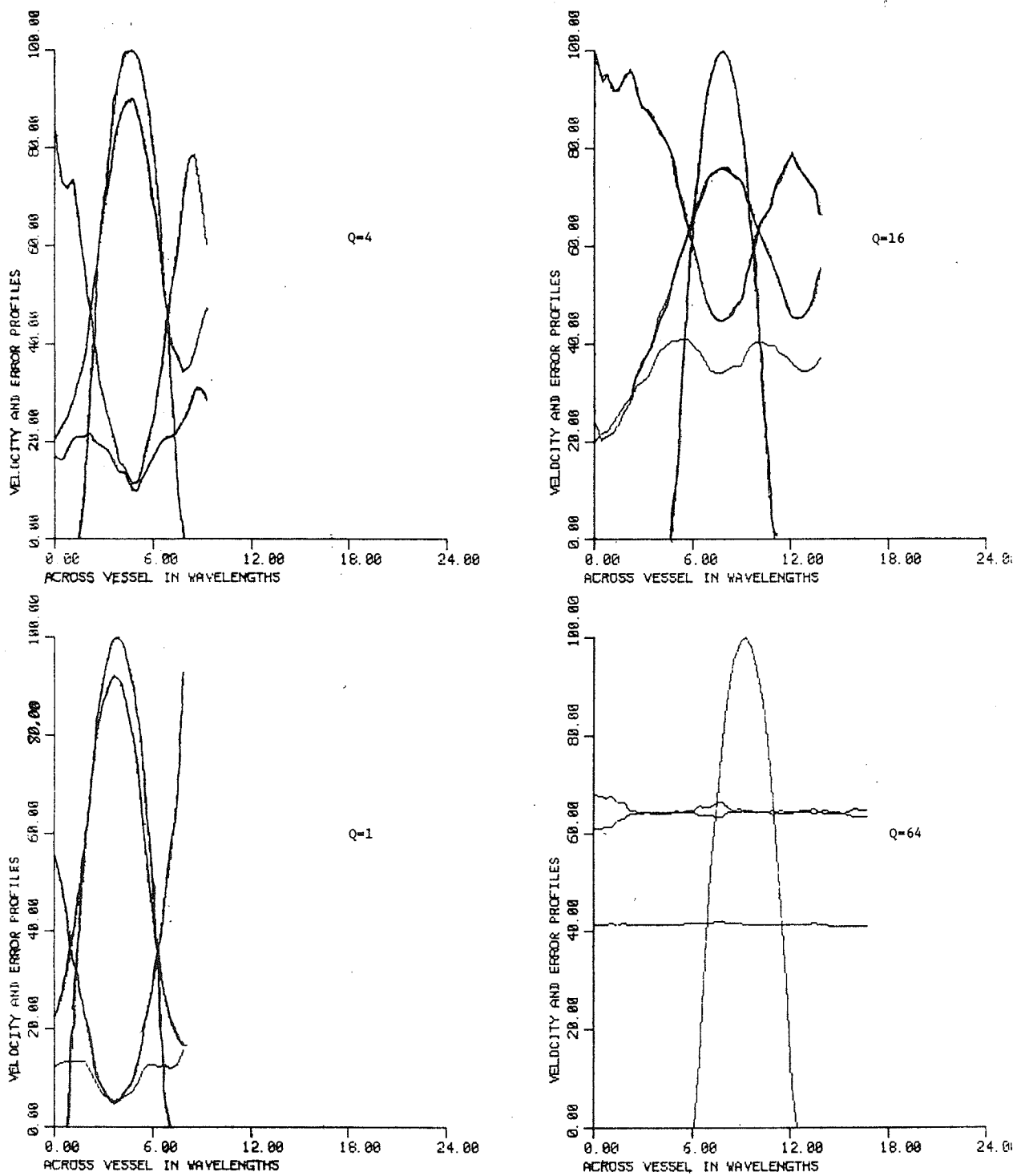


Figure 40. Results of the computer simulation when the system Q was varied. The parameters (in wavelengths) used are: vessel diameter of 6, correlation length of 4, transducer beam width of 2, and a viewing angle of 45 degrees.

VII. IMPROVEMENTS FOR THE TIME DOMAIN METHOD

One of the most troublesome aspects of the experimental system was the uncertainty in the Doppler angle. A fixture should be machined so that the rotation plane of the transducer would contain the axis of the vessel.

The possibility of a different correlation algorithm or type of window to apply to the echoes should be studied to see if the jitter could be reduced further over the current value.

Chapter V showed that the simulation needed only 1 bit of resolution in the A/D to determine the velocity profile across a vessel with only a 2% increase in jitter over the 8-bit resolution simulation. An A/D with 1-bit of resolution (a comparator) should be tried experimentally to see if the jitter also increases only 2% as in the simulation. If the increase in jitter is acceptable, then the correlator would reduce to a serial binary adder, which would simplify a hardware correlator design. TRW makes a high speed LSI chip for a 1 bit correlation (TDC1023J).

Further research should be directed towards finding the optimal values of transducer beam width, system Q, and correlation length for a given vessel with a given axial flow and Doppler angle.

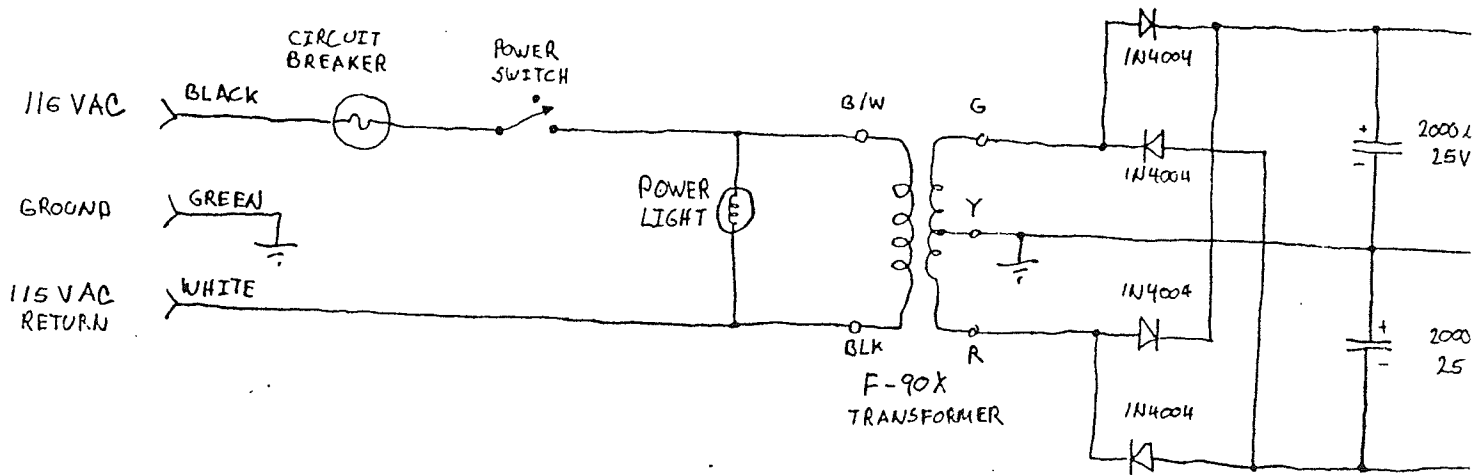
Additional research must be directed towards determining the dependence of the correlation coefficient and the system's ability to estimate the velocity for vessel diameters approaching the range cell size.

A two-dimensional scan through the cross section of the

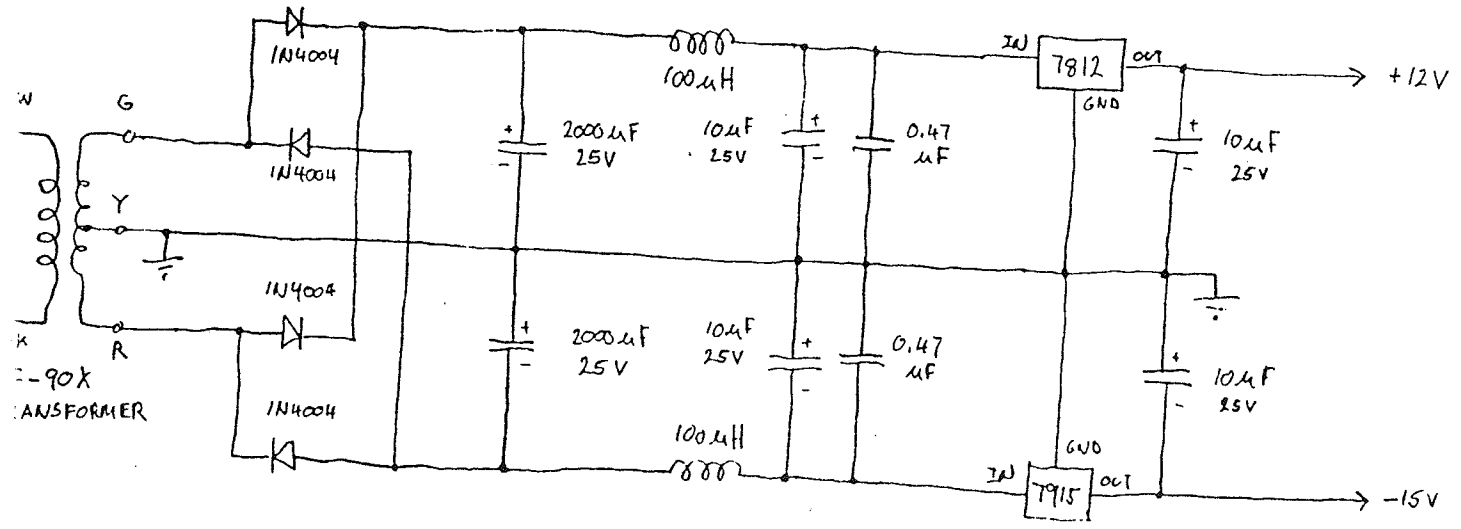
vessel is possible. This would solve the problem of orienting the plane for sweeping the transducer beam so that it contains the axis of the vessel.

The timing problems of having two A/D's running a half cycle off from each other (so that a 50 MHz rate could be achieved) can be circumvented by using a 75 MHz 8-bit flash A/D produced recently by TRW.

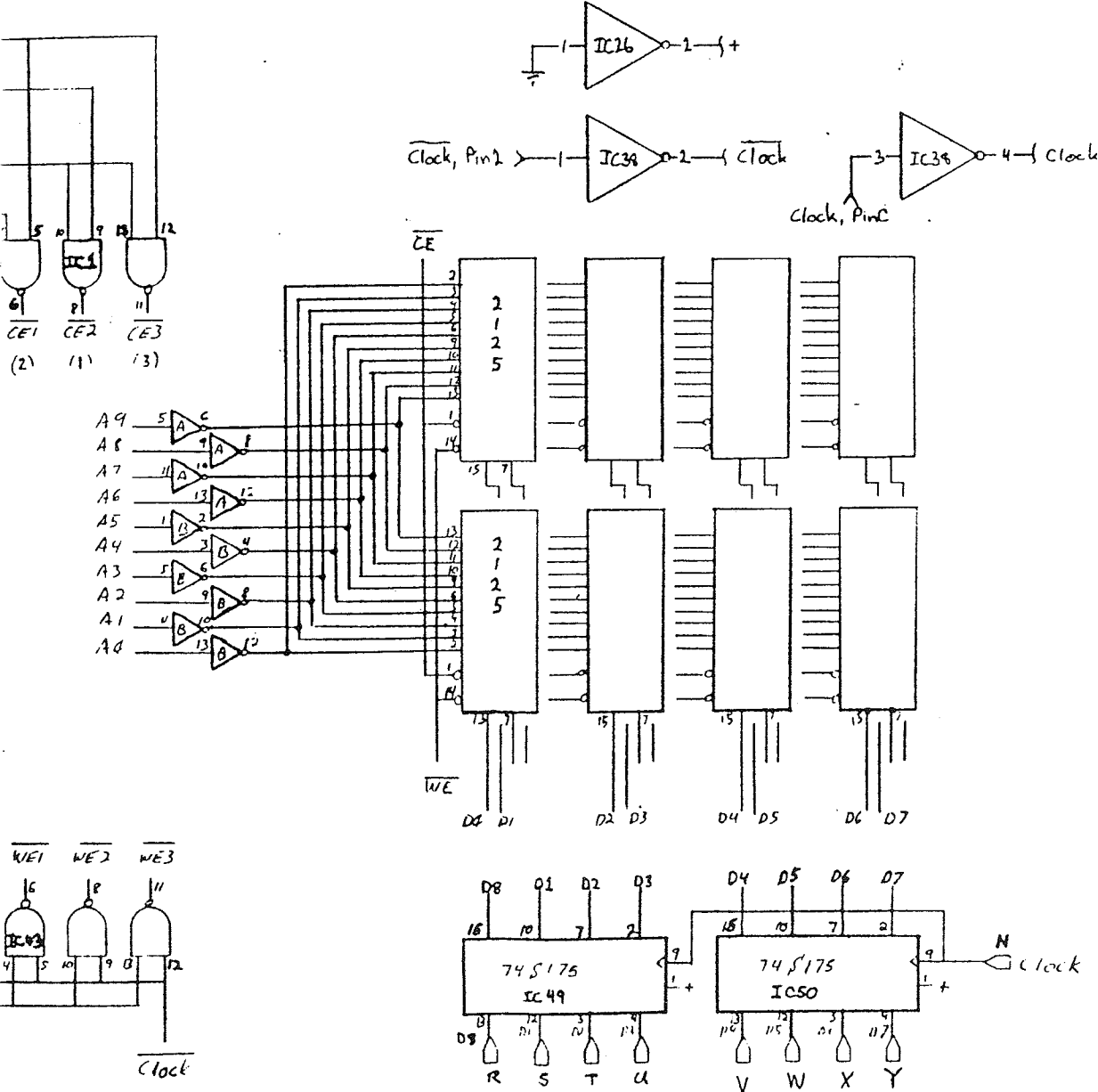
APPENDIX
FLOW CHARTS

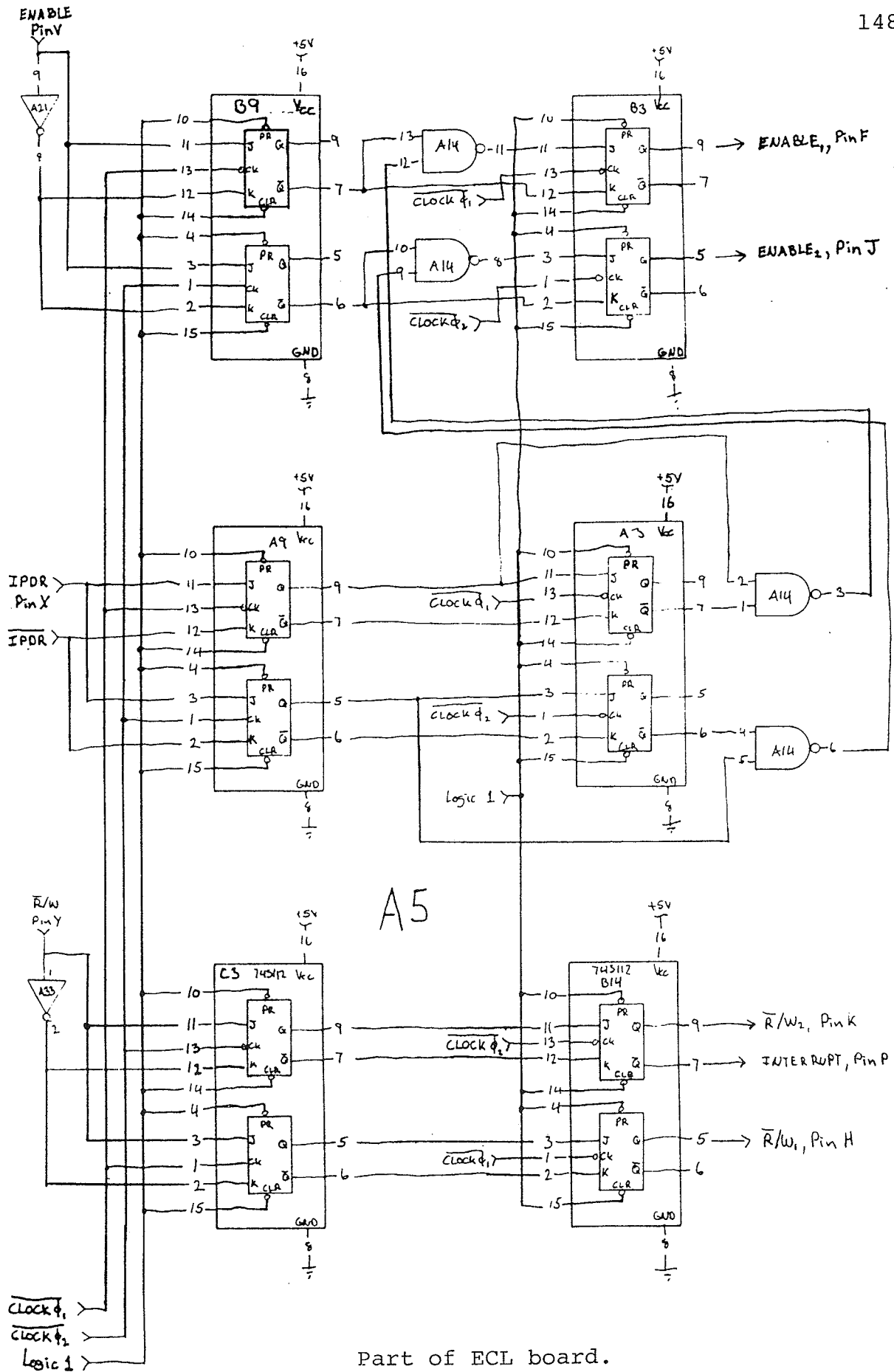


Power supply for pre-amp.

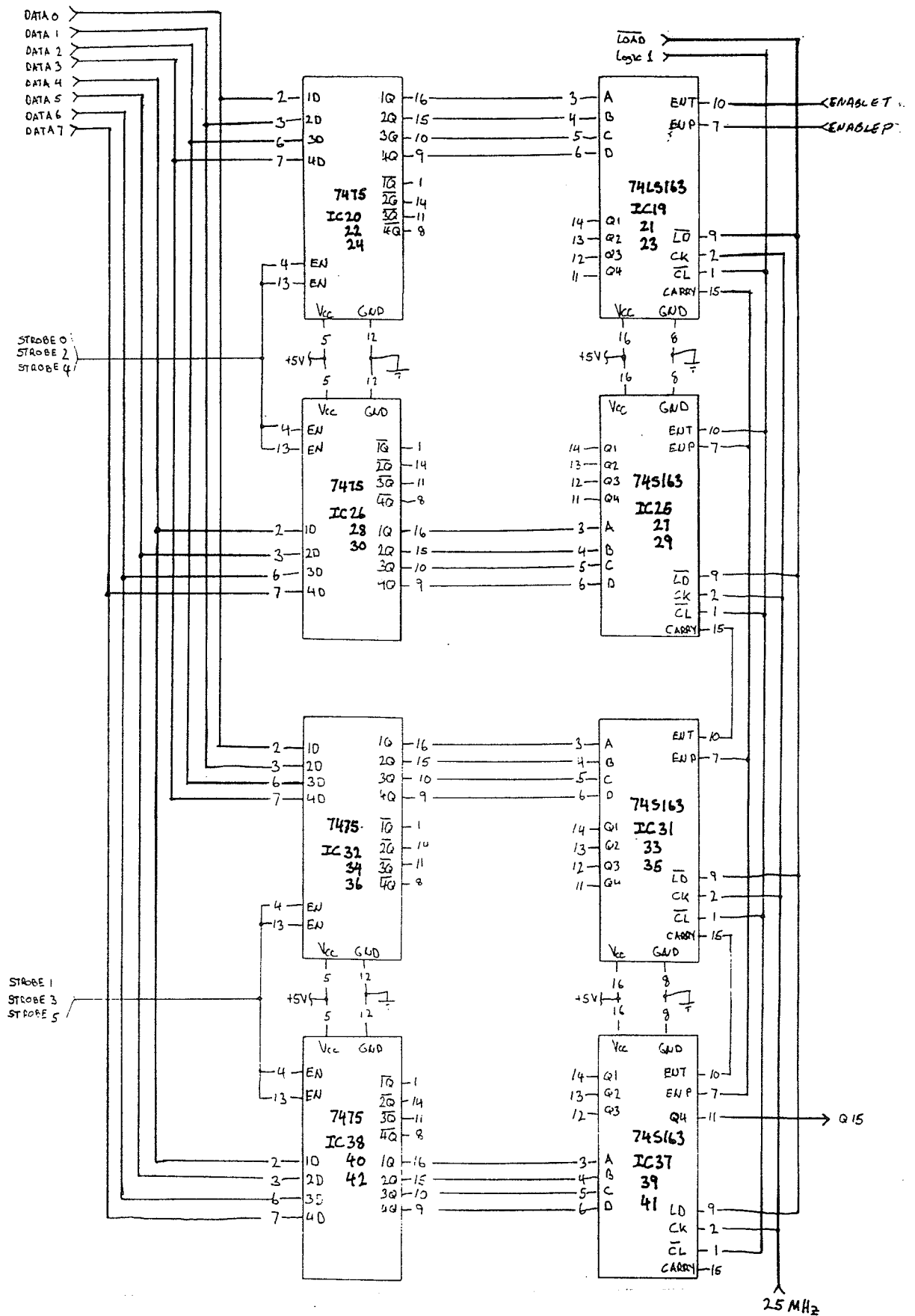


UNIVERSITY OF ILLINOIS PHYSICS DEPARTMENT SUBJECT	ENGINEERING NOTES	PROJECT	DIVISION	SHEET OF
		NAME	DATE	

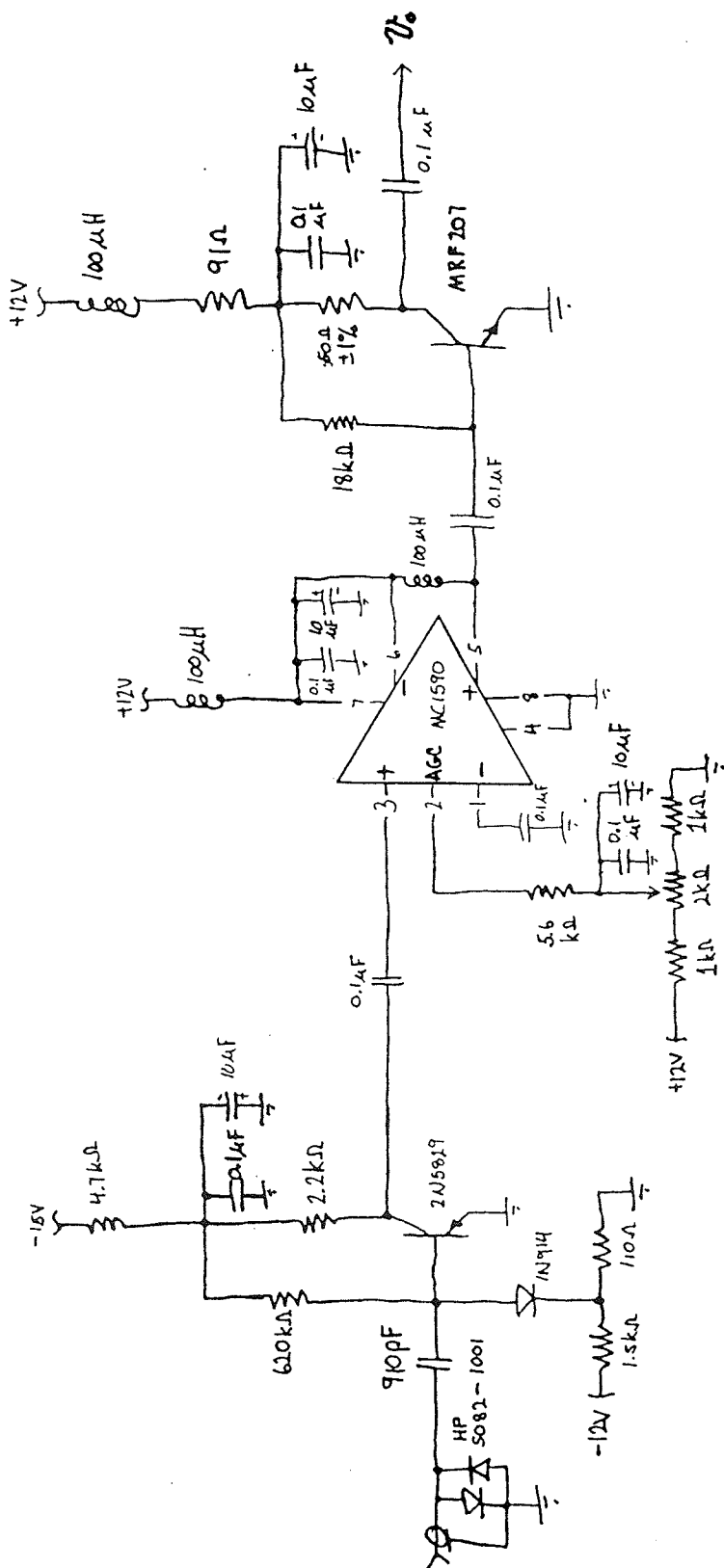




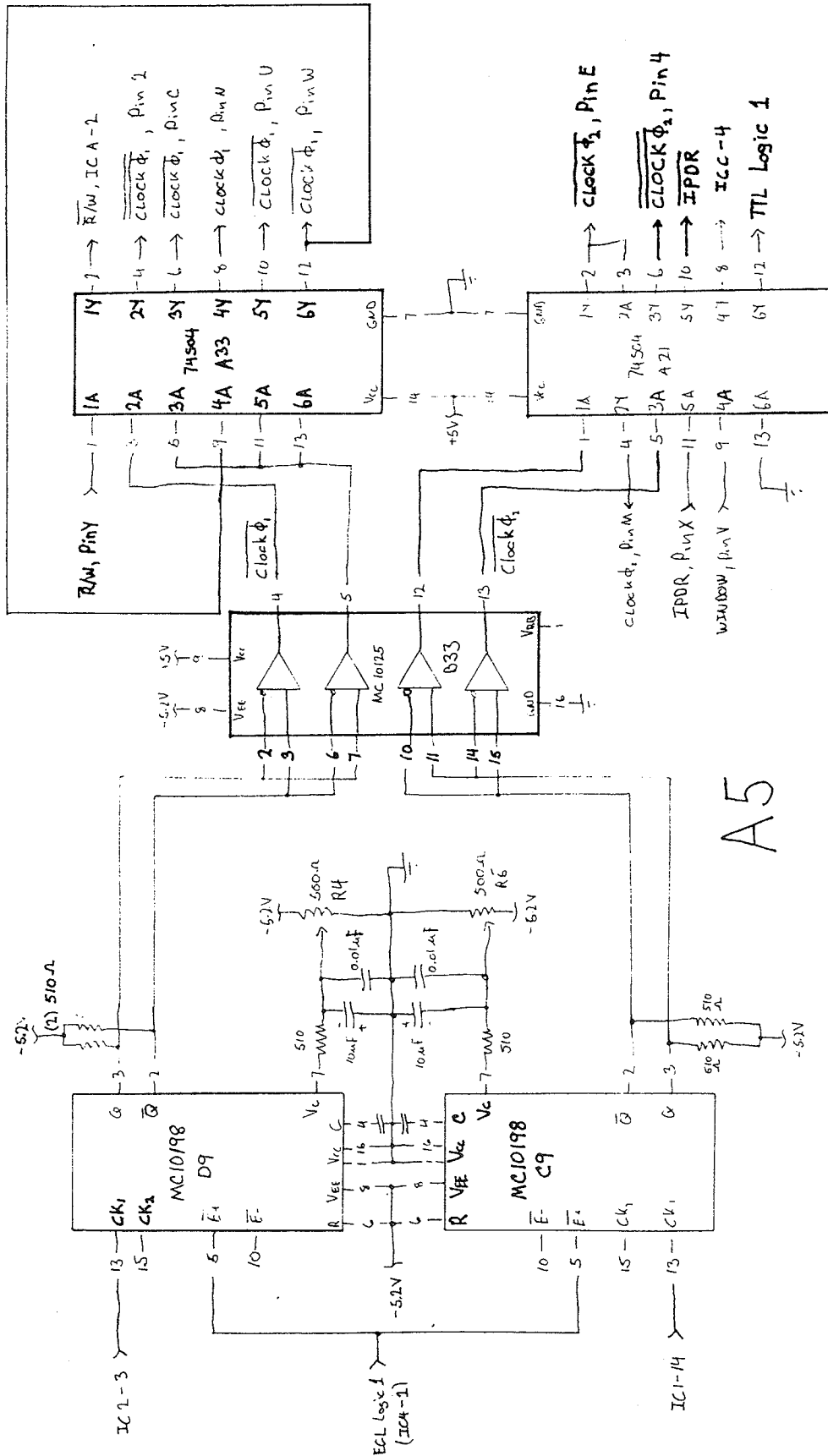
Part of ECL board.



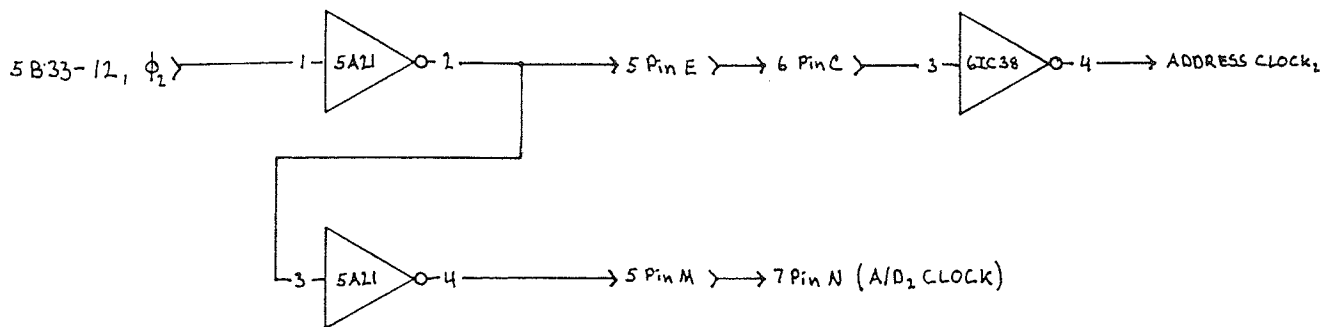
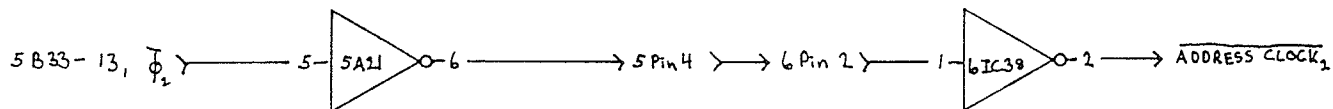
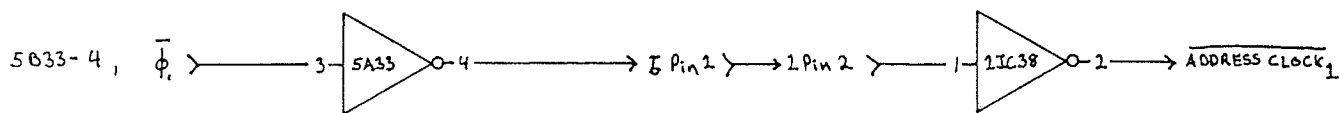
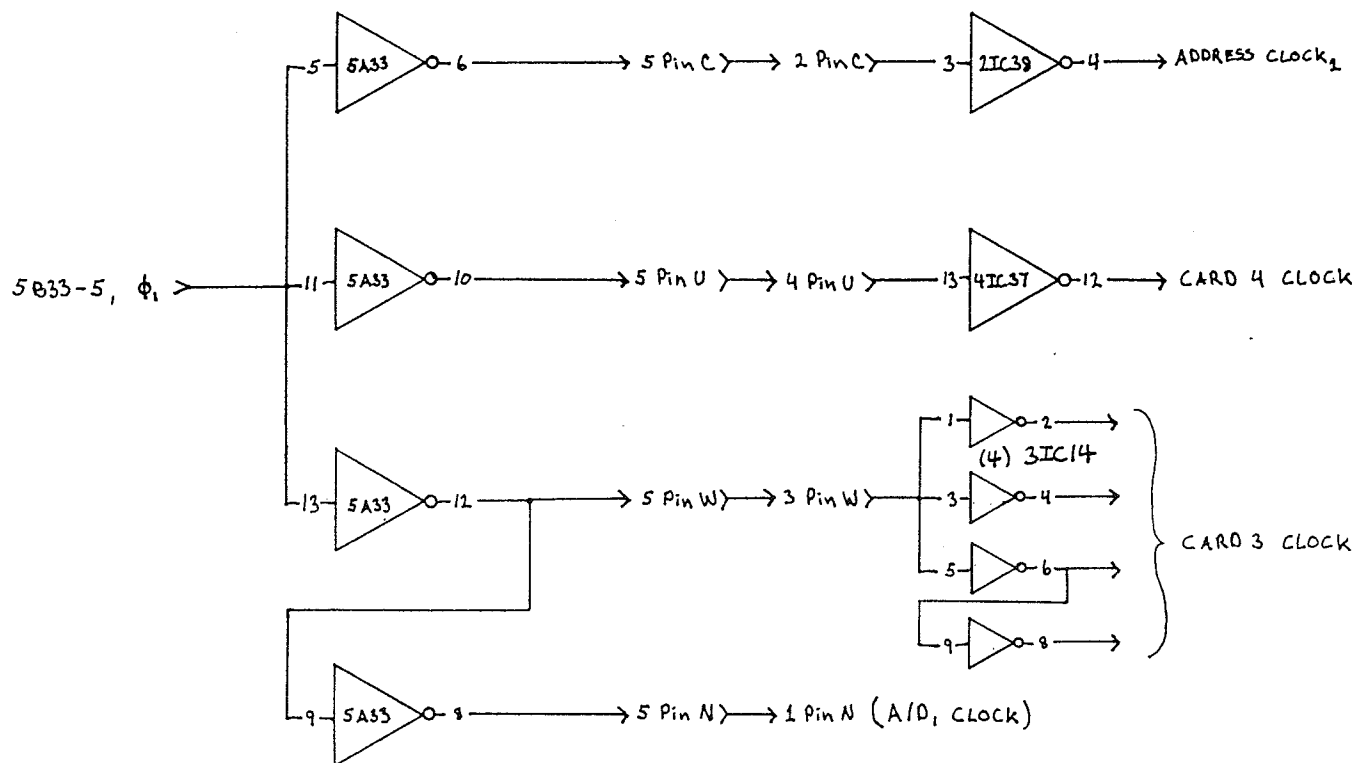
Sixteen-bit counter with latch.



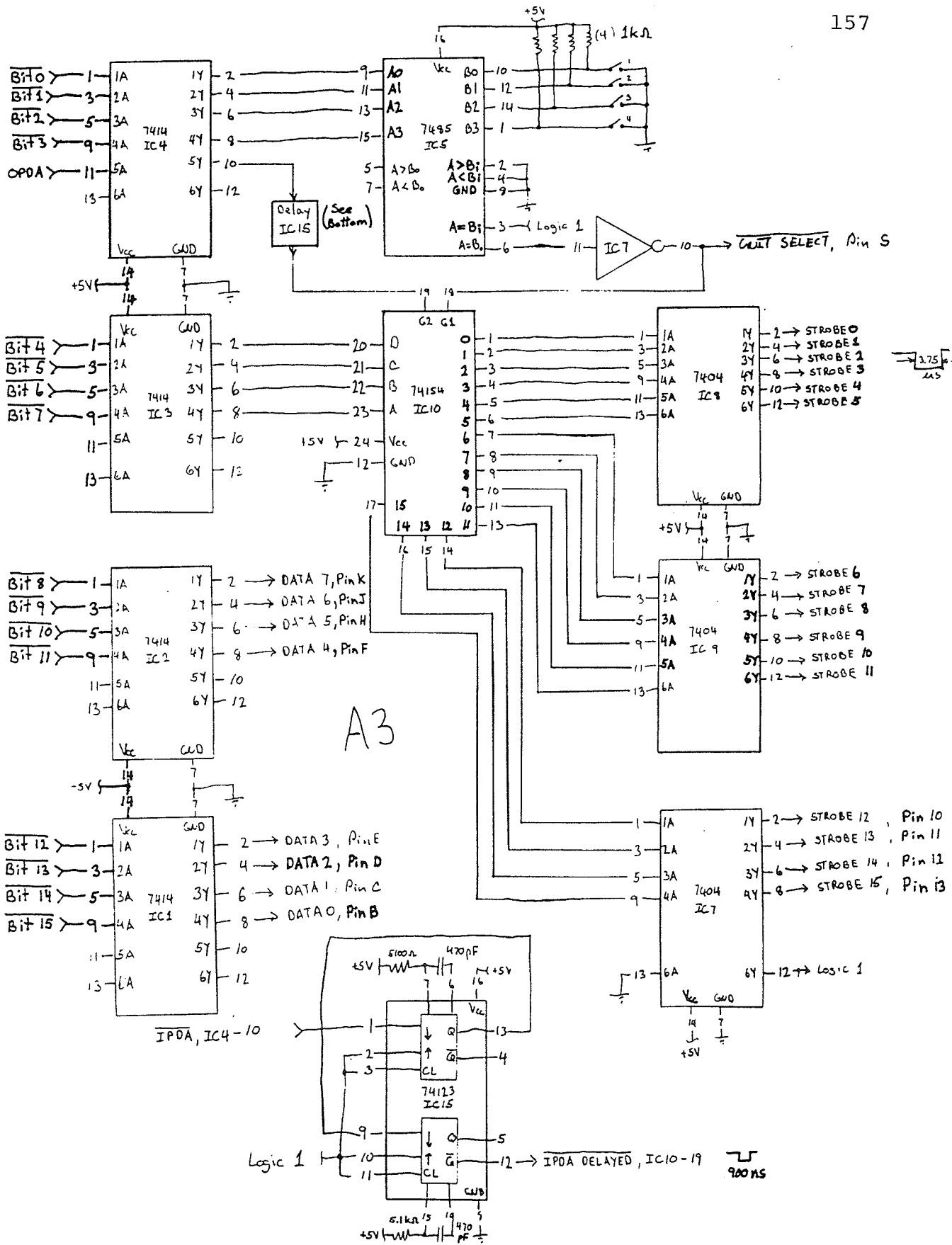
Pre-amp.



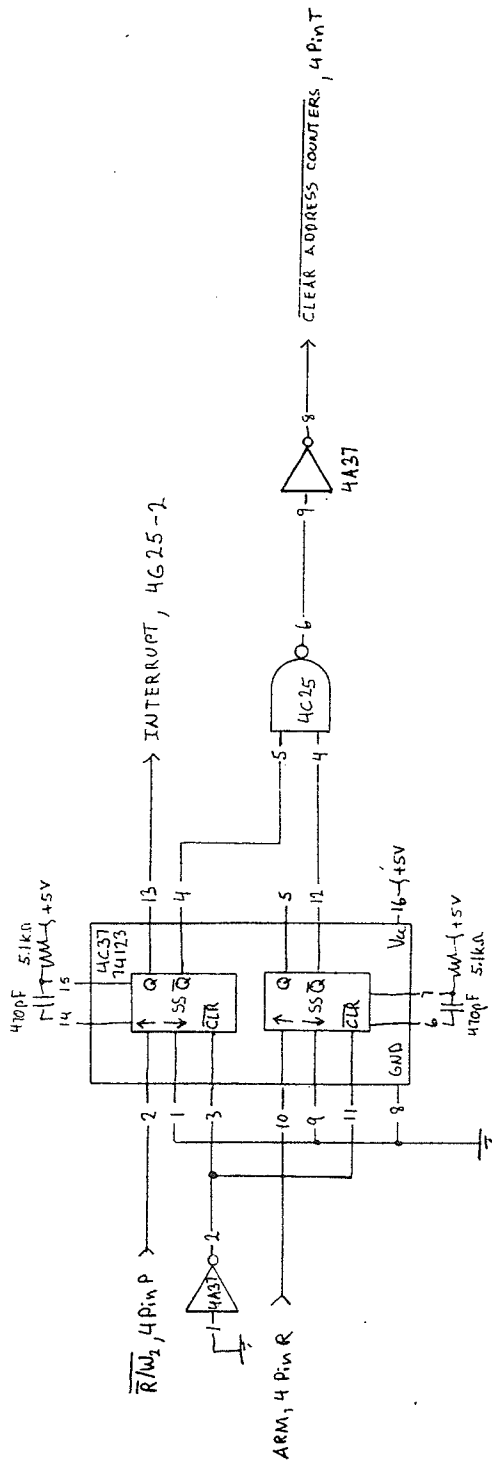
Part of ECL board.



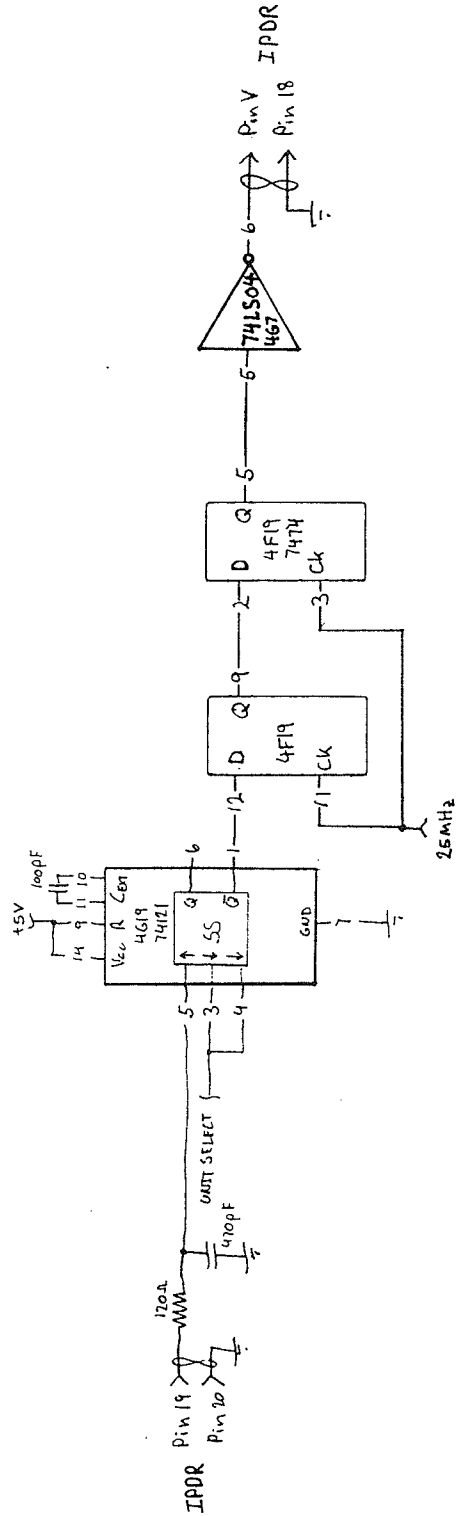
Note: All Card to Card clock connections are twisted pair.



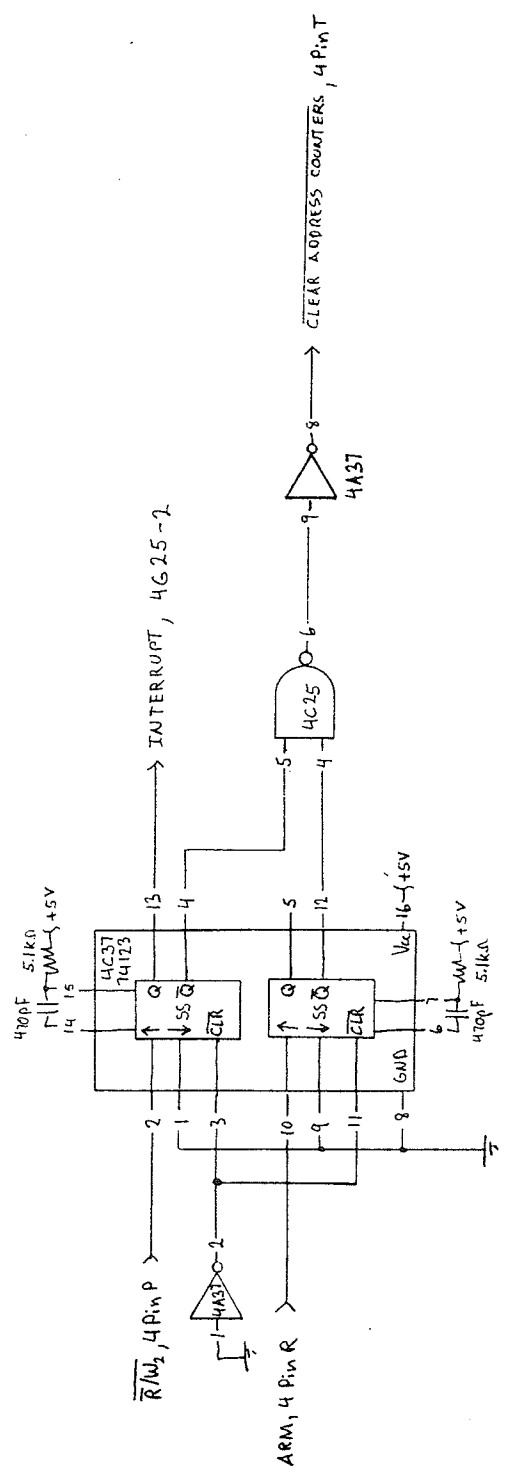
Parallel input port from computer.



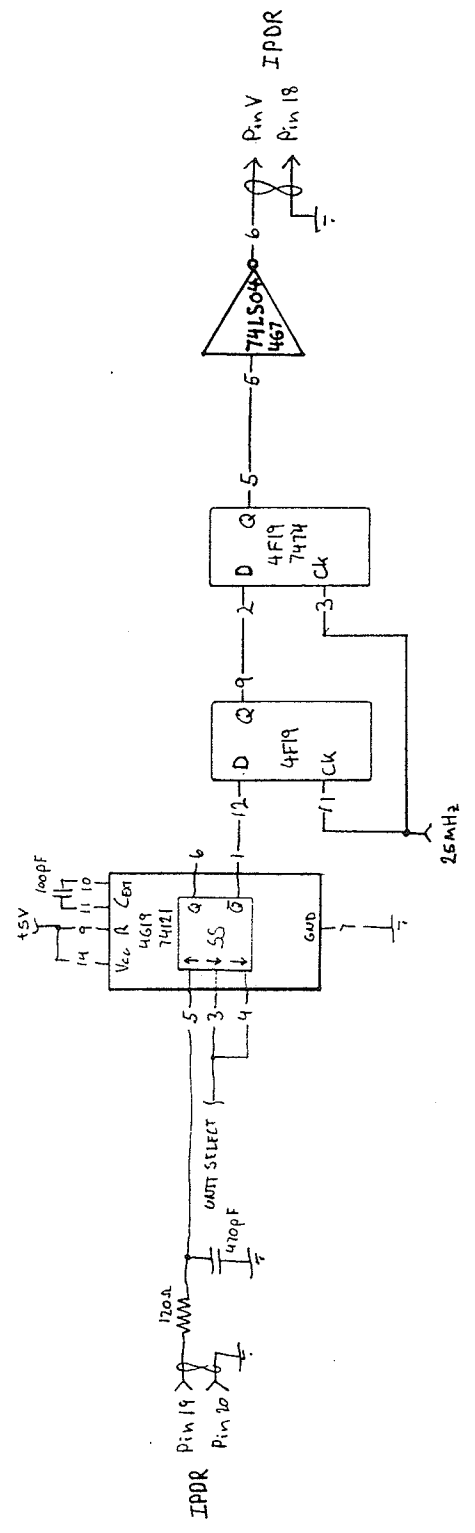
A4



IPDR and CLEAR ADDRESS COUNTER circuitry.



A4



IPDR and CLEAR ADDRESS COUNTER CIRCUITRY.

VITA

Here is the list of the required statistics of the author:

- 1) Birth date: 3/1/54.
- 2) Place of birth: Chicago, Illinois.
- 3) Military service: U.S. Air Force, July 1972 to July 1976.
- 4) B.S. degree in Electrical Engineering, December 1978, at the Illinois Institute of Technology at Chicago, Illinois.
- 5) M.S. degree in Electrical Engineering, April 1981, at the University of Illinois, Urbana, Illinois.
- 6) Ph.D. degree in Electrical Engineering, Spring 1985, at the University of Illinois, Urbana, Illinois.

LIST OF REFERENCES

- [1] D. W. Baker, F. K. Forster, and R. E. Daigle, *Methods and Phenomena 3, Ultrasound: Its Application in Medicine and Biology*. New York: Elsevier Scientific Publishing Company, pp. 303-316, 1978.
- [2] D. W. Baker, "Pulsed Ultrasonic Doppler Blood-Flow Sensing," *IEEE Trans. Sonics and Ultrasound*, vol. SU-17, pp. 170-185, July 1970.
- [3] J. E. Jorgensen, D. N. Campau, and D. W. Baker, "Physical Characteristics and Mathematical Modelling of the Pulsed Ultrasonic Flowmeter," *Med. Biol. Eng.*, no. 11, pp. 404-421, 1973.
- [4] P. N. T. Wells, "A range gated ultrasonic Doppler system," *Med. Biol. Eng.*, vol. 7, pp. 641-652, 1969.
- [5] P. J. Bendick and V. L. Newhouse, "Ultrasonic random-signal flow measurement systems," *J. Acoust. Soc. Am.*, vol. 56, pp. 860-865, Sept. 1974.
- [6] C. P. Jethwa, M. Kaveh, G. R. Copper, and F. Saggio, "Blood Flow Measurements Using Ultrasonic Pulsed Random Signal Doppler System," *IEEE Trans. Sonics and Ultrasound*, vol. SU-22, pp. 1-11, Jan. 1975.
- [7] D. J. Cathignol, C. Fourcade, and J. Chapelon, "Transcutaneous Blood Flow Measurements Using Pseudorandom Noise Doppler System," *IEEE Trans. Biomed. Eng.*, vol. BME-27, pp. 30-36, Jan. 1980.

- [8] M. B. Histanđ, R. A. Corace, and M. K. Wells, "Ultrasound Doppler and Echo Combined as a Noninvasive Blood Flowmeter," ISA Trans., vol. 21, no. 2, pp. 53-57, 1982.
- [9] L. W. Varner, V. L. Newhouse, and P. J. Bendick, "Application of Transit Time Effects to the Independent Measurement of Blood Velocity and Angle," Proc. 28th ACEMB, p. 75, Sept. 1975.
- [10] A. Nowicki and J. M. Reid, "An Infinite Gate Pulse Doppler," Ultrasound in Med. & Biol., vol. 7, pp.41-50, 1981.
- [11] W. R. Brody, "Theoretical Analysis of the Ultrasonic Blood Flow Meter," Ph.D. dissertation, Dep. Elec. Eng., Stanford Univ., Stanford, Calif., 1972.
- [12] W. R. Brody, "Theoretical Analysis of the CW Doppler Ultrasonic Flowmeter," IEEE Trans. Biomed. Eng., vol. BME-21, pp. 183-192, May 1974.
- [13] V. L. Newhouse, P. J. Bendick, and L. W. Varner, "Analysis of Transit Time Effects on Doppler Flow Measurements," IEEE Trans. Biomed. Eng., vol. BME-23, pp. 381-387, Sept. 1976.
- [14] K. K. Shung, R. A. Sigelmann, and J. M. Reid, "Scattering of Ultrasound by Blood," IEEE Trans. Biomed. Eng., vol. BME-23, pp. 460-467, 1976.

- [15] B. A. J. Angelsen, "A Theoretical Study of the Scattering of Ultrasound from Blood," IEEE Trans. Biomed. Eng., vol. BME-27, pp. 61-67, Feb. 1980.
- [16] A. C. Burton, Physiology and Biophysics of the Circulation. New York: Year Book Medical Publ., 1965.
- [17] M. E. Valkenburg, Analog Filter Design. New York: Holt, Rinehart and Winston, 1982.
- [18] M. D. Srinath and P. K. Rajasekaran, An Introduction to Statistical Signal Processing With Applications. New York: Wiley, pp. 375-380, 1979.
- [19] H. L. Van Trees, Detection, Estimation, and Modulation Theory. New York: Wiley, 1968.
- [20] M. Born and E. Wolf, Principles of Optics. New York: Pergaman Press, pp. 435-449, 1970.
- [21] R. W. Fox and A. T. McDonald, Introduction to Fluid Mechanics. New York: Wiley, pp. 329, 1973.
- [22] P. G. Hoel, Introduction to Mathematical Statistics. New York: Wiley, 1971.
- [23] H. L. Langhaar, "Steady flow in the transition length of straight tube," J. Appl. Mech., vol. 9, pp. 55-58, 1942.
- [24] N. N. Mohsenin, Physical Properties of Plant and Animal Materials. New York: Gordon and Breach Science Publishers, 1970.

- [25] H. Taub and D. L. Schilling, Principles of Communication Systems. New York: McGraw-Hill, pp. 33, 1971.
- [26] A. Papoulis, Probability, Random Variables, and Stochastic Processes. New York: McGraw-Hill, 1965.
- [27] B. A. J. Angelsen, "Instantaneous Frequency, Mean Frequency, and Variance of Mean Frequency Estimators for Ultrasonic Blood Velocity Doppler Signals," IEEE Trans. Biomed. Eng., vol. BME-28, pp. 733-741, Nov. 1981.